

An inverse problem framework for reconstruction  
of phonon properties using solutions of the  
Boltzmann transport equation

by

Mojtaba Forghani



Submitted to the Department of Mechanical Engineering  
in partial fulfillment of the requirements for the degree of

Doctor of Philosophy in Mechanical Engineering and Computation

at the

MASSACHUSETTS INSTITUTE OF TECHNOLOGY

September 2019

© Massachusetts Institute of Technology 2019. All rights reserved.

**Signature redacted**

Author .....  
Department of Mechanical Engineering

August 25, 2019

Certified by ..... **Signature redacted** .....

~~Nicolas G. Hadjiconstantinou~~  
Professor

~~Thesis Supervisor~~

Accepted by ..... **Signature redacted** .....

~~Nicolas G. Hadjiconstantinou~~  
Chairman, Department Committee on Graduate Theses  
Co-Director, Computational Science and Engineering

Accepted by ..... **Signature redacted** .....

~~Youssef M. Marzouk~~  
Co-Director, Computational Science and Engineering



# An inverse problem framework for reconstruction of phonon properties using solutions of the Boltzmann transport equation

by

Mojtaba Forghani

Submitted to the Department of Mechanical Engineering  
on August 25, 2019, in partial fulfillment of the  
requirements for the degree of  
Doctor of Philosophy in Mechanical Engineering and Computation

## Abstract

A methodology for reconstructing phonon properties in a solid material, such as the frequency-dependent relaxation time distribution, from thermal spectroscopy experimental results is proposed and extensively validated. The reconstruction is formulated as a non-convex optimization problem whose goal is to minimize the difference between the experimental results and the one calculated by a Boltzmann transport equation (BTE)-based model of the experimental process, with the desired material property treated as the unknown in the optimization process. Crucially, the proposed approach makes no assumption of an underlying Fourier behavior, thus avoiding all approximations associated with that assumption.

The proposed method combines a derivative-free optimization method, referred to as the Nelder-Mead algorithm, with a graduated (multi-stage) optimization framework. Our results show that, compared to other reconstruction methods, the proposed method is less sensitive to scarcity of data in a specific transport regime (such as sub-micron length scales). The method is also very versatile in incorporating known information into the optimization process, such as the known value of the material thermal conductivity or solid-solid interface conductance if a material interface is present; addition of this information improves the quality of the optimization. In the presence of a material interface of unknown conductance, we show that simultaneous reconstruction of both the solid-solid interface frequency-dependent transmissivity function and the relaxation time function is possible.

The optimization algorithm is validated using both synthetically generated temperature profiles (generated by solving the BTE), as well as experimentally measured signals. In the case of synthetic input data, the reconstructed properties are compared to the material models used to create the input data. In the case of experimental data, we compare the reconstructed phonon properties with their corresponding benchmark values, obtained using either theoretical predictions, such as relaxation times from density functional theory, or experimentally measured, such as the experimentally

measured interface transmissivities. The interface transmissivity reconstruction is also validated on the 2D-dots geometry in the presence of Al-Si interface. Our results show good accuracy in all cases.

The reliability and uniqueness of the optimized solution as well as its statistical properties due to the presence of noise are studied using a number of statistical techniques. Our analysis provides strong evidence that the formulated optimization problem has a unique solution; furthermore the proposed optimization-based framework is capable of finding that solution with good accuracy.

Thesis Supervisor: Nicolas G. Hadjiconstantinou

Title: Professor

## Acknowledgments

First and foremost, I would like to thank my supervisor, Prof. Nicolas Hadjiconstantinou, for being a great advisor, mentor and friend throughout my PhD program. His helpfulness, kindness, and unconditional support have had lasting impact on both my academic and non-academic life. Working with you has certainly been one of the best decisions I have made in my life!

I would also like to thank my committee members, Prof. Gang Chen and Prof. Youssef Marzouk, for their many great advices which have significantly improved the quality of my research. I am grateful to both of you for agreeing to be part of my PhD committee and sharing your valuable viewpoints about every detail of my research.

I would like to thank Prof. Domitilla Del Vecchio, my master's supervisor, for many lessons she has taught me regarding academic research. Although you have not been a part of my PhD committee, many great points that I have learnt from you had indirect, nevertheless, substantial influence on my PhD research.

I am very thankful to Dr. Jean-Philippe Peraud for helping me build the foundation of my PhD work. It would not be an exaggeration to say that I owe my PhD to you JP, since one of the main reasons that this thesis became possible is high efficiency of the adjoint Monte Carlo algorithm that you have developed in your PhD program.

There are many people that their input has notably shaped this work. Many useful comments and suggestions from Dr. Vazrik Chiloyan, Dr. Samuel Huberman, Dr. Alex Maznev, Dr. Giuseppe Romano, and Dr. Lingping Zeng in the past few years have improved the quality of my research.

I am thankful to my friends, who have been an important part of my life throughout my graduate program; to Michael Braun, Chong Yang Goh, Ashkan Haji Hosseinloo, and Reza Mohammadi, for many many great happy moments that we shared; to Khalid Jawed for being incredibly supportive and helpful; to Mehran Dibaji, Ali Hemmatifar, and Mohammad Rahimi for creating many happy moments; to Thomas Fronk, Charlie Hirst, and Vrushank Phadnis, for being amazing friends and house-

mates; to Katie Cavanagh, Nisha Chandramoorthy, Bobak Kiani, Milad Marvian, Mathew Swisher, Petr Vorobev, Gerald Wang, Xiaoyu Wu, and Essie Yu for making our office, Nexus, an amazing workplace; and many more.

I owe everything, from this thesis to my existence, happiness, upbringing, and education, to name a few, to my parents and my sisters. I would like to thank them for many sacrifices they have made for me over the years.

Lastly, I would like to thank the United States Department of Energy for supporting my work through the S3TEC (Solid-State Solar-Thermal Energy Conversion) center.

# Contents

<b>1</b>	<b>Introduction</b>	<b>21</b>
1.1	Background . . . . .	21
1.2	Proposed approach overview . . . . .	22
1.3	Thesis outline . . . . .	23
<b>2</b>	<b>Reconstruction using optimization</b>	<b>25</b>
2.1	Formulation . . . . .	26
2.1.1	Governing equations . . . . .	26
2.1.2	Inverse problem formulation . . . . .	27
2.1.3	Optimization algorithm . . . . .	30
2.2	Application example and validation . . . . .	33
2.2.1	The TTG experiment . . . . .	33
2.2.2	Generation of synthetic experimental data . . . . .	34
2.2.3	Reconstruction . . . . .	35
2.2.4	Validation . . . . .	39
2.3	Comparison to effective thermal conductivity approach . . . . .	45
<b>3</b>	<b>Reconstruction in the presence of interface</b>	<b>53</b>
3.1	Formulation . . . . .	54
3.1.1	Governing equations for transport across interface . . . . .	54
3.1.2	Inverse problem formulation in the presence of interface . . . . .	54
3.2	Reconstruction . . . . .	56
3.2.1	Problems with known interface conductance . . . . .	57

3.2.2	Problems with unknown interface conductance . . . . .	59
3.2.3	Initialization protocol . . . . .	60
3.3	Validation . . . . .	61
3.3.1	Generation of synthetic experimental data . . . . .	61
3.3.2	Results . . . . .	62
3.3.3	Effect of interface treatment . . . . .	66
3.3.4	Why is interface transmissivity reconstruction not as accurate as relaxation time reconstruction? . . . . .	69
3.3.5	Comparison to the effective thermal conductivity approach . .	72
<b>4</b>	<b>Validation on experimental data</b>	<b>77</b>
4.1	Formulation . . . . .	78
4.2	Reconstruction . . . . .	79
4.2.1	Optimization process . . . . .	79
4.2.2	Optimization in the presence of experimental data . . . . .	80
4.3	Validation . . . . .	82
4.4	Sensitivity analysis of the solution . . . . .	85
<b>5</b>	<b>Reliability of the optimization process and results</b>	<b>91</b>
5.1	Uniqueness of the optimization solution . . . . .	92
5.2	Does the free path distribution define a unique relaxation time function?	96
5.3	On the inability of the free path distribution to uniquely define the relaxation time function . . . . .	98
5.4	Bayesian approach to relaxation time reconstruction . . . . .	101
5.5	Probabilistic characterization of the optimization results . . . . .	109
<b>6</b>	<b>Summary and outlook</b>	<b>123</b>
<b>A</b>	<b>Parameters of piece-wise linear model for relaxation time</b>	<b>129</b>
<b>B</b>	<b>Semi-analytical solution for the transient thermal grating</b>	<b>131</b>
<b>C</b>	<b>Solution of the transient thermal grating for late times</b>	<b>133</b>

<b>D</b>	<b>Analytical solution for transient thermal grating in ballistic limit</b>	<b>135</b>
<b>E</b>	<b>Parameters of piece-wise linear model for transmissivity</b>	<b>137</b>



# List of Figures

2-1	An example of simplex update in the NM algorithm; the case of two unknowns (corresponding to $n = 2$ ) is shown. (a)- Point $\mathbf{p}^2$ of the previous simplex (which consists of points $\mathbf{p}^0$ , $\mathbf{p}^1$ , and $\mathbf{p}^2$ ) is replaced with a new point from the set $\{\mathbf{p}^c, \mathbf{p}^{cc}, \mathbf{p}^r, \mathbf{p}^e\}$ . The new simplex consists of $\mathbf{p}^0$ , $\mathbf{p}^1$ , and the replacement of $\mathbf{p}^2$ . (b)- If none of the candidate points in figure 5-13a have an objective function smaller than $\mathcal{L}(\mathbf{p}^2)$ , then the simplex shrinks. The new simplex is $\mathbf{p}^0$ , $\mathbf{v}^1$ , and $\mathbf{v}^2$ . . . . .	32
2-2	The TTG experiment; a sinusoidal temperature profile ( $T_m$ in the figure) with different wavelengths ( $L$ ) is created at time $t=0$ via crossing two varying angled pump pulses. A fast detector measures the combined diffracted probe light and the reference beam [10]. The Si film thickness is constant at $D$ . In the case of 1D-TTG (this chapter), the transport is one-dimensional, $D \rightarrow \infty$ . . . . .	33
2-3	Dependence of the final value of $\mathcal{L}$ at the third stage on $\mathcal{N}_{\text{BTE}}$ . Increasing the number of particles decreases the mean and variance of $\mathcal{L}$ . . . . .	38
2-4	Comparison between true and reconstructed relaxation times and free path distribution using IFFT of the semi-analytical result (2.11) for the Holland material model. . . . .	40
2-5	Comparison between true and reconstructed relaxation times and free path distribution using $T_{\text{BTE}}$ obtained from adjoint MC simulation using the Holland material model. . . . .	41

2-6	Comparison of the synthetic temperature profile obtained by MC simulations using $\mathcal{N}_m = 10^9$ and $\mathcal{N}_m = 10^3$ computational particles based on the Holland material model. Two different grating wavelengths are shown. . . . .	41
2-7	Comparison between true and reconstructed relaxation times and free path distribution using IFFT of (2.11) from noisy synthetic data for the Holland material model. . . . .	42
2-8	Comparison between true and reconstructed relaxation times and free path distribution using adjoint MC simulation from noisy synthetic data for the Holland material model. . . . .	42
2-9	Comparison between true and reconstructed relaxation times and free path distribution using IFFT of (2.11) with the <i>ab initio</i> material model. . . . .	43
2-10	Comparison between true and reconstructed relaxation times and free path distribution using $T_{\text{BTE}}$ obtained from adjoint MC simulation of the <i>ab initio</i> material model. . . . .	43
2-11	Comparison between true and reconstructed relaxation times and free path distribution using IFFT of (2.11) from noisy synthetic data for the <i>ab initio</i> material model. . . . .	44
2-12	Comparison between true and reconstructed relaxation times and free path distribution using adjoint MC simulation from noisy synthetic data for the <i>ab initio</i> material model. . . . .	44

2-13 Comparison between true and reconstructed data for the case of limited range of input wavelengths: (a) Reconstructed relaxation times using IFFT of the semi-analytical result (2.11) for the Holland material model using  $L = 1 \mu\text{m}, 5 \mu\text{m}, 10 \mu\text{m},$  and  $50 \mu\text{m}$ . Relaxation data was “recorded” in the time period  $0 \leq t \leq t_L$ , where  $t_L = \min(t_{L,1\%}, 50 \text{ ns})$ ; (b) Comparison of the free path distribution obtained from reconstruction shown in (a) with data transcribed [61] from figure 2 of [13] (denoted “Reconstructed CDF,  $\kappa_{\text{eff}}$ ”), obtained from the effective thermal conductivity approach using 12 relaxation profiles with wavelengths in the range  $L = 1 - 15 \mu\text{m}$ . . . . . 46

2-14 Comparison between the method proposed in the present work and various Fourier-based methods. Temperature relaxation profiles are shown for four grating wavelengths and compared to BTE solution for the *ab initio* material model (denoted “BTE”). The prediction of the method proposed here, denoted as “present”, is given by solution of the Boltzmann equation based on the reconstructed relaxation time data of figure 2-9. Solutions based on equations (2.14) and (2.19) are denoted “Equation (2.14)” and “Equation (2.19)”, respectively. . . . . 49

2-15 Comparison between the method proposed in the present work and various Fourier-based methods. Temperature relaxation profiles are shown for four grating wavelengths and compared to BTE solution for the Holland material model (denoted “BTE”). The prediction of the method proposed here, denoted as “present”, is given by solution of the Boltzmann equation based on the reconstructed relaxation time data of figure 2-4. Solutions based on equations (2.14) and (2.19) are denoted “Equation (2.14)” and “Equation (2.19)”, respectively. . . . . 50

3-1	2D-dots geometry, comprising a periodic array of Al “dots” on a Si substrate. The structure is assumed to be sufficiently large that it can be approximated as infinite in the x and y directions; moreover, the Si substrate thickness is sufficiently large to be approximated as semi-infinite. The dot height is constant at $L_{\text{Al}} = 100$ nm, while the dot base is square with edge length $L$ . The ratio between $L$ and the periodicity of the structure is constant at 0.5. The experimental measurement, $T_{\text{m}}(t, \mathbf{x}; L)$ , corresponds to the surface temperature of Al after the initial heating event at $t = 0$ . . . . .	61
3-2	Reconstructed material properties with <i>ab initio</i> relaxation times, experimental transmissivities, and noise-free synthetic relaxation profiles.	63
3-3	Reconstructed material properties with <i>ab initio</i> relaxation times, experimental transmissivities, and noisy synthetic relaxation profiles. .	63
3-4	Reconstructed material properties with Holland relaxation times, experimental transmissivities, and noise-free synthetic relaxation profiles.	64
3-5	Reconstructed material properties with Holland relaxation times, DMM transmissivities, and noise-free synthetic relaxation profiles. . . . .	64
3-6	Reconstructed material properties with Holland relaxation times, experimental transmissivities, and noisy synthetic relaxation profiles. . .	65
3-7	Reconstructed material properties with Holland relaxation times, DMM transmissivities, and noisy synthetic relaxation profiles. . . . .	65
3-8	Reconstructed material properties with Holland relaxation times, experimental transmissivities, and noise-free synthetic relaxation profiles with separate linear models for frequency-dependent transmissivities of <i>LA</i> and <i>TA</i> branches. . . . .	67
3-9	Reconstructed material properties with Holland relaxation times, experimental transmissivities, and noise-free synthetic relaxation profiles with $T_{21,\omega}$ (the transmissivity from Al to Si) being unknown. . . . .	68

3-10	Comparison between the synthetic temperature profiles and the ones generated from the reconstructed properties of (a)- figure 3-4, (b)- figure 3-2, and (c)- figure 3-9. . . . .	68
3-11	Reconstructed material properties with Holland relaxation times, experimental transmissivities, and noise-free temperature profiles with $\tau'_{Al} = 100\tau_{Al} = 1$ ns. . . . .	69
3-12	Reconstructed material properties with Holland relaxation times, experimental transmissivities, and noise-free temperature profiles with variable dot heights, $L_{Al}$ . . . . .	71
3-13	Reconstructed free path distribution based on effective thermal conductivity approach (c); “expt.” denotes the experimental interface model adapted from [67]. Length dependent cumulative effective heat conductivity (b). The suppression function based on experimental transmissivity interface model (a). . . . .	73
3-14	Non-diffusive behavior inside silicon. (a) Mode and time dependent Knudsen number inside silicon for pump-probe measurement time, $0 < t < 5$ ns, based on BTE solution using Holland properties, experimental transmissivities, and noise-free relaxation profiles. (b) Effect of measurement time on transport regime inside silicon for both experimental and DMM transmissivities. The plot shows $\kappa_{\text{eff}}(L = \infty)/\kappa$ for different measurement times. This quantity approaches 1 as the measurement window moves to later times. . . . .	76
4-1	(a)- The 2D-TTG experiment; the Si film thickness is constant at $D=400$ nm. (b) A few examples of the measured signal for different length scales. Nineteen wavelengths in the range $L = 1.6\text{--}21 \mu\text{m}$ were measured.	78

4-2	Comparison between reconstructed material properties and DFT calculations. (a) Reconstructed and “model A” DFT calculations of relaxation times. (b) Reconstructed and “model B” DFT calculations of relaxation times. (c) Reconstructed, “model A”, and “model B” DFT calculation of free path distribution. . . . .	83
4-3	Comparison between experimentally measured (“expt”), reconstructed (“recons”), and DFT-based simulated temperature profiles. (a) DFT vs. experimental measurements. (b) Reconstructed vs. experimental measurements. (c) DFT vs. reconstructed for sub-micron regime. All “recons” results are based on the reconstructions of figure 4-2. . . . .	84
4-4	Comparison between experimentally measured (“expt”) temperature relaxation profiles and those predicted by reconstructed data (“recons”) using information of experiments in the range $L = 10\text{--}21 \mu\text{m}$ . . . . .	85
4-5	Sensitivity analysis of the solution of the optimization algorithm at the minimum point using “model A” (figure 4-2a) for (a)- long/medium and (b)- short free paths. The “x” signs show the minimum point (the solution from the optimization algorithm). . . . .	87
4-6	Comparison between temperature profiles based on optimal solutions and perturbed $LO$ solutions at small length scales for (a)- $L = 200 \text{ nm}$ and (b)- $L = 20 \text{ nm}$ . . . . .	88
4-7	Sensitivity analysis of the solution of the optimization algorithm at the minimum point using “model B” (figure 4-2b) for (a)- long/medium and (b)- short free paths. The “x” signs show the minimum point (the solution from the optimization algorithm). . . . .	89
4-8	Sensitivity analysis of the solution of the optimization algorithm at the minimum point with length scales in the range $L = 10\text{--}21 \mu\text{m}$ (figure 4-4) for (a)- long/medium and (b)- short free paths. The “x” signs show the minimum point (the solution from the optimization algorithm). . . . .	89

5-1	The value of the objective function versus the distance (see equation (5.5)) between the points sampled during GBNM and the true solution for (a)- Holland and (b)- <i>ab initio</i> model. . . . .	95
5-2	The value of the objective function versus the distance (see equation (5.5)) between the points sampled during GBNM and the true solution for (a)- Holland and (b)- <i>ab initio</i> model. . . . .	95
5-3	The value of the objective function versus the relative distance (see equation (5.6)) between the points sampled during GBNM and the true solution for <i>ab initio</i> model. (b) is the magnified version of (a) close to the correct solution. . . . .	97
5-4	(a)- The reconstructed relaxation time function and (b)- free path distribution and (c)- temperature profile at 100 nm wavelength based on equation (5.7) objective function. . . . .	98
5-5	The plot of $C_{\omega v_{\omega}}$ versus frequency for the (a)- <i>ab initio</i> and the (b)- Holland model.. . . .	101
5-6	Pairwise posterior marginals of different pairs of the parameters of the <i>LA</i> mode. . . . .	106
5-7	Pairwise posterior marginals of different pairs of the parameters of the <i>TA</i> mode. . . . .	107
5-8	Contour plot of the probability density of the frequency-dependent relaxation times distribution of <i>LA</i> and <i>TA</i> modes. The red line in (a) denotes the true $\tau_{\omega}^{LA}$ , while the red line in (b) denotes the true $\tau_{\omega}^{TA_1}$ and the green line in (b) denotes the true $\tau_{\omega}^{TA_2}$ . . . . .	108
5-9	Distributions at a few low frequency (a) and high frequency (b) <i>LA</i> modes. . . . .	108
5-10	Distributions at a few low frequency (a) and high frequency (b) <i>TA</i> modes. . . . .	109

5-11	Frequency-dependent relaxation time distribution of $LA$ and $TA$ modes for the noise-free measurements and forward simulations. The red line in (a) denotes the true $\tau_{\omega}^{LA}$ while the red line in (b) denotes the true $\tau_{\omega}^{TA_1}$ and the green line in (b) denotes the true $\tau_{\omega}^{TA_2}$ . . . . .	117
5-12	Frequency-dependent relaxation time distribution of $LA$ and $TA$ modes for the noisy measurements and noise-free forward simulations. The red line in (a) denotes the true $\tau_{\omega}^{LA}$ while the red line in (b) denotes the true $\tau_{\omega}^{TA_1}$ and the green line in (b) denotes the true $\tau_{\omega}^{TA_2}$ . . . . .	118
5-13	Frequency-dependent relaxation time distribution of $LA$ and $TA$ modes for the noisy measurements and forward simulations. The red line in (a) denotes the true $\tau_{\omega}^{LA}$ while the red line in (b) denotes the true $\tau_{\omega}^{TA_1}$ and the green line in (b) denotes the true $\tau_{\omega}^{TA_2}$ . . . . .	119
5-14	Distributions of $\mathbf{Y}^1$ and $\mathcal{F}^1$ for the noisy measurements and noisy forward simulations. The point in the middle of the red circle shows where the result has converged to. . . . .	120
5-15	Distribution of $\mathcal{F}^1$ for all three cases. . . . .	121

# List of Tables

3.1	Calculated interface heat conductance based on the true (first row) and reconstructed (second row) interface transmissivities; “expt.” denotes the experimental interface model adapted from [67]. . . . .	66
-----	------------------------------------------------------------------------------------------------------------------------------------------------------------------------------------------------------------	----



# Chapter 1

## Introduction

### 1.1 Background

The study of phonon dynamics in the context of nanoscale solid-state heat transport has received considerable attention [1–14]. One area of significant interest is the study of phonon relaxation time and free path distributions [12–19], in particular, the extraction of phonon relaxation times and free path distribution from thermal spectroscopy experiments [7–13]. This information is required for modeling heat transport at the kinetic level, which becomes necessary due to the failure of Fourier-based analyses at such small scales. The applications of this study include improved heat management in nanoelectronic circuits and devices [1, 2, 14, 20–22], microelectromechanical sensors [4] and nano-structured materials for improved thermoelectric conversion efficiency [3, 7, 23–26].

Thermal spectroscopy [12, 19] has emerged as a promising method for experimentally “extracting” the phonon free path distribution in a crystalline material. However, the analysis of thermal spectroscopy data remains a challenging task. To extract the free path distribution from the experimentally measured temperature relaxation profiles, researchers typically invoke the concept of “effective thermal conductivity” and proceed to match the experimentally measured response to solutions of the heat conduction equation with the thermal conductivity (or thermal diffusivity) treated as an adjustable, “effective” property [12, 19]. Unfortunately, as it was shown in [8],

this procedure implicitly assumes that heat transport is Fourier-like, which is only justified under fairly restrictive conditions (late times and large scales) that are not always satisfied under experimental conditions. On the other hand, although purely theoretical approaches such as density functional theory (DFT) have been widely used to predict phonon properties [5, 6], they have yet to rise to a stature level where they can replace experimental results, in part due to their failure to consistently reproduce experimental observations [5].

## 1.2 Proposed approach overview

In order to address these limitations, here, a technique for reconstructing phonon relaxation times is proposed which does not assume validity of Fourier’s law and does not make use of the effective thermal conductivity concept. In this technique, reconstruction is posed as an optimization problem in which the relaxation time distribution is obtained as the distribution of relaxation times that minimizes the error between experimentally measured material response and the one obtained from the Boltzmann transport equation (BTE) solutions (numerical or analytical). This method is validated using synthetically generated temperature profiles in the transient thermal grating (TTG) geometry [18, 27, 28], using both deviational Monte Carlo (MC) simulations [29–32] and inverse fast Fourier transform (IFFT) algorithms, in the presence and absence of noise in the measurement, on two different sets of silicon material properties [8], as well as experimentally measured thermal response of a two-dimensional transient thermal grating (2D-TTG) [10] geometry [11].

Due to the ubiquity of solid-solid interfaces in nano-structures [4, 33, 34] and thermal spectroscopy experiments [19, 35], the reconstruction of phonon relaxation times function (and briefly, solid-solid interface transmissivities) in the presence of an unknown solid-solid interface has also been addressed in this thesis. In particular, an extended version of the optimization algorithm discussed in the previous paragraph [8] is proposed, where frequency-dependent interface transmissivities are treated as unknowns of the optimization problem along with the frequency-dependent relaxation

times. In other words, in this framework, no assumption of underlying Fourier-like transport is made, in contrast to previous approaches which typically treat problems with interfaces by introducing an *assumed known* thermal boundary resistance [36] to the Fourier-based, effective thermal conductivity formulation [19].

The methodology proposed for the reconstruction of phonon relaxation time function in the presence of an unknown solid-solid interface is validated using deviational MC-generated synthetic relaxation profiles of time domain thermoreflectance (TDTR) experiments of the 2D-dots geometry for an Al-Si system, similar to the experimental setup used in [19]. The results suggest that the relaxation time/free path distribution can be obtained with good accuracy, despite the additional unknowns introduced by the interface description [9]. This is partly due to the fact that accurate *relaxation time reconstruction* does not require determination of the interface properties to the same accuracy level and thus the number of unknowns introduced by the interface model can be kept small. The latter finding, namely that the reconstruction of the relaxation time/free path distribution can be achieved without reconstructing the interface properties at the same level of accuracy, is of great consequence for thermal spectroscopy applications where reconstruction of the relaxation times is the primary interest, because it implies that a number of reconstructions previously thought intractable are, in fact, feasible. The results also indicate that the accuracy of the reconstructed relaxation times is fairly insensitive to the transport regime and properties of the metal dot used in the thermal spectroscopy experiment (Al in the present case)

### 1.3 Thesis outline

In Chapter 2, the Boltzmann transport equation (BTE) for study of phonon transport and the proposed inverse problem framework to reconstruct phonon relaxation times from the thermal spectroscopy experiments, in the absence of solid-solid interfaces, are introduced. The proposed method is validated on synthetically generated temperature profiles (using MC), and compared to common reconstruction approaches, such as the

effective thermal conductivity approach.

Chapter 3 discusses the extension of the optimization process proposed in Chapter 2 for reconstruction of the phonon relaxation time function, to the cases where an unknown solid-solid interface is present in the experiment. The algorithm in this chapter is validated on the synthetically generated temperature profiles (using MC) of the 2D-dots geometry. Furthermore, simultaneous reconstruction of both the phonon relaxation time function and frequency-dependent interface transmissivities, will be studied briefly.

In Chapter 4, the reconstruction method of Chapter 2 is validated using measurements obtained from a 2D-TTG experiment and compared with the DFT predictions.

In Chapter 5, we discuss the properties of the solutions of the proposed inverse problem framework. In particular, the uniqueness of the solution from a global optimization perspective and the role of the choice of the parameters involved in the optimization algorithm, as well as the noise in the experimental measurement will be investigated.

Finally, Chapter 6 concludes the thesis by discussing its contribution to the field of nanoscale thermal transport, as well as suggesting potential future directions.

## Chapter 2

# Reconstruction using optimization

We begin (section 2.1) by introducing the governing Boltzmann transport equation (BTE) and posing the reconstruction problem as an optimization framework requiring only solutions of the BTE. In section 2.2, we discuss the implementation of the proposed method in the context of an archetypal experimental setup, namely that of a transient thermal grating [28, 37, 38], on silicon; the material models used in this chapter have been used previously in [29, 39], and [28]. In the same section, we validate our proposed method using synthetic data generated through Monte Carlo (MC) simulation. Finally, in section 2.3 we provide a detailed theoretical analysis of the one-dimensional TTG problem as a means of highlighting the approximations associated with the effective thermal conductivity approach. The validation of the algorithm being discussed in this section using experimental measurements is left to Chapter 4.

This chapter is based on Ref. [8], where this material first appeared.

## 2.1 Formulation

### 2.1.1 Governing equations

Given the small temperature differences usually associated with thermal spectroscopy experiments, here we consider the linearized BTE

$$\frac{\partial e^d}{\partial t} + \mathbf{v}_\omega \cdot \nabla_{\mathbf{x}} e^d = -\frac{e^d - (de^{\text{eq}}/dT)_{T_{\text{eq}}} \Delta \tilde{T}}{\tau_\omega}, \quad (2.1)$$

where  $e^d = e^d(t, \mathbf{x}, \omega, \boldsymbol{\Omega}) = e - e_{T_{\text{eq}}}^{\text{eq}} = \hbar\omega(f - f_{T_{\text{eq}}}^{\text{eq}})$  is the deviational energy distribution,  $\omega$  is the phonon frequency,  $\boldsymbol{\Omega}$  is the phonon traveling direction,  $f = f(t, \mathbf{x}, \omega, \boldsymbol{\Omega})$  is the occupation number of phonon modes,  $\mathbf{v}_\omega = \mathbf{v}(\omega)$  is the phonon group velocity,  $\tau_\omega = \tau(\omega)$  is the frequency-dependent relaxation time and  $\hbar$  is the reduced Planck constant. Here and in what follows, we use  $\omega$  to denote the dependence on both frequency and polarization.

The above equation is linearized about the equilibrium temperature  $T_{\text{eq}}$ , to be understood here as the experimental reference temperature. In general,  $\tau_\omega = \tau(\omega, T)$ ; however, as a result of the linearization,  $\tau_\omega = \tau(\omega, T_{\text{eq}}) \equiv \tau(\omega)$ ; in other words, the solutions (and associated reconstruction) are valid for the experiment baseline temperature  $T_{\text{eq}}$ . Also,  $(de^{\text{eq}}/dT)_{T_{\text{eq}}} = \hbar\omega(df_T^{\text{eq}}/dT)|_{T_{\text{eq}}}$  and  $f_T^{\text{eq}}$  is the Bose-Einstein distribution with temperature parameter  $T$ , given by

$$f_T^{\text{eq}}(\omega) = \frac{1}{\exp(\hbar\omega/k_B T) - 1}, \quad (2.2)$$

where  $k_B$  is Boltzmann's constant. Finally,  $\Delta \tilde{T} = \Delta \tilde{T}(t, \mathbf{x}) = \tilde{T} - T_{\text{eq}}$  is referred to as the deviational pseudo-temperature ( $\tilde{T}(t, \mathbf{x})$  is the pseudo-temperature). Note that the deviational pseudo-temperature, which is different from the deviational temperature defined below, is defined by the energy conservation statement [31]

$$\int_{\boldsymbol{\Omega}} \int_{\omega} \left[ \frac{C_\omega}{\tau_\omega} \Delta \tilde{T} - \frac{e^d}{\tau_\omega} D_\omega \right] d\omega d\boldsymbol{\Omega} = 0, \quad (2.3)$$

in which  $D_\omega = D(\omega)$  is the density of states,  $C_\omega = C(\omega; T_{\text{eq}}) = D_\omega (de^{\text{eq}}/dT)_{T_{\text{eq}}}$  is the

frequency-dependent volumetric heat capacity, and  $d\Omega = \sin(\theta)d\theta d\phi$  represents the differential solid angle element such that  $\theta$  and  $\phi$  refer to the polar and azimuthal angles in the spherical coordinate system, respectively. The temperature  $T(t, \mathbf{x})$  is computed from

$$\int_{\Omega} \int_{\omega} [C_{\omega} \Delta T - e^d D_{\omega}] d\omega d\Omega = 0, \quad (2.4)$$

where  $\Delta T(t, \mathbf{x}) = T - T_{\text{eq}}$  is the deviational temperature. The frequency-dependent free path is given by

$$\Lambda_{\omega} = v_{\omega} \tau_{\omega}, \quad (2.5)$$

where  $v_{\omega} = \|\mathbf{v}_{\omega}\|$  is the group velocity magnitude.

### 2.1.2 Inverse problem formulation

Our goal is to obtain an accurate and reliable approximation to the function  $\tau_{\omega}$  from the experimental measurements, with the latter typically in the form of a temperature (relaxation) profile. Reconstruction of the free path distribution follows from relationship (2.5); in other words, the group velocities  $v_{\omega}$  are assumed known, since they can be reliably calculated either experimentally [40–43] by means of Raman spectroscopy, x-ray scattering, etc, or theoretically [44–47] using methods such as density functional theory (DFT).

We propose the use of an optimization framework in which the experimental measurements provide targets that need to be reproduced by the BTE solution; in other words,  $\tau_{\omega}$  is determined as the function that optimizes (minimizes) the discrepancy between the experimental result and the BTE prediction for the same quantity. One important consideration is use of a suitable discrete representation for  $\tau_{\omega}$ . In our formulation any number of longitudinal/transverse acoustic/optical branches  $\tau_{\omega}^S$  may exist and are solved for explicitly, where the superscript  $S$  denotes the branch; the total scattering rate  $\tau_{\omega}^{-1}$  is obtained using Matthiessen’s rule

$$\tau_{\omega}^{-1} = \sum_S (\tau_{\omega}^S)^{-1}, \quad (2.6)$$

where  $S \in \{LA, TA_1, TA_2, LO, TO_1, TO_2\}$ , in which  $LA$  denotes the longitudinal acoustic branch,  $TA_1$  and  $TA_2$  represent the two transverse acoustic branches,  $LO$  denotes the longitudinal optical branch, and  $TO_1$  and  $TO_2$  represent the two transverse optical branches.

In order to account for the most general situation where no *a priori* information is available on the functional form of the  $\tau_\omega = \tau(\omega)$  relation, we have used a piecewise linear relation between  $\log(\tau_\omega^S)$  and  $\log(\omega)$ . The intersections between the piecewise linear segments are smoothed via a third order polynomial function (of  $\log(\omega)$ ) that guarantees continuity of the relaxation time function and its first derivative [48] (the continuity requirement may be easily removed, allowing jumps between different segments). Note that our parametrization is equivalent to a (piecewise) relationship of the form of  $\tau_\omega = c_1 \omega^{c_2}$  for some real numbers  $c_1$  and  $c_2$ , which is related to relations commonly used in the literature [49, 50]. Our approach, however, does not constrain the value of  $c_2$  to any particular value or even an integer value. The actual functional form is given by

$$\begin{aligned} \log(\tau_\omega^S) = & \\ & \sum_{j=0}^{M^S-1} \left[ \frac{\log(\tau_{\omega_{j+1}}^S) - \log(\tau_{\omega_j}^S)}{\log(\omega_{j+1}^S) - \log(\omega_j^S)} (\log(\omega) - \log(\omega_j^S)) + \log(\tau_{\omega_j}^S) \right] \mathbb{1}_{\omega \in [X_{2j}^S, X_{2j+1}^S]} + \\ & \sum_{j=1}^{M^S-1} [a_j^S [\log(\omega)]^3 + b_j^S [\log(\omega)]^2 + c_j^S \log(\omega) + d_j^S] \mathbb{1}_{\omega \in (X_{2j-1}^S, X_{2j}^S)}, \quad (2.7) \end{aligned}$$

where  $M^S$  determines the number of segments. We note that since the minimum and maximum frequencies for each branch ( $\omega_0^S$  and  $\omega_{M^S}^S$ ) are known (input), there are  $2M^S$  unknowns in the model for each branch  $S \in \{LA, TA_1, TA_2, LO, TO_1, TO_2\}$ , consisting of  $\omega_1^S, \dots, \omega_{M^S-1}^S$ , and  $\log(\tau_{\omega_0}^S), \dots, \log(\tau_{\omega_{M^S}}^S)$  (see section 2.1.3 for implementation details; also note the input unknowns are denoted  $\mathbf{p}^k$  in that section). In the above,  $\mathbb{1}_{\omega \in \mathcal{S}}$  denotes the indicator function whose value is 1 if  $\omega \in \mathcal{S}$ , and 0 if  $\omega \notin \mathcal{S}$ . The closed intervals  $[X_{2j}^S, X_{2j+1}^S]$  for  $j = 0, \dots, M^S - 1$  and open intervals  $(X_{2j-1}^S, X_{2j}^S)$  for  $j = 1, \dots, M^S - 1$  denote the frequency ranges over which the piece-

wise linear and smoothing polynomial functions are active, respectively; definitions for  $X_i^S$ ,  $i = 0, \dots, 2M^S - 1$  can be found in Appendix A.

Once all  $\omega_j^S$  and  $\log(\tau_{\omega_j}^S)$  are known, the coefficients  $a_j^S$ ,  $b_j^S$ ,  $c_j^S$ ,  $d_j^S$ , and the intervals in which each linear segment or polynomial smoothing function is active inside can be computed. The relationships for calculating these parameters are provided in Appendix A.

In the interest of compactness, we will use the vectorial notations  $\boldsymbol{\tau}^S$  and  $\boldsymbol{\omega}^S$ , defined as  $\boldsymbol{\tau}^S := (\tau_{\omega_0}^S, \dots, \tau_{\omega_{M^S}}^S)$  and  $\boldsymbol{\omega}^S := (\omega_1^S, \dots, \omega_{M^S-1}^S)$ , respectively, to represent the unknown parameters. Moreover, we will use the symbol  $\mathbf{U}$  to denote the set of all unknown vectors, namely,

$$\mathbf{U} = (\boldsymbol{\tau}^{LA}, \boldsymbol{\tau}^{TA_1}, \boldsymbol{\tau}^{TA_2}, \boldsymbol{\omega}^{LA}, \boldsymbol{\omega}^{TA_1}, \boldsymbol{\omega}^{TA_2}, \boldsymbol{\tau}^{LO}, \boldsymbol{\tau}^{TO_1}, \boldsymbol{\tau}^{TO_2}, \boldsymbol{\omega}^{LO}, \boldsymbol{\omega}^{TO_1}, \boldsymbol{\omega}^{TO_2}). \quad (2.8)$$

The reconstruction proceeds by minimizing the objective function  $\mathcal{L}$ ,

$$\min_{\mathbf{U}} \mathcal{L} = \min_{\mathbf{U}} \left[ \frac{\sum_{t, \mathbf{x}, L} |T_m(t, \mathbf{x}; L) - T_{\text{BTE}}(t, \mathbf{x}; L, \mathbf{U})|}{N} + \alpha \left| 1 - \frac{1}{3\kappa} \int_{\omega} C_{\omega} \tau_{\omega}(\mathbf{U}) v_{\omega}^2 d\omega \right| \right], \quad (2.9)$$

where  $T_m(t, \mathbf{x}; L)$  denotes the experimentally measured temperature,  $T_{\text{BTE}}$  is the temperature computed from solution of the BTE (the same temperature in equation (2.4)), and  $N$  is the total number of (independent) measurements available. As indicated above,  $T_m$  is in general a function of space, time, but also the characteristic lengthscale of the thermal relaxation problem,  $L$ . As a result, the optimization process can be based on data for  $T_{\text{BTE}}$  and  $T_m$  at various time instances, spatial locations, and for different characteristic system parameters, with  $\sum_{t, \mathbf{x}, L} 1 = N$ . We also point out that  $T_{\text{BTE}}$  may be obtained by any method that can provide accurate solutions of (2.1) as applied to the experimental setup; here, we consider both semi-analytical solution (using Fourier transform techniques) and MC simulation.

The second term in (2.9) exploits the fact that the bulk value of the thermal conductivity,  $\kappa$ , is usually known, to enhance the importance of the low frequency modes in the optimization. Although this term is ‘‘optional’’, we have found that

including this term with a weight of  $0.01 < \alpha < 1$  improves the reconstruction quality considerably in the low frequency regime, because the low density of states associated with those frequencies prevents them from influencing the optimization process if the objective function only includes a comparison between  $T_{\text{BTE}}$  and  $T_{\text{m}}$  (the first term in (2.9)).

### 2.1.3 Optimization algorithm

Determination of  $\mathbf{U}$  which minimizes the objective function (2.9) is achieved using the Nelder-Mead (NM) algorithm [51], a simplex-based search method that is free from gradient computation. Although NM can neither be categorized as a local optimizer or a global optimizer, it performs significantly better than common local minimizers (which fail to converge to the correct solution in the presence of highly non-convex objective functions such as (2.9)) [52], while it is significantly less costly than common global optimizers like genetic algorithms [53] or simulated annealing algorithms [54].

In the NM algorithm, the optimization process proceeds as follows (adopted from [55]):

1. Start with  $n + 1$  initial points  $\mathbf{p}^k$ ,  $k = 0, \dots, n$ , in the  $n$ -dimensional space defined by the  $n$  unknown parameters (here  $n$  is the dimension of  $\mathbf{U}$  in (2.8);  $n = \dim(\mathbf{U})$ ). A possible choice of initial simplex (the set of  $n + 1$  initial points) is  $\mathbf{p}^0$  and  $\mathbf{p}^k = \mathbf{p}^0 + \delta_k \mathbf{e}_k$  for scalars  $\delta_k$ ,  $k = 1, \dots, n$ ; here  $\mathbf{p}^0$  is an arbitrary point in the  $n$ -dimensional space of unknown parameters and  $\mathbf{e}_k$  is the unit vector in the  $k$ -th direction [56].
2. Order the points  $\mathbf{p}^k$ ,  $k = 0, \dots, n$ , in an ascending order based on their objective function values. Assign new superscripts such that  $\mathcal{L}(\mathbf{p}^0) \leq \dots \leq \mathcal{L}(\mathbf{p}^{n-1}) \leq \mathcal{L}(\mathbf{p}^n)$ .
3. Calculate the centroid of the  $n$  points with lowest objective function values,  $\mathbf{p}^{cn} = \frac{1}{n} \sum_{k=0}^{n-1} \mathbf{p}^k$ .
4. Calculate the reflected point,  $\mathbf{p}^r = \mathbf{p}^{cn} + \mu (\mathbf{p}^{cn} - \mathbf{p}^n)$ , where  $\mu > 0$ .

5. If  $\mathcal{L}(\mathbf{p}^0) \leq \mathcal{L}(\mathbf{p}^r) < \mathcal{L}(\mathbf{p}^{n-1})$ , replace  $\mathbf{p}^n$  with  $\mathbf{p}^r$  and start the next iteration; go to step 2.
6. If  $\mathcal{L}(\mathbf{p}^r) < \mathcal{L}(\mathbf{p}^0)$ , compute  $\mathbf{p}^e = \mathbf{p}^r + \gamma(\mathbf{p}^r - \mathbf{p}^{cn})$ , the expanded point, where  $\gamma > 0$ .
  - (a) If  $\mathcal{L}(\mathbf{p}^e) < \mathcal{L}(\mathbf{p}^r)$ , replace  $\mathbf{p}^n$  with  $\mathbf{p}^e$  and start the next iteration; go to step 2.
  - (b) If  $\mathcal{L}(\mathbf{p}^e) \geq \mathcal{L}(\mathbf{p}^r)$ , replace  $\mathbf{p}^n$  with  $\mathbf{p}^r$  and start the next iteration; go to step 2.
7. If  $\mathcal{L}(\mathbf{p}^r) \geq \mathcal{L}(\mathbf{p}^{n-1})$ 
  - (a) If  $\mathcal{L}(\mathbf{p}^r) < \mathcal{L}(\mathbf{p}^n)$ , compute  $\mathbf{p}^c = \mathbf{p}^{cn} + \rho(\mathbf{p}^r - \mathbf{p}^{cn})$ , the contracted point, where  $0 < \rho < 1$ . If  $\mathcal{L}(\mathbf{p}^c) \leq \mathcal{L}(\mathbf{p}^r)$ , replace  $\mathbf{p}^n$  with  $\mathbf{p}^c$  and start the next iteration; go to step 2. Otherwise, go to step 8.
  - (b) If  $\mathcal{L}(\mathbf{p}^r) \geq \mathcal{L}(\mathbf{p}^n)$ , compute  $\mathbf{p}^{cc} = \mathbf{p}^{cn} + \rho(\mathbf{p}^n - \mathbf{p}^{cn})$ , the new contracted point. If  $\mathcal{L}(\mathbf{p}^{cc}) \leq \mathcal{L}(\mathbf{p}^n)$ , replace  $\mathbf{p}^n$  with  $\mathbf{p}^{cc}$  and start the next iteration; go to step 2. Otherwise, go to step 8.
8. For  $k = 1, \dots, n$ , compute  $\mathbf{v}^k = \mathbf{p}^0 + \sigma(\mathbf{p}^k - \mathbf{p}^0)$  where  $0 < \sigma < 1$ , replace  $\mathbf{p}^k$  with  $\mathbf{v}^k$ , and start the next iteration (go to step 2).

In words, in each iteration, the objective is to eliminate the worst point (with the largest value of objective function) among the current  $n + 1$  points of the simplex via reflection (step 5 or 6b), expansion (step 6a), contraction (step 7) or shrinkage (step 8). Figure 2-1 illustrates this algorithm for the case  $n = 2$ . In the present work, the parameters  $\mu, \gamma$ , and  $\rho$  are taken to be 1, 1, and 0.5, respectively, as proposed in [51, 55, 57]. We have also chosen the shrinkage coefficient to be  $\sigma = 0.9$  as recommended in [57] for robustness in the presence of noise.

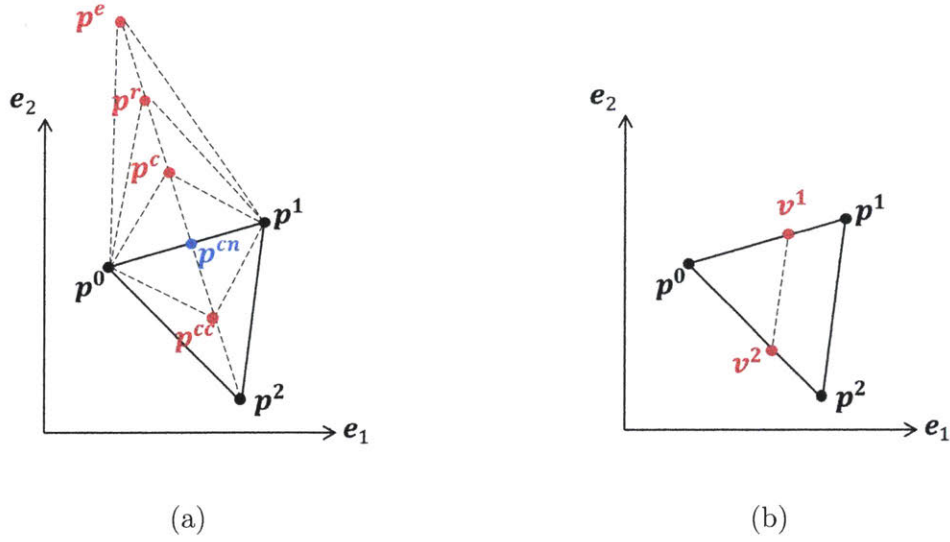


Figure 2-1: An example of simplex update in the NM algorithm; the case of two unknowns (corresponding to  $n = 2$ ) is shown. (a)- Point  $\mathbf{p}^2$  of the previous simplex (which consists of points  $\mathbf{p}^0$ ,  $\mathbf{p}^1$ , and  $\mathbf{p}^2$ ) is replaced with a new point from the set  $\{\mathbf{p}^c, \mathbf{p}^{cc}, \mathbf{p}^r, \mathbf{p}^e\}$ . The new simplex consists of  $\mathbf{p}^0$ ,  $\mathbf{p}^1$ , and the replacement of  $\mathbf{p}^2$ . (b)- If none of the candidate points in figure 5-13a have an objective function smaller than  $\mathcal{L}(\mathbf{p}^2)$ , then the simplex shrinks. The new simplex is  $\mathbf{p}^0$ ,  $\mathbf{v}^1$ , and  $\mathbf{v}^2$ .

The most expensive step in this process is the calculation of the objective function (2.9) which requires evaluation of  $T_{\text{BTE}}$ . The NM algorithm typically requires one or two evaluations of (2.9) at each iteration, except when a shrinkage step takes place where  $\dim(\mathbf{U}) + 2$  evaluations of (2.9) are required. Single function evaluation occurs as a result of successful initial reflection corresponding to step 5 of the algorithm. Two evaluations of the objective function result from either expansion at step 6a, reflection at step 6b, outside contraction at step 7a or inside contraction at step 7b. The simplex typically starts to shrink near the convergence point where it cannot find any new direction that yields lower values of the objective function and consequently, instead, searches for such point inside the previous simplex by shrinking it toward its best vertex [57].

## 2.2 Application example and validation

In this section, we consider the one-dimensional TTG experiment as an example for illustrating and validating the methodology presented in section 2.1. The mathematical model of the TTG experiment will be briefly discussed in section 2.2.1. Using this mathematical formulation, we generate synthetic experimental data; this process is described in section 2.2.2. We then use these synthetic data to reconstruct  $\tau_\omega$  for the material model used in the MC simulations; the details of the reconstruction process are discussed in section 2.2.3. We consider reconstruction both via semi-analytical solution of the BTE and MC simulation; the advantages of each approach are discussed and contrasted. In section 2.2.4, we compare the reconstructed relaxation times and free path distribution with those of the original data used in the MC simulations for generating the synthetic data.

### 2.2.1 The TTG experiment

Transient thermal grating (TTG) experiment has been widely used to study transient thermal transport. In this experiment, a sinusoidal profile with unit amplitude is generated by crossing two short pump pulses [27] (see figure 2-2).

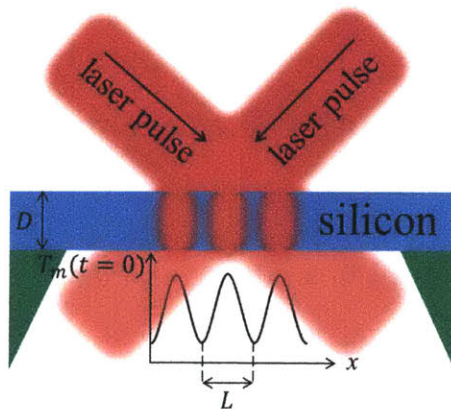


Figure 2-2: The TTG experiment; a sinusoidal temperature profile ( $T_m$  in the figure) with different wavelengths ( $L$ ) is created at time  $t=0$  via crossing two varying angled pump pulses. A fast detector measures the combined diffracted probe light and the reference beam [10]. The Si film thickness is constant at  $D$ . In the case of 1D-TTG (this chapter), the transport is one-dimensional,  $D \rightarrow \infty$ .

By assuming a one-dimensional heat transport along the  $x$  direction, the BTE from equation (2.1) can be written in the form

$$\frac{\partial e^d}{\partial t} + v_\omega \cos(\theta) \frac{\partial e^d}{\partial x} = -\frac{e^d - (de^{\text{eq}}/dT)_{T_{\text{eq}}} \Delta \tilde{T}}{\tau_\omega} + (de^{\text{eq}}/dT)_{T_{\text{eq}}} \delta(t) \exp(2\pi i x/L), \quad (2.10)$$

in which the last term is due to the sinusoidal initial temperature profile. Here,  $L$  is the grating wavelength (see discussion in section 2.1.2), and  $i$  is the imaginary unit. This equation is sufficiently tractable to allow analytical solutions in Fourier/reciprocal space [28, 37]. We follow a similar procedure (see Appendix B) to obtain a Fourier space solution for  $T_{\text{BTE}}$ ; the final result is

$$\Delta T_\zeta = \frac{e^{2\pi i x/L}}{C} \left[ \int_\omega S_\omega \tau_\omega^2 d\omega + \frac{(\int_\omega S_\omega \tau_\omega d\omega)^2}{\int_\omega [C_\omega \tau_\omega^{-1} - S_\omega] d\omega} \right], \quad (2.11)$$

where  $C = \int_\omega C_\omega d\omega$  is the volumetric heat capacity and  $\Delta T_\zeta = \Delta T(\zeta, x)$  denotes the Fourier transform of  $\Delta T(t, x)$  with respect to the time variable. Also,  $S_\omega = S(\omega, \zeta)$  is given by

$$S_\omega = \frac{i C_\omega L}{4\pi v_\omega \tau_\omega^2} \ln \left( \frac{\tau_\omega \zeta - v_\omega \tau_\omega 2\pi L^{-1} - i}{\tau_\omega \zeta + v_\omega \tau_\omega 2\pi L^{-1} - i} \right). \quad (2.12)$$

We note here that the temperature profile required for evaluating (2.9) is given by  $T_{\text{BTE}}(t, x) = \Delta T(t, x) + T_{\text{eq}}$ .

## 2.2.2 Generation of synthetic experimental data

Instead of using experimental data (for  $T_{\text{m}}$ ) to validate the proposed methodology, we use synthetic data generated from MC simulation of (2.10). This approach enables considerably more precise validation because it sidesteps issues of experimental error, which is hard to quantify, but also modeling error (how accurately does (2.10) model the TTG experiment?), which is even harder to quantify. In other words, reconstruction from  $T_{\text{m}}$  “measurements” obtained from MC simulations should be able to reproduce the function  $\tau_\omega$  used to generate the synthetic data exactly, making any discrepancies directly attributable to numerical/methodological error.

In the interest of simplicity, the material was assumed to be silicon. However, in order to fully explore the ability of the reconstruction process to capture arbitrary functional relations  $\tau_\omega = \tau(\omega)$ , we consider both a simple analytical model and an *ab initio* model of this material. The simple model considered here is described in [29,39] (thermal conductivity  $\kappa = 143.8 \text{ Wm}^{-1}\text{K}^{-1}$ ) and will be referred to as the Holland model. The second model considered (thermal conductivity  $\kappa = 139.7 \text{ Wm}^{-1}\text{K}^{-1}$ ) is described in [28] and will be referred to as the *ab initio* model throughout this work.

Mirroring the experimental procedure as closely as possible, we obtain transient temperature relaxation data (solutions of (2.10)) at one spatial location for a number of characteristic (grating) lengths, namely  $T_m(0 \leq t \leq t_L; L)$  ( $= T_m(0 \leq t \leq t_L, x = 0; L)$  for example). These solutions were obtained using the adjoint Monte Carlo method recently proposed [32] that is particularly efficient if solutions at particular spatial locations are of interest. The MC simulations used a sufficiently high number of particles ( $\mathcal{N}_m = 10^9$ ) to ensure that the synthetic data was essentially noise free ( $\mathcal{N}_m$  is the number of particles used in the MC simulations for *generating synthetic “experimental” data*). As discussed in section 2.2.4, we have also produced noisy synthetic data using significantly fewer particles in order to investigate the robustness of the optimization method to noise. Relaxation data was “recorded” in the time period  $0 \leq t \leq t_L$ , where  $t_L = \min(t_{L,1\%}, 5 \text{ ns})$ ; here,  $t_{L,1\%}$  denotes the time taken for the response to decay to 1% of its original amplitude for each  $L$ . During this time period, 100 discrete  $T_m$  measurements were obtained. Eight different wavelengths were simulated, namely,  $L = 10 \text{ nm}, 50 \text{ nm}, 100 \text{ nm}, 500 \text{ nm}, 1 \mu\text{m}, 5 \mu\text{m}, 10 \mu\text{m}$ , and  $50 \mu\text{m}$ . As a result, 800 total  $T_m$  measurements were available for reconstruction ( $N = 800$ ).

### 2.2.3 Reconstruction

Reconstruction proceeds by comparing solutions of 1-D TTG experiment, equation (2.10), in the form of  $T_{\text{BTE}}(0 \leq t \leq t_L; L, \mathbf{U})$  to the counterpart  $N$  measurements of  $T_m$  as a means of finding the optimum unknown vectors. Here, solutions of (2.10) were obtained using inverse fast Fourier transform (IFFT) of (2.11) as explained in [58], or

by using adjoint MC simulations [32]. Although MC simulations are more expensive, they are investigated here because they make the proposed method significantly more general, since they are not limited to problems which lend themselves to analytical or semi-analytical solutions.

As discussed before, phonon group velocities were assumed known, while  $\tau_\omega$  was described by the model given in (2.7) with  $M^{LA} = M^{TA_1} = M^{TA_2} = 3$  (a piecewise linear function with three segments) and  $M^{LO} = M^{TO_1} = M^{TO_2} = 0$ . As shown in section 2.2.4, this approximation level gives very good results. We have not considered optical phonons in this section because acoustic modes account for most of the heat conduction [50], but also because the proposed methodology can be straightforwardly extended to include them. Although the inclusion of additional unknowns is expected to have an effect on the complexity of the optimization calculation, as long as the number of additional unknowns is not large, this is manageable. Moreover, the weaker dependence of optical phonons on frequency allows a simpler model introducing less unknowns than an additional acoustic branch. This approach also makes sense from the point of view that the contribution of optical phonons to transient transport is small and thus probably insufficient for the determination of an inverse problem with many unknowns (see the discussion and results in Chapter 4).

To generate the initial starting points ( $\dim(\mathbf{U}) + 1$  vertices of the simplex), we have used  $\delta_k = 0.1p_k^0$  as recommended in [56], where  $p_k^0$  represents the  $k$ -th component of vector  $\mathbf{p}^0$  as discussed in the first step of the NM algorithm in section 2.1.3. Larger values of  $\delta_k$  (we have tested  $\delta_k = 10p_k^0$ ) may lead to large steps during the initial iterations of the optimization, which consequently can move the simplex toward a wrong local minimum; on the other hand, very small values of  $\delta_k$  (we have tested  $\delta_k = 0.001p_k^0$ ) lead to smaller steps throughout the optimization process, which require a (significantly) larger number of iterations in order to guarantee that the parameter space is adequately sampled. We have obtained similar performances to  $\delta_k = 0.1p_k^0$  using  $\delta_k = 0.05p_k^0$  and  $\delta_k = 0.025p_k^0$ .

We have used a graduated [59] (multi-stage) optimization framework. In particular, we perform the optimization in four stages. In the first stage, we solve for one

segment ( $M^{LA} = M^{TA_1} = M^{TA_2} = 1$ ) which is the same for all branches, leading to only two unknown parameters. Due to the small number of unknowns, this step is very cheap but very valuable since it results in a significant reduction in the value of objective function in only 10–20 iterations. In the second stage,  $LA$  and  $TA$  modes are still assumed to be the same but the intended number of segments is used, increasing the number of unknowns to  $2M^{LA}$  (or  $2M^{TA_1}$ ,  $2M^{TA_2}$ ) —six in the present case. The initial condition for this stage is taken to be the same as the optimized value of the previous stage (or a slightly perturbed version). In the third stage, we repeat the optimization process, now for  $2M^{LA} + 2M^{TA}$  unknowns (the two  $TA$  branches are assumed to be the same,  $\tau_\omega^{TA_1} = \tau_\omega^{TA_2}$ ), starting from the optimized parameters of the second stage<sup>1</sup>. Finally, we perform the optimization for all  $2(M^{LA} + M^{TA_1} + M^{TA_2})$  unknowns starting from the optimized parameters of the previous stage (repeated for each of the three branches independently). This procedure is more robust than direct optimization for  $2(M^{LA} + M^{TA_1} + M^{TA_2})$  unknowns, which depending on the initial condition may be trapped in a local minimum of (2.9) characterized by significantly different relaxation times for the  $LA$  and  $TA$  branches.

To reduce the probability of the reconstruction being trapped in a local minimum, in our approach, the first and second stages were repeated starting from 5 distinct initial conditions. The result at each stage with the lowest value of  $\mathcal{L}$  was used as the initial condition for the next stage. Although this consideration may not be necessary, it is expected to improve the quality of the optimization process (by providing a smaller final value of  $\mathcal{L}$ ) due to the non-convexity of the objective function.

Although the number of iterations varies depending on the initial condition, we have observed that for the values of  $M^S$  used in our work (corresponding to 18 unknowns), the third and fourth stages require on the order of 150–200 iterations for convergence (each). When using analytical or semi-analytical (IFFT) solutions for  $T_{\text{BTE}}$ , the computational cost associated with each evaluation is very small and thus

---

<sup>1</sup>Note that for the material considered here (silicon), the range of the  $TA$ -mode frequencies is smaller than that of  $LA$  modes. As a result, the  $TA$ -mode portion of the solution at the second stage may only consist of one or two line segments; in these cases, we may need to introduce one or two additional segmentation points on this solution to ensure a piecewise linear model with three line segments.

cost is not a consideration. Using MC simulation to obtain solutions for  $T_{\text{BTE}}$  is more costly and is discussed below.

**Reconstruction using MC simulations** To reduce cost, MC simulations during the first two stages of the optimization process used  $\mathcal{N}_{\text{BTE}} = 10^4$  particles for calculation of  $T_{\text{BTE}}$ . During the third and fourth stages of the process, the number of particles is increased to  $\mathcal{N}_{\text{BTE}} = 10^6$ .

Figure 2-3 investigates the sensitivity of the final value of the objective function  $\mathcal{L}$  in the third stage as a function of the number of particles used (in this stage of the optimization) for the *ab initio* material model. Specifically, the figure compares the mean and variance of the objective function compared to the third-stage final value obtained from IFFT of (2.11) (which is free from noise and independent of number of particles). The MC result appears to converge (asymptotically) to the deterministic result with increasing number of computational particles,  $\mathcal{N}_{\text{BTE}}$ . Although this convergence appears to be slow, it is encouraging that the additional error (compared to deterministic reconstruction) is small and thus the shallow slope of the convergence implies that the reconstruction is quite robust to noise in the range  $10^4 \leq \mathcal{N}_{\text{BTE}} \leq 10^6$ .

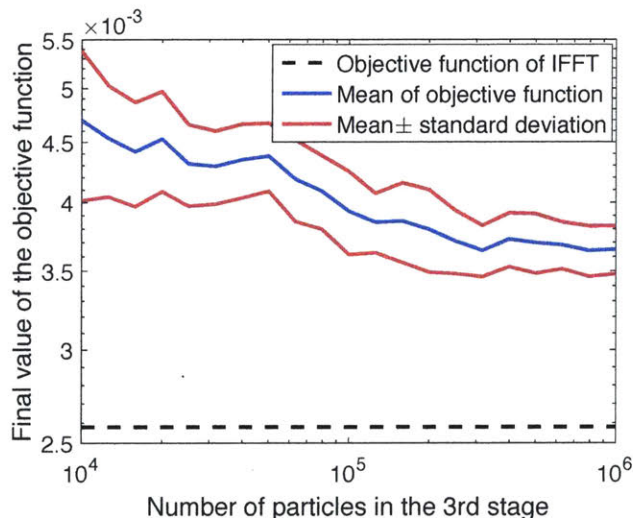


Figure 2-3: Dependence of the final value of  $\mathcal{L}$  at the third stage on  $\mathcal{N}_{\text{BTE}}$ . Increasing the number of particles decreases the mean and variance of  $\mathcal{L}$ .

Since the computational time for each adjoint MC simulation is proportional to

$\mathcal{N}_{\text{BTE}}$  [32], given our choices for  $\mathcal{N}_{\text{BTE}}$  ( $\mathcal{N}_{\text{BTE}} = 10^4$  for stages 1 and 2 and  $\mathcal{N}_{\text{BTE}} = 10^6$  for stages 3 and 4), the cost of the first two stages of the optimization is negligible compared to the cost of the last two stages. Here we note that no attempt has been made to optimize this process; it is therefore possible that considerably more computational benefits may be possible if a more structured approach is used [60] that takes into account information such as that contained in figure 2-3. We also note that given the small cost of the first two optimization stages, repeating them a number of times starting from different initial conditions does not increase the cost of the reconstruction process significantly.

For an average of 150–200 iterations, the cost of each of the third or fourth stages corresponds to 300–600 MC simulations, considering that on average 2–3 evaluations of (2.9) at each iteration are required. This number of iterations can be performed efficiently using the adjoint method proposed recently in [32]. Note that a significant fraction of the computational effort is spent on iterations close to the final solution, which is primarily due to the high computational cost of the shrinkage step near convergence as was discussed previously in section 2.1.3 (compare  $2(M^{LA} + M^{TA_1} + M^{TA_2}) + 2 = 20$  function evaluations associated with the shrinkage step, with one or two function evaluations associated with reflection, expansion or contraction). In contrast to the present case where validation required very small error tolerances, in actual practice, tolerances will be set by experimental considerations and are expected to be larger, reducing the number of expensive shrinkage processes and making the cost of reconstruction from experimental data smaller.

## 2.2.4 Validation

In this section, we discuss reconstruction results with particular emphasis on their ability to reproduce the original material properties ( $\tau_\omega = \tau(\omega)$ ) used to generate the synthetic measurements  $T_m$ , referred to as “true”. Although our scheme returns  $\tau_\omega$  as output, as is typical in the literature, we also provide comparison between the “true” and “reconstructed” cumulative distribution function (CDF) of free paths defined as  $F(\Lambda) := \frac{1}{3\kappa} \int_{\omega^*(\Lambda)} C_\omega v_\omega^2 \tau_\omega d\omega$ , where  $\omega^*(\Lambda)$  is the set of modes such that

$$\omega^*(\Lambda) = \{\omega | \Lambda_\omega \leq \Lambda\}.$$

**Holland model** Here, we present results for the Holland material model. For this model, we assumed that the two  $TA$  branches are the same and as a result, the optimization process consists of three stages with a total of 12 unknowns.

Figure 2-4 shows a comparison between the true material parameters and the reconstructed ones using the semi-analytical solution (2.11) for  $T_{\text{BTE}}$ . The agreement is excellent.

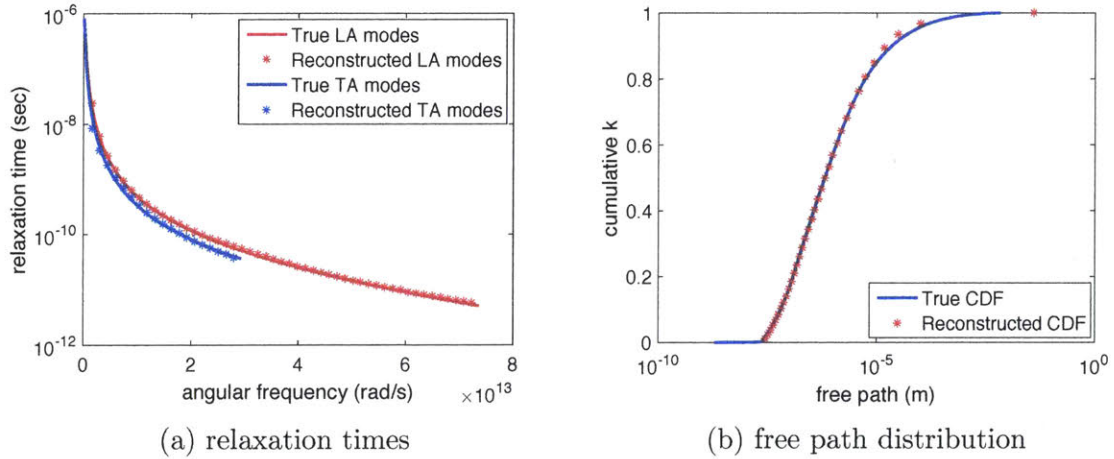


Figure 2-4: Comparison between true and reconstructed relaxation times and free path distribution using IFFT of the semi-analytical result (2.11) for the Holland material model.

Figure 2-5 shows a similar comparison for the case where MC simulations were used for obtaining  $T_{\text{BTE}}$ . We observe that the error in reconstructed relaxation times is more significant when using MC simulations. We attribute this primarily to the noise associated with MC simulation and its interaction with the NM algorithm.

The synthetic data used to obtain the results in figures 2-4 and 2-5 were generated by MC simulations using  $\mathcal{N}_m = 10^9$  computational particles. This high number of computational particles leads to a very small variance, corresponding to a very accurate “experimental measurement”. In order to evaluate the performance of the reconstruction method in the presence of noise in the experimental measurement, we have also performed reconstruction calculations with noisy synthetic data. For that

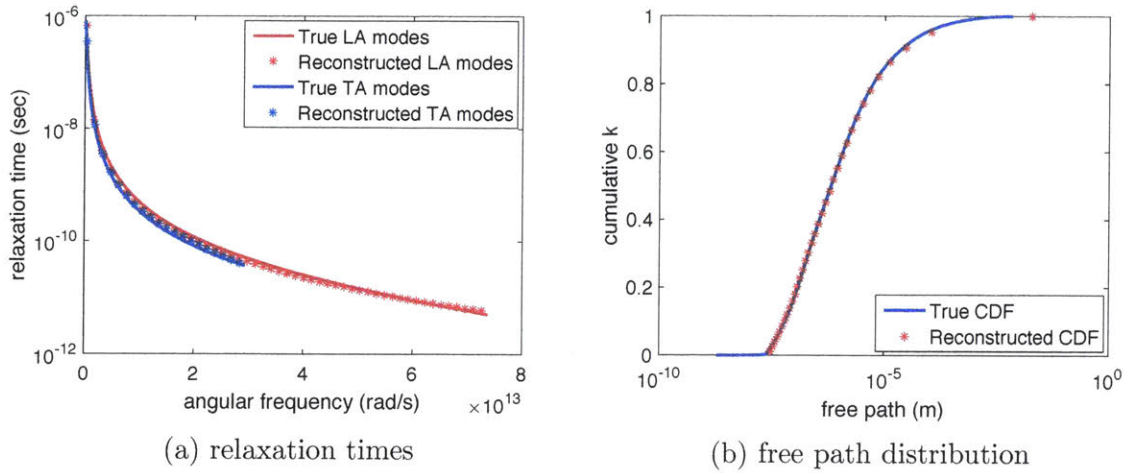


Figure 2-5: Comparison between true and reconstructed relaxation times and free path distribution using  $T_{\text{BTE}}$  obtained from adjoint MC simulation using the Holland material model.

purpose, we have used only  $\mathcal{N}_m = 10^3$  computational particles in the MC simulations that generated the synthetic data, leading to a standard deviation of 0.02 K. This number of particles makes the uncertainty in  $T_m$  significantly larger than the noise in common experimental data (e.g. compare the noisy temperature profile of figure 2-6 with figure 2c of [19]). Figure 2-6 shows a comparison between the synthetic data obtained with  $\mathcal{N}_m = 10^9$  and  $\mathcal{N}_m = 10^3$  particles.

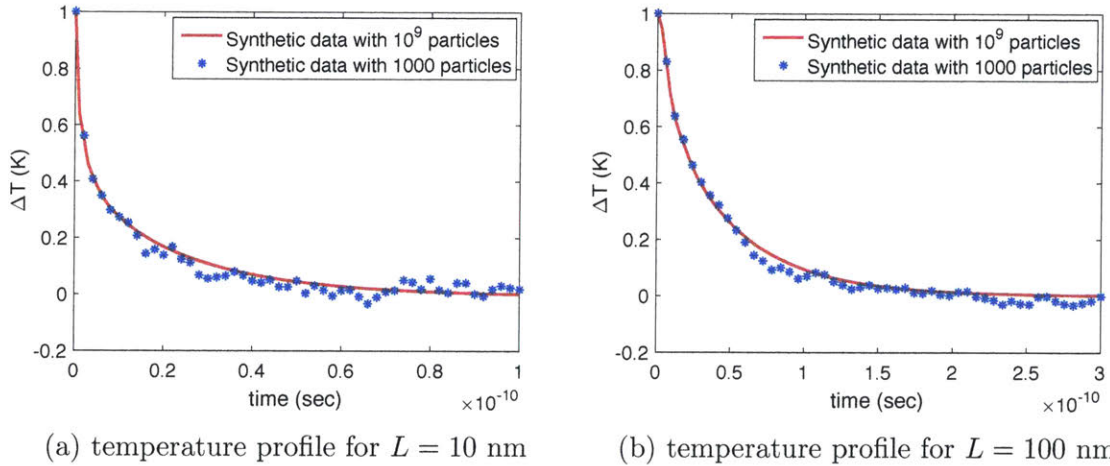


Figure 2-6: Comparison of the synthetic temperature profile obtained by MC simulations using  $\mathcal{N}_m = 10^9$  and  $\mathcal{N}_m = 10^3$  computational particles based on the Holland material model. Two different grating wavelengths are shown.

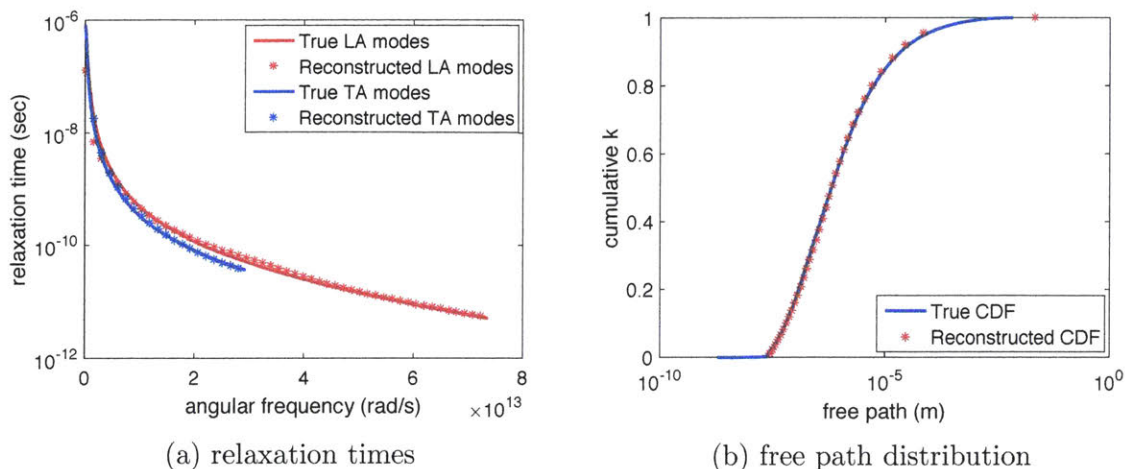


Figure 2-7: Comparison between true and reconstructed relaxation times and free path distribution using IFFT of (2.11) from noisy synthetic data for the Holland material model.

The reconstructed relaxation times and free path distribution corresponding to the noisy synthetic data ( $\mathcal{N}_m = 10^3$ ) using semi-analytical and MC solutions with the Holland material model are provided in figures 2-7 and 2-8, respectively. In both figures we observe that even in the presence of the considerable noise in the measurement, the algorithm is able to infer the relaxation times and the free path distribution with reasonable accuracy.

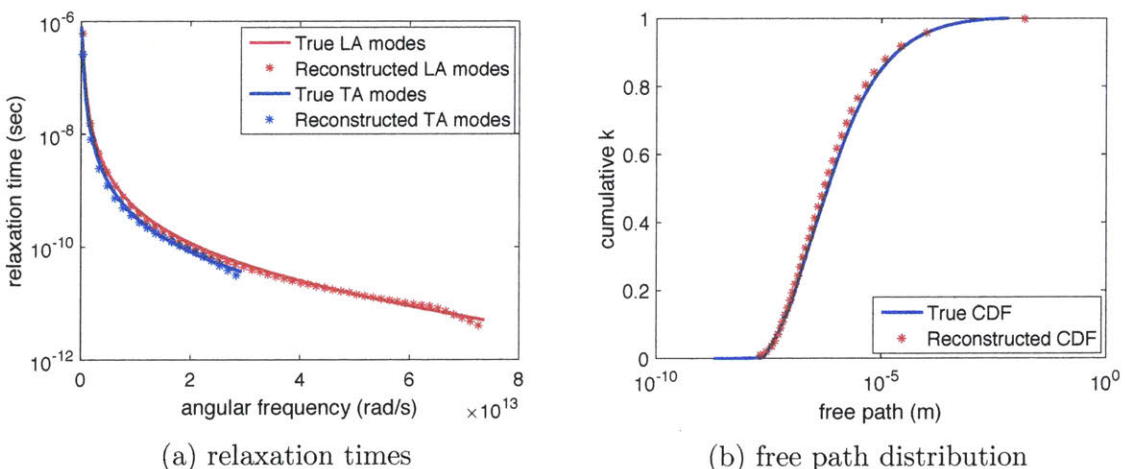


Figure 2-8: Comparison between true and reconstructed relaxation times and free path distribution using adjoint MC simulation from noisy synthetic data for the Holland material model.

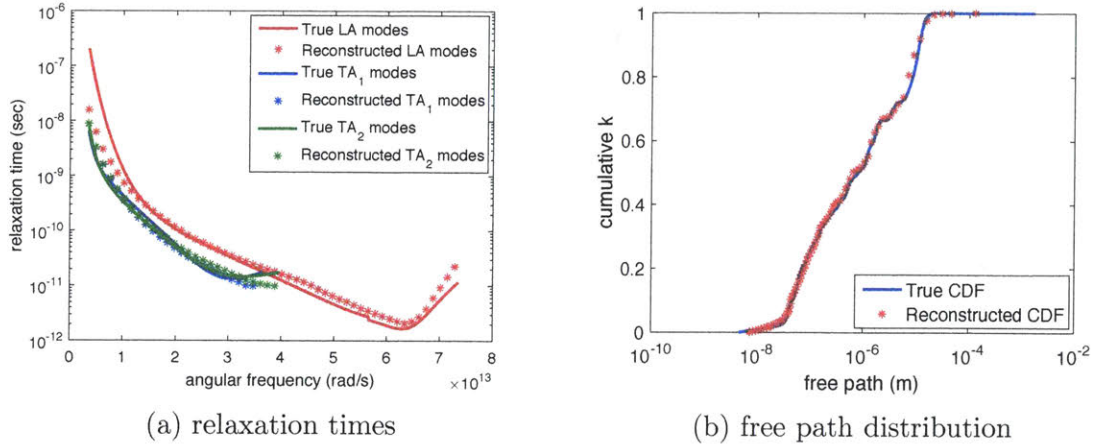


Figure 2-9: Comparison between true and reconstructed relaxation times and free path distribution using IFFT of (2.11) with the *ab initio* material model.

**Ab initio model** In this section, we repeat the validation process, namely using IFFT of (2.11) and adjoint MC simulation in the presence and absence of noise in the synthetic data, for the *ab initio* material model. The reconstructed material properties in the absence of noise ( $\mathcal{N}_m = 10^9$ ) are provided in figures 2-9 and 2-10. The reconstructed material properties in the presence of noise ( $\mathcal{N}_m = 10^3$ ) using IFFT of (2.11) and MC simulation are provided in figures 2-11 and 2-12, respectively.

We observe that the general level of agreement is very good, but not at the level of the Holland model discussed in section 2.2.4. This is clearly to be expected given

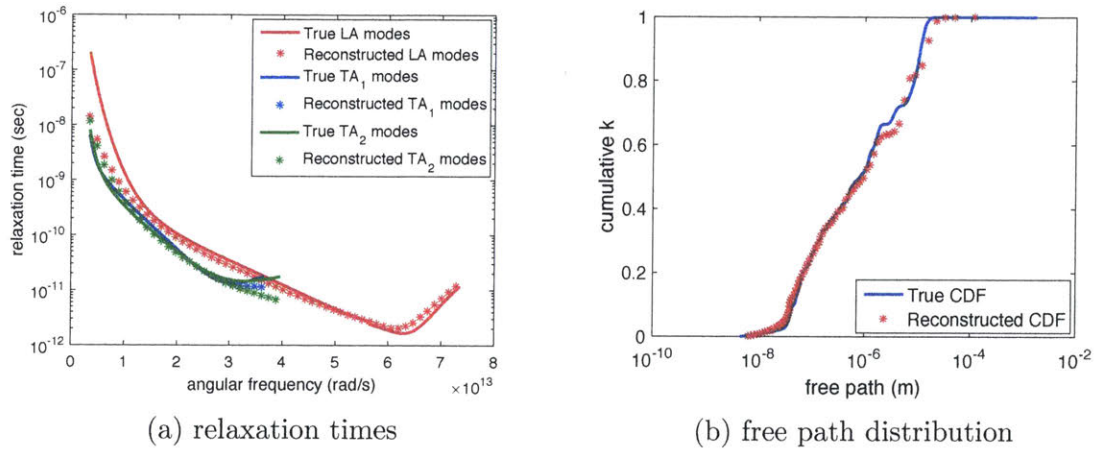


Figure 2-10: Comparison between true and reconstructed relaxation times and free path distribution using  $T_{\text{BTE}}$  obtained from adjoint MC simulation of the *ab initio* material model.

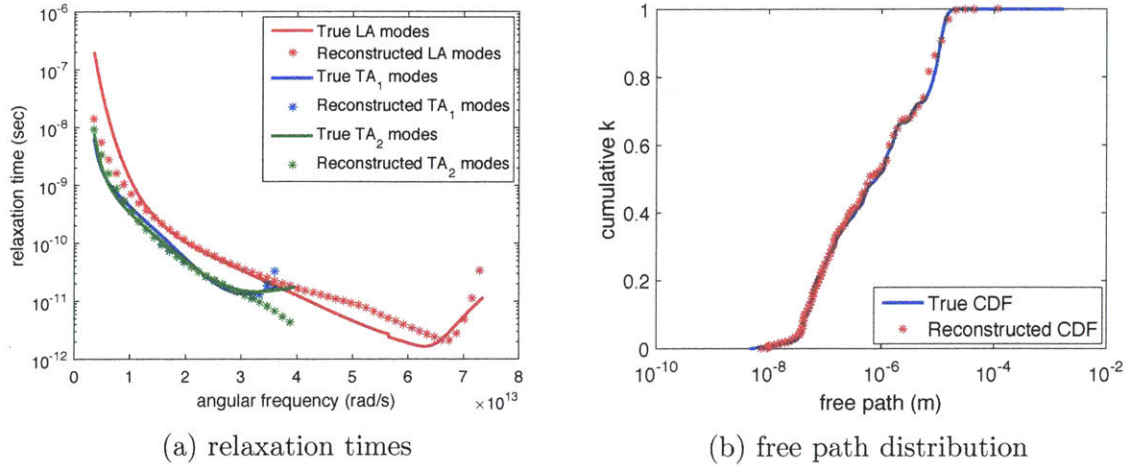


Figure 2-11: Comparison between true and reconstructed relaxation times and free path distribution using IFFT of (2.11) from noisy synthetic data for the *ab initio* material model.

the relative complexity of the two models and the fact that the parametrization (2.7) is related to the Holland model in limiting cases. We also note that although the discrepancy is particularly noticeable for low frequencies, this is primarily an artifact of the low density of states of modes in these frequency ranges. Specifically, the density of states of the *LA* modes for  $\omega \leq 8 \times 10^{12}$  rad/s is zero (i.e. none of the two terms in (2.9) influences  $\tau_{\omega}^{LA}$  for  $\omega \leq 8 \times 10^{12}$ ). The role of density of states

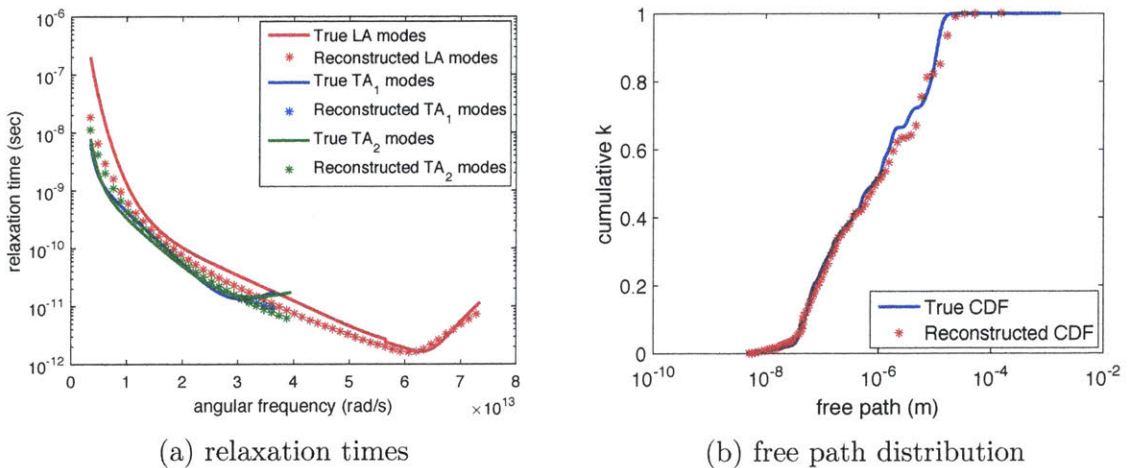


Figure 2-12: Comparison between true and reconstructed relaxation times and free path distribution using adjoint MC simulation from noisy synthetic data for the *ab initio* material model.

can be further verified by noting that the reconstructed free path distribution is in all cases in better agreement with the input (“true”) data compared to the corresponding relaxation times.

We also observe that, as in the case of the Holland model, the noise in the synthetic data has only a small effect on the reconstruction quality.

## 2.3 Comparison to effective thermal conductivity approach

The accuracy of the reconstruction process shown in figures 2-4, 2-5, 2-7–2-12 is very encouraging and, generally speaking, superior to that obtained by effective-thermal-conductivity-based approaches (see, for example, figure 2 in [13], or figure 2-13 of the present work). In [13], it is pointed out that the effective-thermal-conductivity-based approach is less accurate outside the range of lengthscales over which input data is available and thus the discrepancies observed in [13] may be attributed to the lack of data in the range  $L \lesssim 1 \mu\text{m}$  and  $L \gtrsim 15 \mu\text{m}$ . On the other hand, as shown in figure 2-13, reconstruction using the method proposed here using relaxation data for  $L = 1 \mu\text{m}, 5 \mu\text{m}, 10 \mu\text{m},$  and  $50 \mu\text{m}$ , reveals that the proposed method is less sensitive to the range of wavelengths spanned by the input data.

Sensitivity to the range over which input data exists is very important, not only because some lengthscales may not be experimentally accessible [13], but also because the effective thermal conductivity concept cannot be used to analyze small lengthscale or early-time data—recall that Fourier-based descriptions are only accurate in the limit of large lengthscales (compared to the mean free path) and long timescales (compared to the mean time between scattering events). Below, we theoretically analyze the limitations arising from these requirements by studying in detail the response associated with the TTG setup.

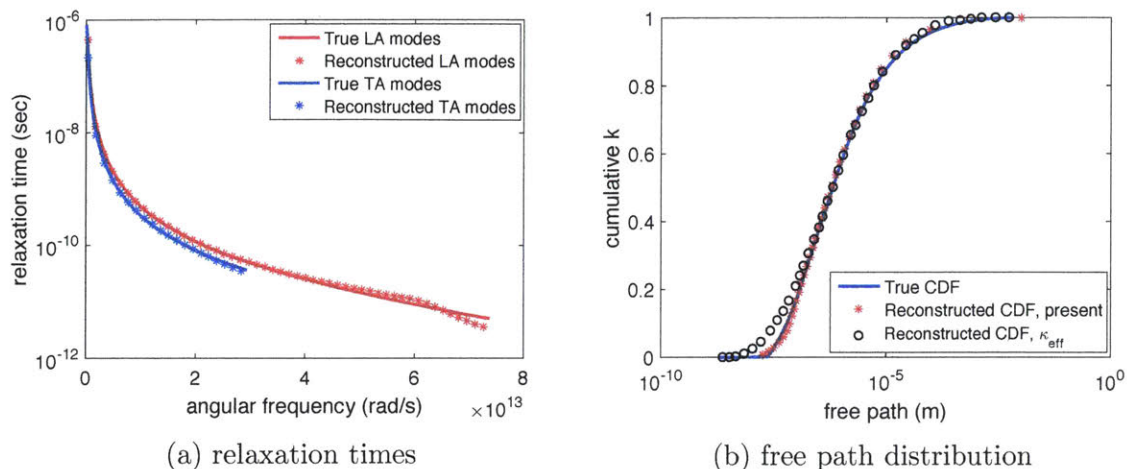


Figure 2-13: Comparison between true and reconstructed data for the case of limited range of input wavelengths: (a) Reconstructed relaxation times using IFFT of the semi-analytical result (2.11) for the Holland material model using  $L = 1 \mu\text{m}, 5 \mu\text{m}, 10 \mu\text{m},$  and  $50 \mu\text{m}$ . Relaxation data was “recorded” in the time period  $0 \leq t \leq t_L$ , where  $t_L = \min(t_{L,1\%}, 50 \text{ ns})$ ; (b) Comparison of the free path distribution obtained from reconstruction shown in (a) with data transcribed [61] from figure 2 of [13] (denoted “Reconstructed CDF,  $\kappa_{\text{eff}}$ ”), obtained from the effective thermal conductivity approach using 12 relaxation profiles with wavelengths in the range  $L = 1 - 15 \mu\text{m}$ .

Another problem associated with the effective thermal conductivity approach is that, other than in the thermal grating geometry, the associated suppression functions are unknown (and depend not only on the experimental setup, but also on the material parameters that are being calculated). Using gray MC simulations as a substitute for the suppression function introduces approximations (see [28] for a discussion) that are not always acceptable and more importantly not *a priori* controllable.

**The thermal grating case in detail** Clearly, in order to extract information from the experiment correctly, a model needs to be able to fit the functional form of the experimental response accurately. We now examine, both theoretically and via simulation, if this requirement is satisfied by the effective thermal conductivity formalism in the case of the TTG problem.

We first recall that the effective thermal conductivity concept applies to late times, as defined by  $\tau_\omega \zeta \ll 1$  [37] ( $\zeta$  is the Fourier transform variable with respect to time

—see discussion in section 2.2.1). Following previous work [37], we simplify (2.12) in the limit of  $\tau_\omega \zeta \ll 1$  to obtain (see Appendix C)

$$S_\omega = \frac{C_\omega}{\tau_\omega} \left[ \frac{\tan^{-1}(\text{Kn}_\omega)}{\text{Kn}_\omega} - \frac{\tau_\omega}{\text{Kn}_\omega^2 + 1} i\zeta \right]. \quad (2.13)$$

Here,  $\text{Kn}_\omega = 2\pi v_\omega \tau_\omega / L$ . Substituting equation (2.13) in (2.11) and performing the inverse Fourier transform in time leads to the following temperature response in the *late time limit*  $t \gg \tau_\omega$

$$\Delta T = A \exp\left(\frac{2\pi i x}{L}\right) \exp\left(-\left(\frac{2\pi}{L}\right)^2 \frac{\kappa_{\text{mod}}}{C_{\text{mod}}} t\right), \quad (2.14)$$

where

$$\kappa_{\text{mod}} = \int_\omega \frac{1}{3} C_\omega v_\omega^2 \tau_\omega \left\{ \frac{3}{\text{Kn}_\omega^2} \left[ 1 - \frac{\tan^{-1}(\text{Kn}_\omega)}{\text{Kn}_\omega} \right] \right\} d\omega \quad (2.15)$$

is the effective thermal conductivity as found before [37],

$$A = \frac{\left[ \int_\omega \frac{C_\omega \tau_\omega}{\text{Kn}_\omega^2 + 1} d\omega \int_\omega \frac{C_\omega}{\tau_\omega} \left( 1 - \frac{\tan^{-1}(\text{Kn}_\omega)}{\text{Kn}_\omega} \right) d\omega + \int_\omega \frac{C_\omega}{\text{Kn}_\omega^2 + 1} d\omega \int_\omega \frac{C_\omega}{\text{Kn}_\omega} \tan^{-1}(\text{Kn}_\omega) d\omega \right]^2}{\left[ \int_\omega \frac{C_\omega}{\text{Kn}_\omega^2 + 1} d\omega \right]^3} \quad (2.16)$$

is the response amplitude, and

$$C_{\text{mod}} = \int_\omega \frac{C_\omega}{\text{Kn}_\omega^2 + 1} d\omega \quad (2.17)$$

is an effective heat capacity.

In other words, although the response (2.14) is of exponential form in time, it is not a solution of the Fourier heat equation with an effective thermal conductivity  $\kappa_{\text{mod}}$ , as usually assumed. Response (2.14) is a diffusive type of solution which differs from the classical Fourier solution by featuring

- an amplitude,  $A$ , different from the original temperature perturbation in the TTG experiment (taken to be 1 K here)
- a thermal conductivity given by  $\kappa_{\text{mod}}$

- a heat capacity given by  $C_{\text{mod}}$

Moreover, we always need to keep in mind that the above is only true for  $\tau_\omega \zeta \ll 1$ , which turns out to have significant implications. Using the fact that  $\kappa_{\text{mod}}/C_{\text{mod}} \sim O(\kappa/C) \sim \langle \Lambda_\omega \rangle^2 / \langle \tau_\omega \rangle$  we can write (2.14) in the form

$$\Delta T \sim A \exp\left(\frac{2\pi i x}{L}\right) \exp\left(-\pi^2 \text{Kn}^2 \frac{t}{\langle \tau_\omega \rangle}\right), \quad (2.18)$$

where  $\text{Kn} = \langle \Lambda_\omega \rangle / L$  is the (average) Knudsen number,  $\langle \Lambda_\omega \rangle$  is the mean free path and  $\langle \tau_\omega \rangle$  is the mean free time. This leads us to conclude that the requirement  $t/\tau_\omega \gg 1$  ( $t/\langle \tau_\omega \rangle \gg 1$ ) is incompatible with a solution of this form ( $\Delta T \rightarrow 0$ ) unless  $\text{Kn}^2 \ll 1$ . This “mathematical” incompatibility is a simple statement of the physical fact that relaxation times scale with the system size and thus for a small system not satisfying  $\text{Kn}^2 \ll 1$  the response timescale will be on the order of the relaxation time or smaller (no experimentally measurable signal will be available at times much longer than the relaxation time) —in other words, no fully diffusive relaxation regime is possible for systems not satisfying  $\text{Kn}^2 \ll 1$ .

The above discussion is validated in figures 2-14 and 2-15; the figures compare various Fourier-based relaxation profiles to the BTE solution of the grating relaxation problem for various values of the wavelength  $L$ . In addition to solution (2.14), we also consider the traditional effective thermal conductivity approach given by [37],

$$\Delta T = \exp\left(\frac{2\pi i x}{L}\right) \exp\left(-\left(\frac{2\pi}{L}\right)^2 \frac{\kappa_{\text{mod}}}{C} t\right). \quad (2.19)$$

The figures also show the solution of the same problem obtained via IFFT of (2.11) using the *reconstructed*  $\tau_\omega$  data (as shown in figure 2-4 for the Holland model and figure 2-9 for the *ab initio* model). Figure 2-14 shows results for the *ab initio* material model ( $\langle \Lambda_\omega \rangle = 95.7$  nm) and figure 2-15 for the Holland model ( $\langle \Lambda_\omega \rangle = 85.5$  nm). Here,  $\langle \Lambda_\omega \rangle$  was calculated using the procedure outlined in [62].

In both figures, we observe that the BTE solution based on reconstructed relaxation times, referred to as “present”, is the only solution that is able to predict the

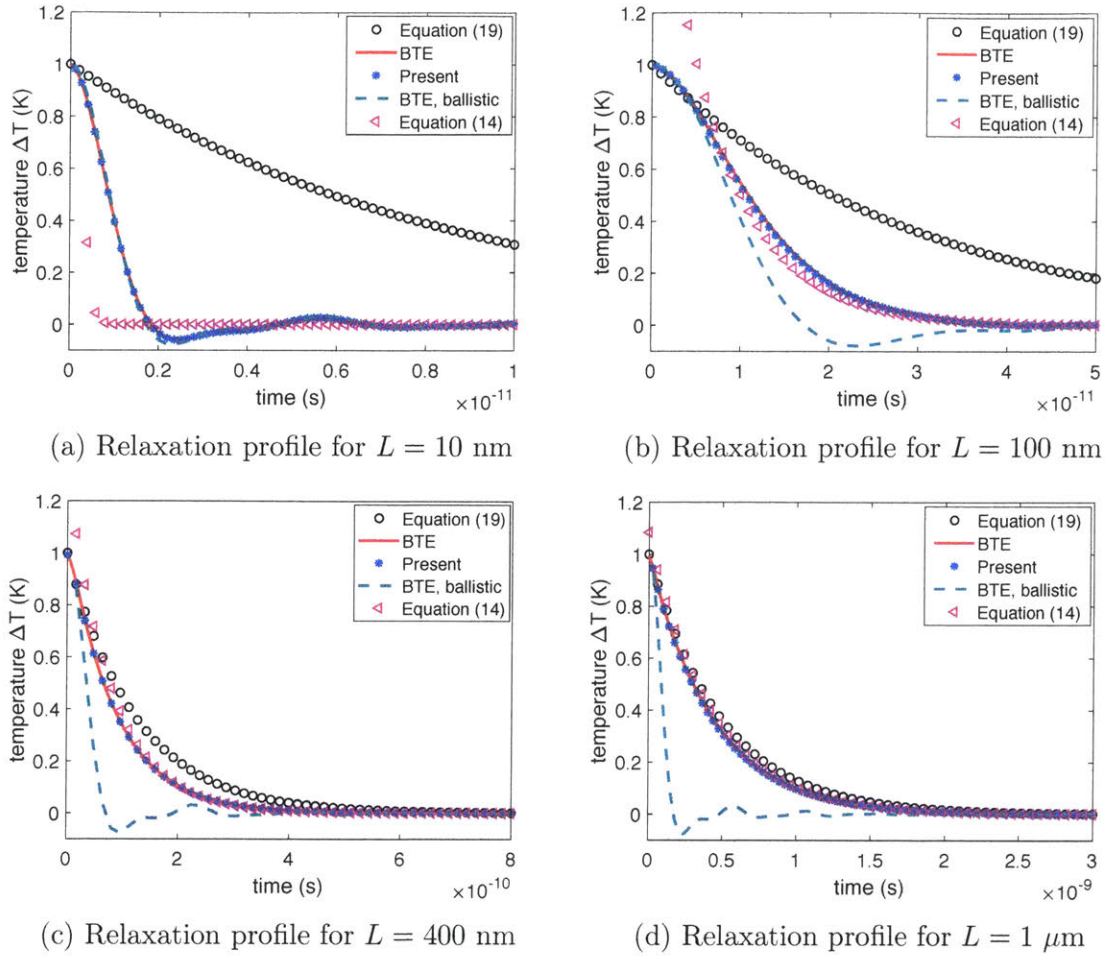


Figure 2-14: Comparison between the method proposed in the present work and various Fourier-based methods. Temperature relaxation profiles are shown for four grating wavelengths and compared to BTE solution for the *ab initio* material model (denoted “BTE”). The prediction of the method proposed here, denoted as “present”, is given by solution of the Boltzmann equation based on the reconstructed relaxation time data of figure 2-9. Solutions based on equations (2.14) and (2.19) are denoted “Equation (2.14)” and “Equation (2.19)”, respectively.

correct temperature profiles (IFFT of (2.11), denoted by “BTE”) in all Kn-regimes, for all times. Referring to figure 2-14, at  $L = 10$  nm, the ballistic solution of the BTE (provided in Appendix D) is also able to predict the temperature profile, although for  $t \gtrsim 1.5$  ps some discrepancies are observable (scattering is no longer completely negligible); Fourier-based approximations are inaccurate. For  $L = 100$  nm ( $\text{Kn} \approx 0.96$ ), none of the Fourier-based approximations are able to predict the correct temperature profile; although solution (2.14) provides a significantly better approximation com-

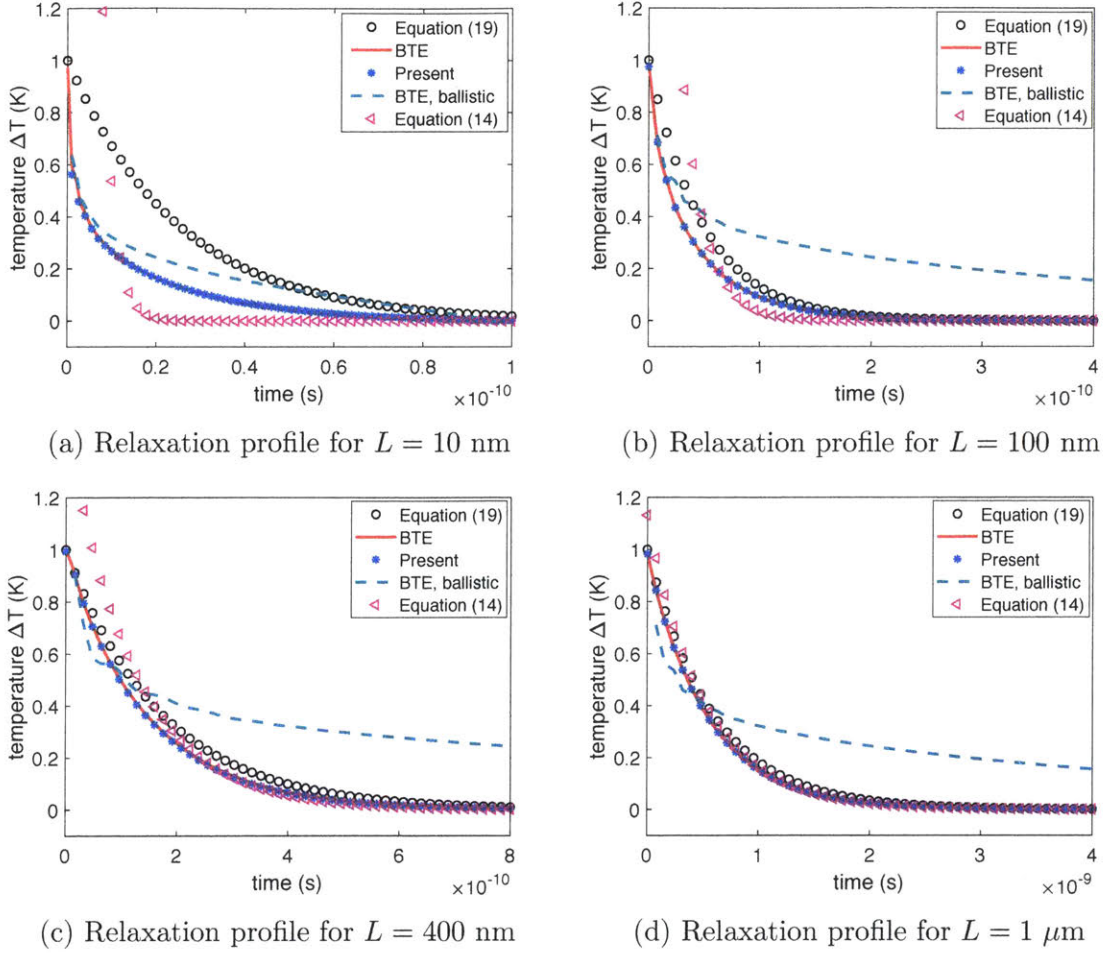


Figure 2-15: Comparison between the method proposed in the present work and various Fourier-based methods. Temperature relaxation profiles are shown for four grating wavelengths and compared to BTE solution for the Holland material model (denoted “BTE”). The prediction of the method proposed here, denoted as “present”, is given by solution of the Boltzmann equation based on the reconstructed relaxation time data of figure 2-4. Solutions based on equations (2.14) and (2.19) are denoted “Equation (2.14)” and “Equation (2.19)”, respectively.

pared to expression (2.19) at late times, the BTE solution is clearly not of exponential form at early and moderate times (in other words, although (2.14) appears to be close to the BTE solution, this is partly because both go to 0 at late times). At  $L = 400$  nm ( $\text{Kn} \approx 0.24$ ) the agreement between (2.14) and the BTE solution is good; equation (2.19) remains inaccurate. The comparison at  $L = 1 \mu\text{m}$  ( $\text{Kn} \approx 0.096$ ) shows good agreement between equation (2.14) and the BTE solution; equation (2.19) also becomes a reasonable approximation. Further comparison (not shown here) shows

that at  $L = 10 \mu\text{m}$  ( $\text{Kn} \approx 0.0096$ ), both Fourier-based solutions are able to reproduce the Boltzmann solution.

A comparison for the Holland model can be found in figure 2-15. The results are similar, but generally reveal worse performance by equation (2.14) in the critical  $\text{Kn} = 0.2 - 1$  range. Also, the ballistic behavior is observed at smaller wavelengths (approximately  $L = 1 \text{ nm}$  —not shown here).

In summary, although relation (2.14) shows that a regime featuring exponential relaxation is possible, this is only physically realizable (and measurable) for  $\text{Kn}^2 \ll 1$ . This is clearly more favorable than the typical requirement ( $\text{Kn} \ll 1$  for homogeneous materials,  $\text{Kn} \lll 1$  in the presence of boundaries [63]) for validity of Fourier’s law uncorrected; the improved range of validity is due to the corrections (2.15)–(2.17), which are available, in part, due to the simplicity of the TTG problem and geometry. Although extensions of Fourier approaches are sometimes possible (e.g. see [63] for the role of boundaries), these are not always guaranteed to exist or be tractable and their range of validity cannot be expected to extend to  $\text{Kn} \sim 1$ , except fortuitously.

With the above considered, for the TTG case, the effective thermal conductivity construction and associated solution (2.14) is only strictly theoretically justified in the limit  $\text{Kn}^2 \ll 1$ . In some cases this coincides with the range in which experiments operate [18], in which case reconstruction using a diffusive approximation may be acceptable provided:

- the correct asymptotic relation (i.e. equation (2.14)) is used
- some loss of accuracy outside the range over which experimental data is available is acceptable

We also point out that the validation in [13] featured wavelengths satisfying  $\text{Kn}^2 \ll 1$ . In general, however, the requirements  $\text{Kn}^2 \ll 1$  and  $t \gg \tau_\omega$  are very restrictive, especially when considering that typical pump-probe response time is on the order of a few nanoseconds [19]. In contrast, the method proposed here introduces no lengthscale or timescale restriction; moreover, if input data is available over a limited range of wavelengths, the quality of the reconstruction does not suffer significantly.

We close this chapter by noting that even if the (rather restrictive) requirements mentioned here for validity of the effective-heat-conductivity approach are satisfied, in general, there is no guarantee that the free path distribution is a reliable substitute for the relaxation time function. In fact, we will show in Chapter 5 that a given free path distribution is incapable of predicting a unique relaxation time function and, more importantly, a unique thermal response.

# Chapter 3

## Reconstruction in the presence of interface

In this chapter, in section 3.1, we propose an extended version of the optimization formulation discussed in Chapter 2, where the existence of the interface in the experiment is also included. In section 3.2, we discuss the implementation of the algorithm. In section 3.3, we validate the proposed methodology using synthetic experimental data on the 2D-dots geometry [19], where a Si-Al interface exists, discuss our results, and compare our method to previously used effective thermal conductivity-based approaches. The silicon material models used in this chapter have also appeared previously in [29, 39], and [28]. For the aluminum, we used the material model adapted from the dispersion relation in [64] with constant relaxation time of  $\tau_{\text{Al}} = 10$  ps as in [29, 39].

This chapter is based on Ref. [9], where the reconstruction in the presence of interface first was discussed.

## 3.1 Formulation

### 3.1.1 Governing equations for transport across interface

In the presence of a material interface, equation (2.1) requires matching conditions across the interface, usually supplied in the form of phonon transmissivities. More specifically, the frequency-dependent transmissivity from material 1 to material 2 in the presence of interface in a given geometry, denoted by  $T_{12,\omega}$ , is defined as the probability that a phonon with frequency  $\omega$  can transmit through the interface. Similarly, the reflectivity,  $R_{12,\omega} = 1 - T_{12,\omega}$ , is the probability that the phonon is reflected back into material 1 after impinging on the interface. In this work, we have assumed elastic and diffuse scattering (at the interface), that is, phonons preserve their mode as they travel across the interface while losing the memory of their initial direction (emerging direction is random). Under these assumptions, the transmissivities of two sides of the interface are related to each other through the principle of detailed balance [65],

$$T_{12,\omega}v_{\omega,1}C_{\omega,1} = T_{21,\omega}v_{\omega,2}C_{\omega,2} \quad (3.1)$$

where  $C_{\omega,1}$  and  $v_{\omega,1}$  are the frequency-dependent volumetric heat capacity and group velocity of material 1 and similarly  $C_{\omega,2}$  and  $v_{\omega,2}$  are the frequency-dependent volumetric heat capacity and group velocity of material 2. The transmissivities are usually related to the interface heat conductance  $G$  and properties of materials 1 and 2 via the model [29, 39, 65]

$$G = \frac{0.5}{2 \left( \int_{\omega} T_{12,\omega} C_{\omega,1} v_{\omega,1} d\omega \right)^{-1} - \left( \int_{\omega} C_{\omega,1} v_{\omega,1} d\omega \right)^{-1} - \left( \int_{\omega} C_{\omega,2} v_{\omega,2} d\omega \right)^{-1}}. \quad (3.2)$$

### 3.1.2 Inverse problem formulation in the presence of interface

Our goal here, similar to Chapter 2, is to obtain an accurate approximation to the function  $\tau_{\omega}$  from the experimental temperature measurements. The relaxation time function follows the model that was discussed in section 2.1.2, with the functional form

described in equation (2.7). The interface transmissivity as a function of frequency  $T_{12,\omega}^S(\omega)$  is also expressed using piecewise linear relations. This function is additionally constrained to vary between 0 and  $\min\{1, \frac{v_{\omega,2}C_{\omega,2}}{v_{\omega,1}C_{\omega,1}}\}$  since transmissivity represents a probability. Note that the upper bound is set by both the maximum permissible probability of  $T_{12,\omega}$  and  $T_{21,\omega}$ ; the latter is determined via (3.1). The specific functional form is given by

$$T_{12,\omega}^S = \max \left\{ \min \left\{ \sum_{j=0}^{\bar{M}^S-1} \left[ \frac{T_{12,\bar{\omega}_{j+1}}^S - T_{12,\bar{\omega}_j}^S}{\bar{\omega}_{j+1}^S - \bar{\omega}_j^S} (\omega - \bar{\omega}_j^S) + T_{12,\bar{\omega}_j}^S \right] \mathbb{1}_{\omega \in [\bar{X}_{2j}^S, \bar{X}_{2j+1}^S]} + \sum_{j=1}^{\bar{M}^S-1} [\bar{a}_j^S \omega^3 + \bar{b}_j^S \omega^2 + \bar{c}_j^S \omega + \bar{d}_j^S] \mathbb{1}_{\omega \in (\bar{X}_{2j-1}^S, \bar{X}_{2j}^S)}, \frac{v_{\omega,2}C_{\omega,2}}{v_{\omega,1}C_{\omega,1}}, 1 \right\}, 0 \right\}. \quad (3.3)$$

The role of the parameters  $\bar{M}^S$ ,  $\bar{\omega}_j^S$ ,  $\bar{X}_j^S$ ,  $\bar{a}_j^S$ ,  $\bar{b}_j^S$ ,  $\bar{c}_j^S$ , and  $\bar{d}_j^S$  is similar to  $M^S$ ,  $\omega_j^S$ ,  $X_j^S$ ,  $a_j^S$ ,  $b_j^S$ ,  $c_j^S$ , and  $d_j^S$  in equation (2.7), respectively; definitions can be found in Appendix E. We extend the vectorial notations used in Chapter 2 to transmissivity parameters, that is,  $\mathbf{T}_{12}^S = (T_{12,\bar{\omega}_0}^S, \dots, T_{12,\bar{\omega}_{\bar{M}^S}}^S)$ , and  $\bar{\omega}^S = (\bar{\omega}_1^S, \dots, \bar{\omega}_{\bar{M}^S-1}^S)$  to represent the unknown parameters. Similarly, the vector of all unknowns (equation (2.8) in Chapter 2) in the presence of transmissivities is

$$\mathbf{U} = (\boldsymbol{\tau}^{LA}, \boldsymbol{\tau}^{TA_1}, \boldsymbol{\tau}^{TA_2}, \boldsymbol{\omega}^{LA}, \boldsymbol{\omega}^{TA_1}, \boldsymbol{\omega}^{TA_2}, \mathbf{T}_{12}^{LA}, \mathbf{T}_{12}^{TA_1}, \mathbf{T}_{12}^{TA_2}, \bar{\omega}^{LA}, \bar{\omega}^{TA_1}, \bar{\omega}^{TA_2}), \quad (3.4)$$

where optical phonons were excluded since in this chapter we are only considering acoustic branches (see the discussion in section 2.2.3).

Here we note that formulation proposed in (3.3) does not use any of the previously proposed interface transmissivity models, such as the diffuse mismatch model (DMM) and the acoustic mismatch model (AMM) [33, 66], which are known to be inaccurate, in particular at higher temperatures [67]. Note that we have used the DMM model in section 3.3 for generation of synthetic experimental data (for validation purposes), but that in no way implies an assumption of such behavior during the reconstruction process.

Assuming, without loss of generality, that we are interested in reconstructing the

relaxation times of material 1, the new objective function (the modified version of (2.9)) that needs to be minimized is

$$\begin{aligned} \min_{\mathbf{U}} \mathcal{L} = & \\ & \min_{\mathbf{U}} \left[ \frac{\sum_{t,\mathbf{x},L} |T_m(t, \mathbf{x}; L) - T_{\text{BTE}}(t, \mathbf{x}; L, \mathbf{U})|}{N} + \alpha \left| 1 - \frac{1}{3\kappa_1} \int_{\omega} C_{\omega,1} \tau_{\omega,1}(\mathbf{U}) v_{\omega,1}^2 d\omega \right| \right. \\ & \left. + \beta \left| 1 - \frac{0.5G^{-1}}{2 \left( \int_{\omega} T_{12,\omega}(\mathbf{U}) C_{\omega,1} v_{\omega,1} d\omega \right)^{-1} - \left( \int_{\omega} C_{\omega,1} v_{\omega,1} d\omega \right)^{-1} - \left( \int_{\omega} C_{\omega,2} v_{\omega,2} d\omega \right)^{-1}} \right| \right], \end{aligned} \quad (3.5)$$

where  $T_m(t, \mathbf{x}; L)$ ,  $T_{\text{BTE}}$ ,  $N$ , and  $L$  have the same meaning as before (equation (2.9)).

The second and third terms in the definition of  $\mathcal{L}$  are regularizers whose purpose is to improve the quality of the optimization process. The second term uses the (presumed known) value of the heat conductivity of material 1,  $\kappa_1$ , to improve the quality of the reconstructed relaxation times, while the third term uses the (presumed known) value of the interface thermal conductance,  $G$ , to enhance the accuracy of the reconstruction. We have empirically determined that setting  $0.01 < \alpha, \beta < 1$  improves the reconstruction considerably. If the value of  $\kappa_1$  and/or  $G$  is unknown, the respective terms can be removed (by setting the corresponding coefficient to zero). In the present work we have assumed that  $G$  is unknown, therefore, the objective function used for reconstruction/validation purposes in the remainder of this chapter only features the first and the second terms ( $\beta = 0$ ). However, in section 3.2, we discuss a reconstruction framework that can be applied to both cases with known and unknown interface thermal conductance.

## 3.2 Reconstruction

Similar to the process discussed in Chapter 2, the reconstruction here is based on an optimization process utilizing the Nelder-Mead (NM) algorithm [51]. Reconstruction proceeds by comparing solutions of equation (2.1), obtained via adjoint MC simulations [32] using  $\mathcal{N}_{\text{BTE}}$  particles, with the counterpart  $N$  measurements of  $T_m$ . As

discussed before, phonon group velocities were assumed known, while  $\tau_\omega$  was described by the model given in equation (2.7) with  $M^S = 3$  (a piecewise linear function with three segments) and  $T_{12,\omega}$  by the model described by equation (3.3) with  $\bar{M}^S = 1$ . We have considered three branches for relaxation times (representing three acoustic branches), leading to  $3 \times 6 = 18$  unknowns and only one branch for the transmissivities, adding two unknowns, leading to a total of 20 unknowns. We have observed that increasing the number of branches and/or the value of  $\bar{M}^S$  does not affect the quality of the reconstructed relaxation times significantly, implying that the reconstruction is less sensitive to the values of  $T_{12,\omega}$  (see the discussion in section 3.3.3).

Previously, in Chapter 2, we have proposed a reconstruction algorithm [8] which featured four stages of optimization. Here, in the presence of an interface, we have found that an additional stage is helpful. This additional stage, that we refer to as stage zero, provides an initial estimate for the parameters of the interface transmissivity function,  $T_{12,\omega}$ , that is needed in stage one. If the value of  $G$  is known, this stage is not required.

### 3.2.1 Problems with known interface conductance

Since the role of stage zero is better understood in the context of the first stage of the optimization process, we first discuss stages one through four, suitable for problems with known  $G$ ; stage zero is discussed in the following section.

In the first stage, we assume that all relaxation times (three branches) are described by one line (one branch with  $M^S = 1$ ), leading to two unknowns, namely  $\tau_{\omega_0}$  and  $\tau_{\omega_3}$ . We also use one line to describe the unknown transmissivities, contributing two additional unknowns, namely  $T_{12,\bar{\omega}_0}$  and  $T_{12,\bar{\omega}_1}$ . For  $M^S = 1$  and  $\bar{M}^S = 1$ , equations (2.7) and (3.3) reduce to

$$\log(\tau_\omega) = p \log(\omega) + k, \quad (3.6)$$

and

$$T_{12,\omega} = \hat{p}\omega + \hat{k}, \quad (3.7)$$

respectively, where the superscript  $S$  is omitted since in this stage all branches obey the same model. We also note that the parameters in (2.7) are related to  $p$  and  $k$  via

$$\tau_{\omega_0} = \omega_0^p 10^k, \quad \tau_{\omega_3} = \omega_3^p 10^k, \quad (3.8)$$

while the parameters in (3.3) are related to  $\hat{p}$  and  $\hat{k}$  via

$$T_{12, \bar{\omega}_0} = \hat{p} \bar{\omega}_0 + \hat{k}, \quad T_{12, \bar{\omega}_1} = \hat{p} \bar{\omega}_1 + \hat{k}. \quad (3.9)$$

In order for the values of  $p$  and  $k$  to satisfy the given value of  $\kappa$  (heat conductivity of the material under study;  $\kappa_1$  in equation (2.9)), we must have

$$k = \log \left( \frac{3\kappa}{\int_{\omega} C_{\omega} \omega^p v_{\omega}^2 d\omega} \right), \quad (3.10)$$

where  $C_{\omega} = C_{\omega,1}$  and  $v_{\omega} = v_{\omega,1}$ . Similarly, with the value of  $G$  known, the following relation should hold between  $\hat{p}$  and  $\hat{k}$

$$\hat{k} = \frac{2}{1 + \frac{\int_{\omega} C_{\omega,1} v_{\omega,1} d\omega}{2G} + \frac{\int_{\omega} C_{\omega,1} v_{\omega,1} d\omega}{\int_{\omega} C_{\omega,2} v_{\omega,2} d\omega}} - \hat{p} \frac{\int_{\omega} C_{\omega,1} v_{\omega,1} \omega d\omega}{\int_{\omega} C_{\omega,1} v_{\omega,1} d\omega}. \quad (3.11)$$

Equations (3.10)–(3.11) provide relationships between two first-stage unknown variables and known material properties. While the first stage features four unknowns ( $k$ ,  $\hat{k}$ ,  $p$ ,  $\hat{p}$ ), due to these relations, only two parameters ( $p$  and  $\hat{p}$ ) need to be guessed as part of the initialization. Once the parameters  $p$  and  $\hat{p}$  are specified,  $k$  and  $\hat{k}$  can be determined via equations (3.10) and (3.11), from which the initial condition for  $\tau_{\omega}$  and  $T_{12, \omega}$  can be calculated using equations (3.8) and (3.9). Note that this treatment does not change the number of unknown parameters in stage one; instead, it increases the efficiency of the optimization algorithm by dismissing initial conditions that are inconsistent with the material/interface properties.

In the second stage, the  $LA$  and  $TA$  modes of the relaxation time function are still assumed to be the same but the intended number of segments is used, increasing the number of unknowns for the relaxation times to  $2M^S$  (six in the present case).

The number of unknowns for the transmissivity function stays at two, leading to a total of 8 unknowns. The initial condition for this stage is taken to be the same as the optimized value of the previous stage (or a slightly perturbed version).

In the third stage, we repeat the optimization process, now for  $2(M^{LA} + M^{TA})$  unknowns (the two  $TA$  branches are assumed to be the same,  $\tau_{\omega}^{TA_1} = \tau_{\omega}^{TA_2}$ ), starting from the optimized parameters of the second stage. The number of unknowns for the transmissivity function does not change at this stage. Therefore, the total number of unknowns is  $12 + 2 = 14$ .

Finally, we perform the optimization for all  $2(M^{LA} + M^{TA_1} + M^{TA_2})$  unknowns of the relaxation times and the two unknowns of the transmissivity function (total of 20 unknowns), starting from the optimized parameters of the previous stage. The optimized values at this stage are the final values parameterizing the relaxation time and transmissivity functions.

### 3.2.2 Problems with unknown interface conductance

As explained in the previous section, if  $G$  is known, given a guess for  $\hat{p}$ ,  $\hat{k}$  can be calculated using equation (3.11). If, however,  $G$  is unknown, (3.11) cannot be used. Therefore, an additional stage (stage zero) is added to the optimization process to provide an initial value for  $\hat{k}$  that is consistent with the initial guess for  $\hat{p}$  to be used in stage one.

To obtain a value for  $\hat{k}$  consistent with the value of  $\hat{p}$  to be used in stage one we perform an optimization assuming constant relaxation times ( $\tau(\omega) = \tau$ ) and a fixed value of  $\hat{p}$ . Since the single constant (gray) relaxation time is related to the (assumed known) thermal conductivity via

$$\tau = \frac{3\kappa}{\int_{\omega} C_{\omega} v_{\omega}^2 d\omega}, \quad (3.12)$$

$\hat{k}$  is the only unknown function at this stage and can be solved for by optimization. Using this optimized value and the guess for  $\hat{p}$ , initial conditions for stage one for  $T_{12, \bar{\omega}_0}$  and  $T_{12, \bar{\omega}_1}$  can be obtained from (3.9).

The initial guesses for stage one for  $\tau_{\omega_0}$  and  $\tau_{\omega_3}$  remain the same as in the case of known  $G$ , namely,

$$\tau_{\omega_0} = \frac{3\kappa\omega_0^p}{\int_{\omega} C_{\omega}\omega^p v_{\omega}^2 d\omega}, \quad \tau_{\omega_3} = \frac{3\kappa\omega_3^p}{\int_{\omega} C_{\omega}\omega^p v_{\omega}^2 d\omega} \quad (3.13)$$

(see equations (3.8) and (3.10)).

### 3.2.3 Initialization protocol

To reduce the probability of the reconstruction being trapped in a local minimum, in our approach, we repeated the first stage of the optimization for four different values of  $p$  and four different values of  $\hat{p}$ , leading to a total of  $4 \times 4 = 16$  distinct initial conditions. Consequently, since  $\hat{k}$  for a given  $\hat{p}$  is determined via the zeroth stage, the zeroth stage was also repeated four times. The second stage was also repeated for five different initial conditions which were the five lowest values of  $\mathcal{L}$  obtained from optimizations in stage one<sup>1</sup>. Finally, third and fourth stages were performed for only one initial condition corresponding to the lowest value of  $\mathcal{L}$  in the second and third stages of the optimization, respectively.

To reduce cost, MC simulations during the zeroth, first and second stages of the optimization process used  $\mathcal{N}_{\text{BTE}} = 10^4$  particles for calculation of  $T_{\text{BTE}}$ . During the third and fourth stages of the process, since we were looking for more accurate solutions, the number of particles was increased to  $\mathcal{N}_{\text{BTE}} = 10^6$ . As it was discussed in Chapter 2, since the computational time for each adjoint MC simulation is proportional to  $\mathcal{N}_{\text{BTE}}$  [32], given our choices for  $\mathcal{N}_{\text{BTE}}$ , the cost of the first three stages of the optimization is negligible compared to the cost of the last two stages, therefore, repeating them a number of times starting from different initial conditions does not increase the cost of the reconstruction process significantly.

---

<sup>1</sup>In some cases where multiple simulations of stage one had similar values for  $\mathcal{L}$ , we repeated simulations of stage two for all such initial conditions, leading to more than five simulations in the second stage.

### 3.3 Validation

We demonstrate the use and validate the effectiveness and accuracy of the proposed methodology using synthetic data obtained from MC simulations of equation (2.1) for the 2D-dots problem [19], using the adjoint deviational formulation described in [32]. In other words, we generate “synthetic” experimental data  $T_m(t, \mathbf{x}; L)$  by solving equation (2.1) for a particular material model and then use the proposed formulation to reconstruct the material properties (relaxation times and free path distribution) and compare with the input data. Synthetic data are preferable (to experimental data) because they allow us to validate the accuracy of the algorithm directly with no need to account for possible experimental error, as well as modeling error resulting from neglecting various effects (e.g. electronic transport) present in experiments. A sketch of the 2D-dots geometry can be found in figure 3-1.

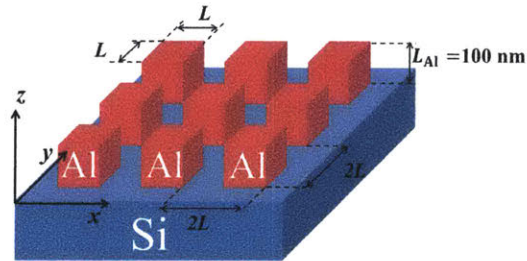


Figure 3-1: 2D-dots geometry, comprising a periodic array of Al “dots” on a Si substrate. The structure is assumed to be sufficiently large that it can be approximated as infinite in the  $x$  and  $y$  directions; moreover, the Si substrate thickness is sufficiently large to be approximated as semi-infinite. The dot height is constant at  $L_{Al} = 100$  nm, while the dot base is square with edge length  $L$ . The ratio between  $L$  and the periodicity of the structure is constant at 0.5. The experimental measurement,  $T_m(t, \mathbf{x}; L)$ , corresponds to the surface temperature of Al after the initial heating event at  $t = 0$ .

#### 3.3.1 Generation of synthetic experimental data

The material under study here is taken to be silicon. We have considered the same set of silicon material properties that we used in Chapter 2 and [8], namely, *ab initio* model (thermal conductivity  $\kappa = 139.7 \text{ Wm}^{-1}\text{K}^{-1}$ ) and Holland model (thermal conductivity  $\kappa = 143.8 \text{ Wm}^{-1}\text{K}^{-1}$ ). Also for Al, we used the material model adapted

from the dispersion relation in [64] with constant relaxation time of  $\tau_{\text{Al}} = 10$  ps as in [29, 39].

Synthetic data was generated using two different interface models. The first model is the DMM which is widely used in transport theory [33]. According to this model, the transmissivity from material 1 to 2 is given by

$$T_{12,\omega} = \frac{C_{\omega,2}v_{\omega,2}}{C_{\omega,1}v_{\omega,1} + C_{\omega,2}v_{\omega,2}}. \quad (3.14)$$

The second model is based on experimental measurements shown in figure 12 of [67]; it will be referred to as the “experimental” model in the present work.

The generated synthetic temperature relaxation profiles are in the form of  $T_{\text{m}}(0 \leq t \leq 5 \text{ ns}, \mathbf{x}_{\text{s}}; L)$ , implying measurement at the surface of Al,  $\mathbf{x}_{\text{s}} = (x, y, 100 \text{ nm})$  (based on the coordinates in figure 3-1) for 5 ns, which is a typical measurement time in pump-probe experiment of the 2D-dots geometry [19]. Ten different side lengths were simulated; namely,  $L = 10 \text{ nm}, 20 \text{ nm}, 40 \text{ nm}, 100 \text{ nm}, 500 \text{ nm}, 750 \text{ nm}, 1 \mu\text{m}, 2.5 \mu\text{m}, 5 \mu\text{m},$  and  $50 \mu\text{m}$ . Each simulation is sampled at 100 discrete time instances (during the relaxation). As a result, 1000 total  $T_{\text{m}}$  measurements were available for reconstruction ( $N = 1000$ ). The data were generated using both essentially noise-free MC simulations via  $\mathcal{N}_{\text{m}} = 10^8$  particles, and noisy MC simulations with  $\mathcal{N}_{\text{m}} = 10^3$  particles. The latter were used to assess the method performance in the presence of noisy experimental measurements (see figure 2-6 for a comparison of the noisy and noise-free temperature profiles).

### 3.3.2 Results

In this section, we present comparisons between the reconstructed relaxation times  $\tau_{\omega} = \tau(\omega)$  (and associated cumulative distribution function (CDF) of free paths) and the corresponding properties used as input for generating the synthetic experimental data. The definition of CDF can be found in Chapter 2; the corresponding probability density function (of free paths) is given by  $\mathbf{f} = \frac{dF}{d\Lambda}$ .

Our comparison figures also display the reconstructed interface transmissivities, al-

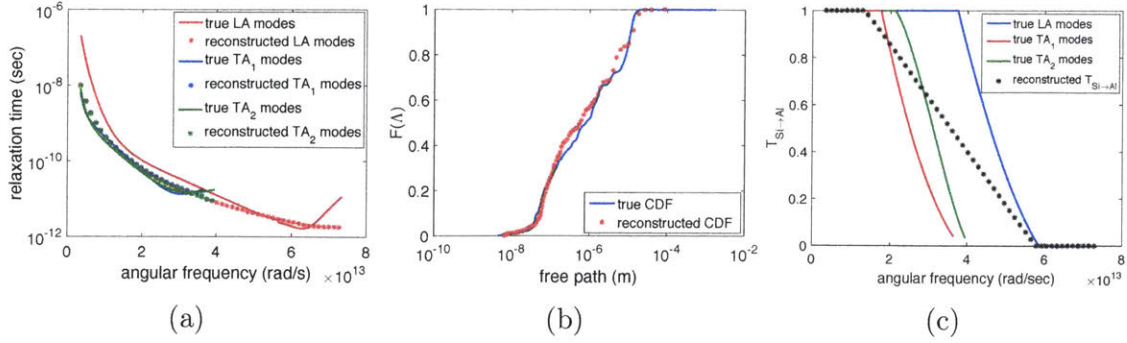


Figure 3-2: Reconstructed material properties with *ab initio* relaxation times, experimental transmissivities, and noise-free synthetic relaxation profiles.

though, as stated previously, the goal of the algorithm is not to specifically determine the mode dependent transmissivities; the latter are a by-product of the relaxation time reconstruction. Similar to the figures presented in Chapter 2, in these figures, the input material properties (which synthetic relaxation profiles are generated from) are labeled as “true”, while the reconstructed properties (obtained through the optimization process) are labeled as “reconstructed”.

**Ab initio model** In this section, we present the reconstructed silicon material properties for the *ab initio* material model. This model has two *TA* branches, therefore, there is a total of 20 unknowns.

Figures 3-2 and 3-3 show a comparison between the true material parameters and the reconstructed ones for the *ab initio* silicon material properties using the experimental interface transmissivities, in the absence and presence of noise, respectively.

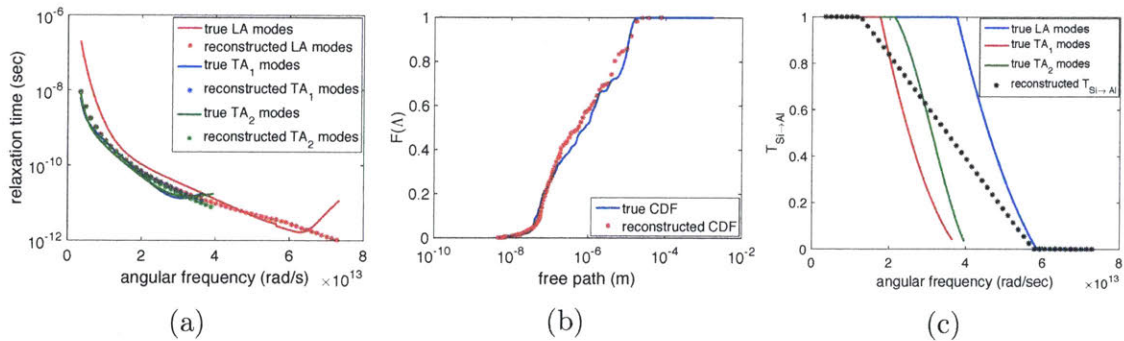


Figure 3-3: Reconstructed material properties with *ab initio* relaxation times, experimental transmissivities, and noisy synthetic relaxation profiles.

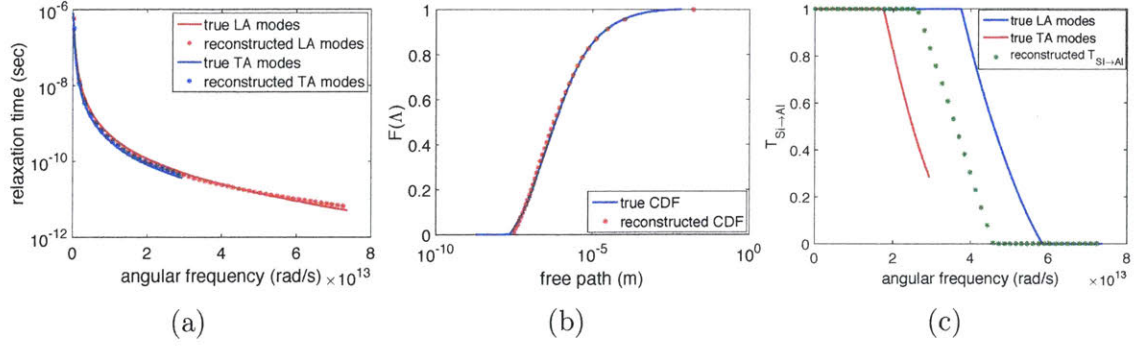


Figure 3-4: Reconstructed material properties with Holland relaxation times, experimental transmissivities, and noise-free synthetic relaxation profiles.

We observe that the reconstructed relaxation times are close to the true data. We also note that the discrepancy is more noticeable for low frequencies, primarily due to the low density of states of these frequency ranges; in particular, as stated previously, the density of states of the *LA* modes for  $\omega \leq 8 \times 10^{12}$  rad/s is zero. These figures show that the error in the reconstructed transmissivities is more significant. However, the final value of the objective function is small, indicating that accurate reconstruction of relaxation time distribution that can reproduce the input temperature profiles (comparisons between input temperature profiles and their counterparts predicted by the reconstructed properties can be found in figure 3-10) are possible even if the transmissivities are not accurately reconstructed.

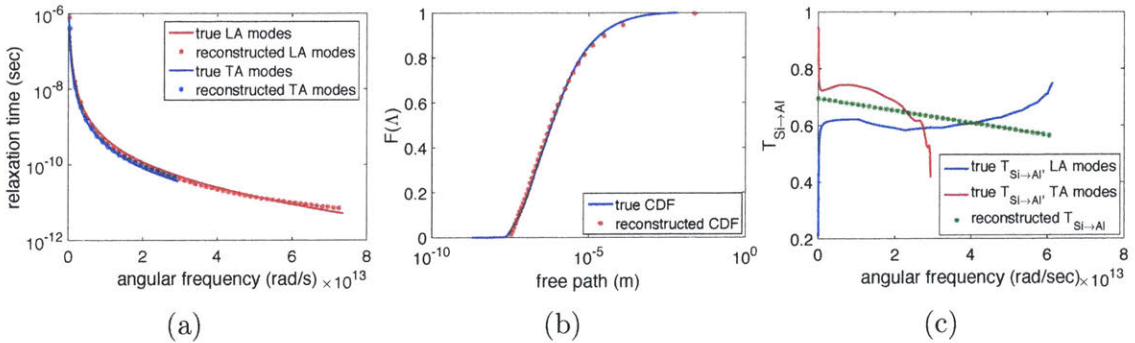


Figure 3-5: Reconstructed material properties with Holland relaxation times, DMM transmissivities, and noise-free synthetic relaxation profiles.

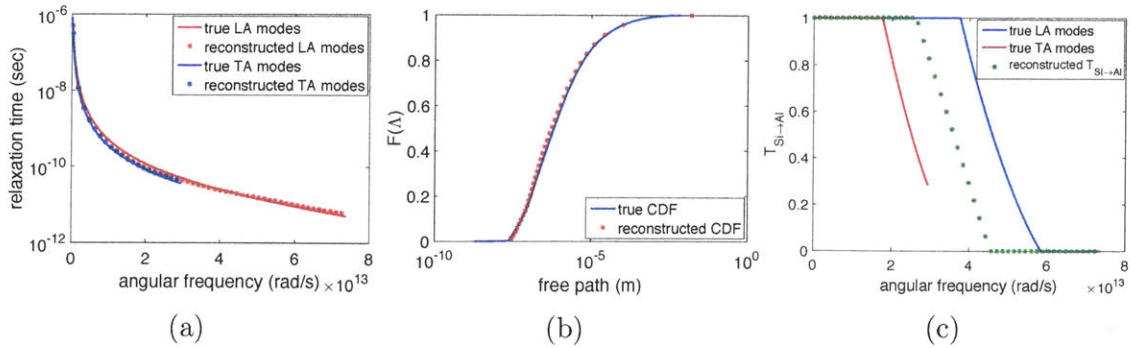


Figure 3-6: Reconstructed material properties with Holland relaxation times, experimental transmissivities, and noisy synthetic relaxation profiles.

**Holland model** Here, we present results for the Holland material model. This model assumes that the two  $TA$  branches are the same and as a result, the optimization process consists of three stages (plus the stage zero) with a total of  $4 \times 3 + 2 = 14$  unknowns.

Figures 3-4 and 3-5 show a comparison between the true material parameters and the reconstructed ones for the Holland set of data using the experimental and DMM interface transmissivities, respectively, in the absence of noise. We observe that the algorithm is able to capture true relaxation times with reasonable accuracy. Our conclusions are similar to the case of *ab initio* data, namely, even though the transmissivities are not reproduced accurately, the relaxation times, which are the quantities of interest, are accurately reconstructed. We can also observe that the same conclusion can be made in the case of noisy data, figures 3-6 and 3-7.

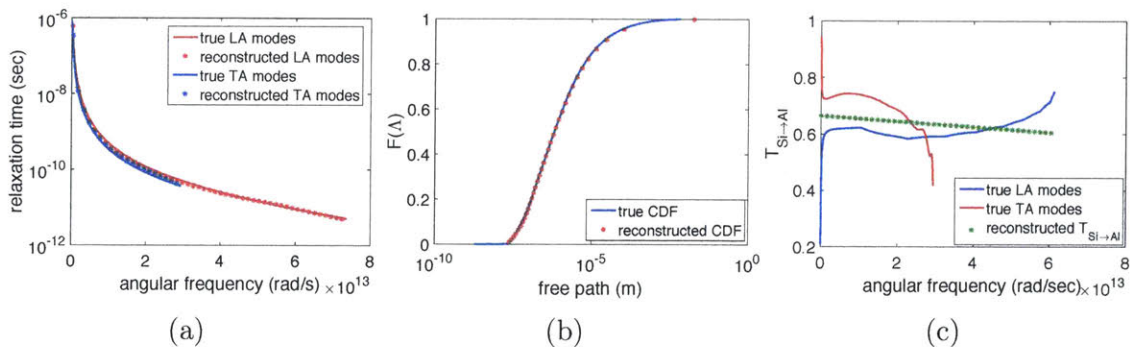


Figure 3-7: Reconstructed material properties with Holland relaxation times, DMM transmissivities, and noisy synthetic relaxation profiles.

### 3.3.3 Effect of interface treatment

In the previous sections we have observed that one line ( $\bar{M}^S = 1$ ) results in a sufficiently adequate representation of the transmissivity (for all branches) *for the relaxation times to be reconstructed accurately*. Given the accurate reconstruction of the relaxation times and temperature fields (see figures 3-10a and 3-10b below), we would expect the interface properties to be captured correctly at least in an “average” sense. Indeed, in the above comparison figures (3-2–3-7) we observe that although the reconstructed transmissivity profiles are not very accurate in a spectral sense, they do capture the interface transmissivity in an average sense. To make this observation more quantitative, we have calculated the interface thermal conductance  $G$  associated with each of the reconstructed transmissivities in section 3.3.2. The resulting values, calculated using equation (3.2), are provided in table 3.1, which shows that the interface thermal conductances are, generally speaking, close to the thermal conductance associated with the true data from which the synthetic temperature relaxation profiles are generated. In other words, these results suggest that reconstruction of the relaxation times is only sensitive to the aggregate effect of the interface, as captured, for example, by a simple linear (as function of frequency) model.

Silicon model/ interface model/ data type	Holland expt. noise-free	Holland DMM noise-free	Holland expt. noisy	Holland DMM noisy	Ab initio expt. noise-free	Ab initio expt. noisy
$G$ (MW/m <sup>2</sup> K)	260	367	260	367	567	567
Reconstructed $G$ (MW/m <sup>2</sup> K)	265	353	273	364	630	658

Table 3.1: Calculated interface heat conductance based on the true (first row) and reconstructed (second row) interface transmissivities; “expt.” denotes the experimental interface model adapted from [67].

To verify this assertion, we have performed the optimization using a more complex parameterization in equation (3.3) where different branches are represented by different distinct linear functions, for all different cases of section 3.3.2. An example

of such reconstruction is provided in figure 3-8 for the Holland material model, experimental transmissivity, and noise-free synthetic data. We observe that the quality of the reconstruction has not improved compared to figure 3-4. Accordingly, we have not noticed any significant improvement in the final value of the objective function.

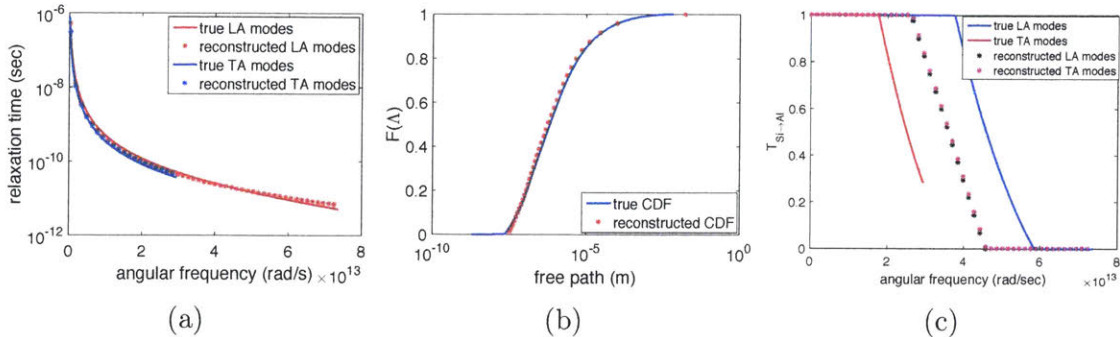


Figure 3-8: Reconstructed material properties with Holland relaxation times, experimental transmissivities, and noise-free synthetic relaxation profiles with separate linear models for frequency-dependent transmissivities of *LA* and *TA* branches.

As a further consistency check, we have repeated one of the reconstruction tests of section 3.3.2 assuming  $T_{21,\omega}$  (the transmissivity from Al to Si) to be the unknown (and hence constrained to be linear in angular frequency) function. The result for the experimental transmissivity and noise-free synthetic data is provided in figure 3-9. As expected, the reconstructed  $T_{12,\omega}$  transmissivities (obtained by applying principle of detailed balance to reconstructed  $T_{21,\omega}$ ) for the different branches are not the same as before and they are now distinct for different branches. However, comparison with figure 3-4 suggests that this result serves as the best, perhaps, illustration of our previous conclusion, namely that the reconstruction is fairly insensitive to the complexity of the parameterization used for the interface (provided it is reasonable); despite the clearly different results for  $T_{12,\omega}$ , the maximum discrepancy between the two reconstruction results (for the relaxation times) is only 0.7%, implying that they are essentially identical. The value of interface conductance associated with this reconstruction is  $G = 273 \text{ MW/m}^2\text{K}$ , which is very close to the heat conductance of the reconstruction of figure 3-4 ( $G = 265 \text{ MW/m}^2\text{K}$  from table 3.1).

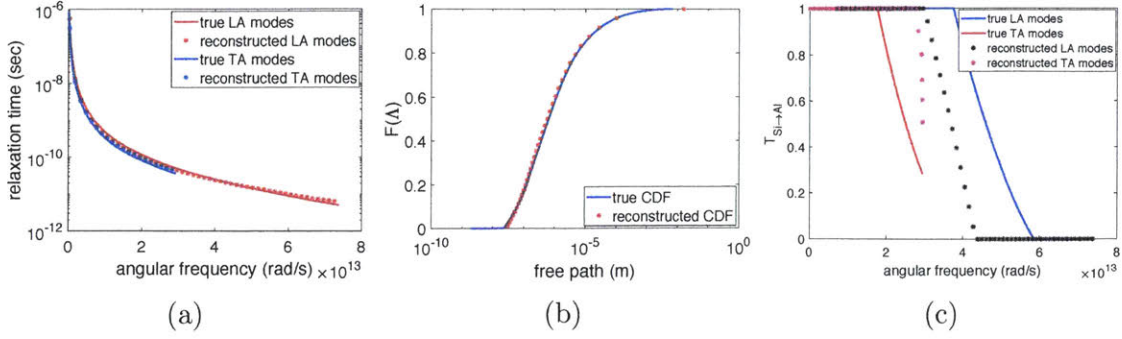


Figure 3-9: Reconstructed material properties with Holland relaxation times, experimental transmissivities, and noise-free synthetic relaxation profiles with  $T_{21,\omega}$  (the transmissivity from Al to Si) being unknown.

Figure 3-10 compares the synthetic input temperature profiles with relaxation profiles generated from reconstructed properties for some of the cases considered in this chapter. All plots show negligible differences between the input and reconstructed temperature profiles; the same conclusion is reached by observing the very small final value of  $\mathcal{L}$ . The trend for other reconstruction results (not shown here) is the same. This figure also confirms our earlier claim that the free time reconstruction can proceed without precise knowledge of the transmissivity profiles, making the present reconstructions (using simple models for the transmissivity) feasible.

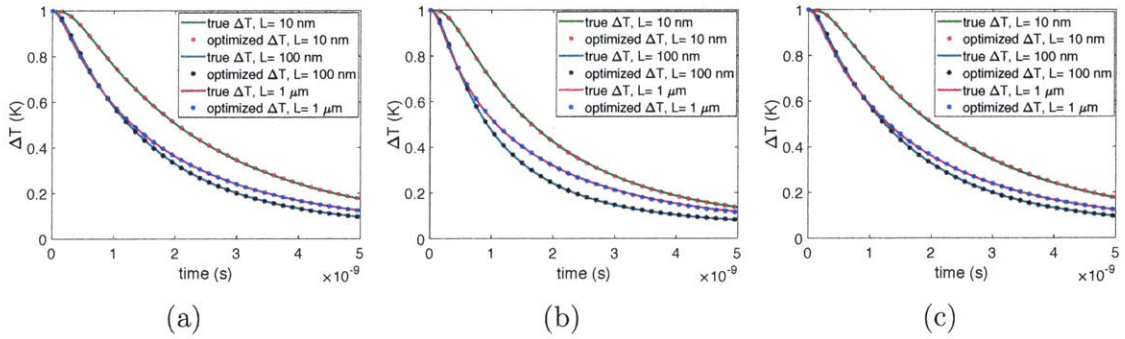


Figure 3-10: Comparison between the synthetic temperature profiles and the ones generated from the reconstructed properties of (a)- figure 3-4, (b)- figure 3-2, and (c)- figure 3-9.

### 3.3.4 Why is interface transmissivity reconstruction not as accurate as relaxation time reconstruction?

So far, we have empirically shown that accurate reconstruction of the relaxation times does not require reconstruction of interface transmissivities to the same accuracy level; specifically, our results suggest that treating the transmissivities using a simple linear model (as a function of frequency) for all branches is sufficient. At the same time, increasing the model complexity does not improve the quality of the interface property reconstruction, suggesting that it is, perhaps, not possible to obtain accurate transmissivity reconstructions from the TDTR setup we have considered here.

In order to gain some further insight we have performed reconstructions for different dot properties and heights. Figure 3-11 shows the reconstruction result which uses the Holland model for Si, experimental transmissivities, noise-free data, and  $\tau'_{Al} = 100\tau_{Al} = 1$  ns. This leads to an average Kn number inside the Al of 17 (based on the dot height), with a range of 17–170 (the characteristic length scale is taken to be the smallest of the dot height,  $L_{Al}$ , and  $L$ ). We observe that, similar to all reconstructions of sections 3.3.2 and 3.3.3, even though the transmissivities are only approximately reconstructed, the relaxation times are reconstructed accurately. We have also performed reconstructions for other Al relaxation times ( $\tau_{Al} = 100$  ps), other Si properties (*ab initio* data), and other interface properties (DMM) as well as different dot heights ( $L_{Al} = 10$  nm, 25 nm, and 50 nm); the conclusion is essentially the

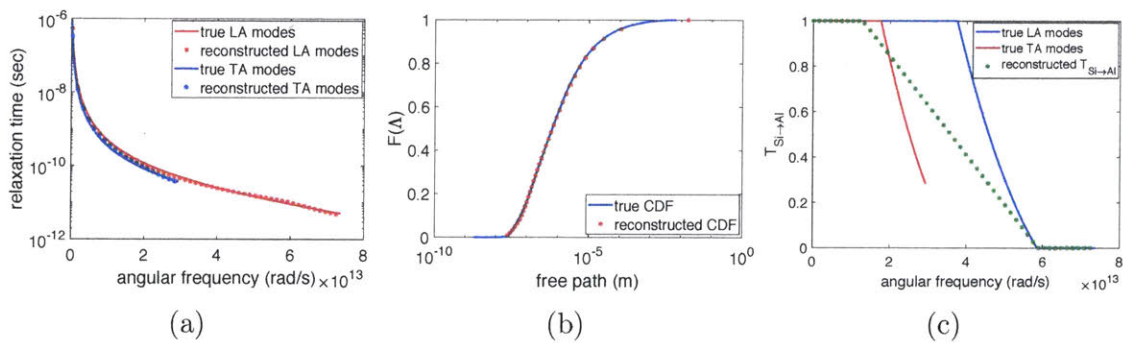


Figure 3-11: Reconstructed material properties with Holland relaxation times, experimental transmissivities, and noise-free temperature profiles with  $\tau'_{Al} = 100\tau_{Al} = 1$  ns.

same in all cases.

An important observation stemming from these numerical experiments is that the reconstructed transmissivity profile in figure 3-11 is different from the one shown in figure 3-4. At the same time, as observed before in table 3.1 for other reconstructions,  $G$  is approximately correctly reconstructed ( $G = 249 \text{ MW/m}^2\text{K}$ ). Although not surprising given our previous findings and discussion, the different transmissivity profile observed here is attributed to the fact that the transport regime (aluminum Knudsen number based on dot height) in the aluminum is different, altering the relative importance of different parts of the frequency spectrum (see [68] for a discussion). The correctly reconstructed value of  $G$ , on the other hand, suggests that temperature relaxation data at a fixed aluminum dot height, provides only sufficient information for a reconstruction of some “aggregate” effect of the interface. This may be attributed to the fact that the dot height has a more direct effect on the phonon population crossing the interface than length scale  $L$ .

In summary, what separates relaxation times from interface transmissivities in the present context (figure 3-1; constant dot height) is that TDTR experiments sample a variety of transport regimes in the substrate material (by varying the characteristic values of length scale  $L$ ), while only sampling one regime as far as the interface is concerned. As a result, relaxation times are accurately reconstructed, while interface properties are only approximately reconstructed (only reconstructed in an aggregate sense). The decoupling of these two unknowns, possibly due to the fact that they correspond to two distinct parts of the system (bulk vs boundary), has a profound effect on the feasibility of the reconstruction of the relaxation times. Implications of this observation for the reconstruction of interface properties are discussed below.

**Reconstruction of interface transmissivities** Motivated by the results such as transmissivity reconstruction of figure 3-11 versus 3-4, in which changing Kn number in Al (based on dot height) has led to different transmissivity functions, we have also performed a reconstruction in which other than the dot bases  $L$ , we also vary the dot heights  $L_{\text{Al}}$ , expecting to be able to have a more accurate reconstruction

of interface transmissivities. Here, we have generated synthetic temperature profiles for four different dot heights,  $L_{A1} = 10$  nm, 25 nm, 50 nm, and 100 nm, each with eight different side lengths (dot base); namely,  $L = 10$  nm, 20 nm, 40 nm, 100 nm, 500 nm, 1  $\mu\text{m}$ , 5  $\mu\text{m}$ , and 50  $\mu\text{m}$ , leading to  $4 \times 8 = 32$  total experiments. Each simulation was also sampled at 100 discrete time instances as before; this leads to  $32 \times 100 = 3200$  total  $T_m$  measurements ( $N = 3200$ ). The data were generated using noise-free MC simulations ( $\mathcal{N}_m = 10^8$ ) with Holland model for the relaxation times and the experimental transmissivity function. The model of the transmissivity function in the reconstruction process was also assumed to be linear as before, but different for  $LA$  and  $TA$  branches (similar to the model used in figure 3-8). The results are provided in figure 3-12.

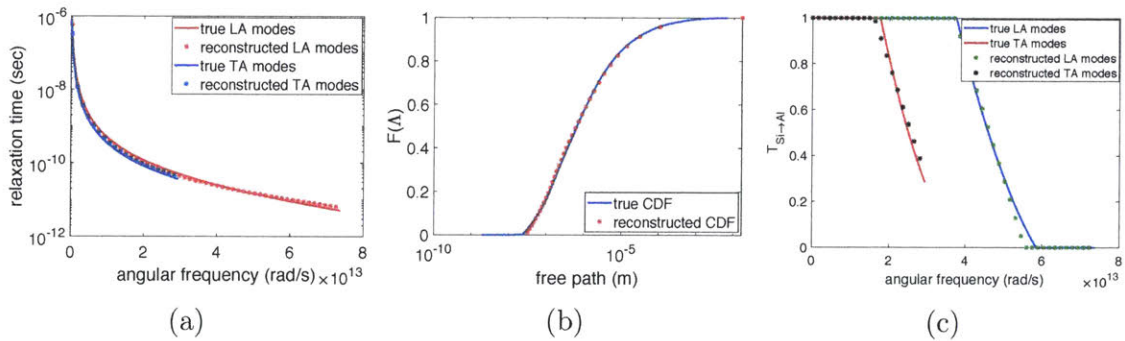


Figure 3-12: Reconstructed material properties with Holland relaxation times, experimental transmissivities, and noise-free temperature profiles with variable dot heights,  $L_{A1}$ .

An important observation in figure 3-12 is the accurate reconstruction of both the relaxation time function and the interface transmissivities. In particular, compared to figure 3-8, where the material model, the relaxation time function, and the transmissivity function, are all the same as the ones used in the reconstruction of figure 3-12, we observe that the quality of the reconstructed interface transmissivities has significantly improved. In fact, the reconstructed transmissivities for both  $LA$  and  $TA$  branches in figure 3-12, unlike figure 3-8, have been able to recover the true transmissivity functions accurately, implying that simultaneous reconstruction of both relaxation time function and interface transmissivities, without any knowledge

of the interface (either frequency-dependent transmissivity function or the interface thermal conductance), is possible, provided that both the dot height and base in the 2D-dots experimental setup are variable length scales.

### 3.3.5 Comparison to the effective thermal conductivity approach

In this section, we compare our approach with the prevalent reconstruction approach, namely the method based on the effective thermal conductivity.

The effective heat conductivity approach aims at reconstructing the phonon free path distribution directly from the measured temperature relaxation profiles, assuming that in the non-diffusive regime, heat transport can still be represented using the Fourier heat conduction equation with a suppressed heat conductivity,  $\kappa_{\text{eff}} \leq \kappa$  [13]. The effective heat conductivity approach is based on the *approximation*

$$\frac{\kappa_i}{\kappa} = \int_0^\infty S(\chi_i) f(\Lambda_\omega) d\Lambda_\omega = \int_0^\infty -\frac{dS(\chi_i)}{d\chi_i} \frac{d\chi_i}{d\Lambda_\omega} F(\Lambda_\omega) d\Lambda_\omega, \quad (3.15)$$

where  $\kappa_i$  is the effective heat conductivity associated with  $L_i$ , obtained by fitting the response  $T_m(t, \mathbf{x}; L_i)$  to the solution of Fourier heat conduction equation with  $\kappa_i$  treated as the unknown in the fitting process. In the above equation,  $\chi_i$  is a dimensionless quantity relating length scale to free paths, here taken to be  $\chi_i = \Lambda_\omega/L_i$ ,  $S(\chi_i)$  is the suppression function, and  $f(\Lambda_\omega)$  and  $F(\Lambda_\omega)$  are defined at the beginning of section 3.3.2.

While the approximate suppression function  $S(\chi_i)$  can be obtained analytically under a set of rather restrictive assumptions [8] for a few simple geometries such as 1D TTG [13], for most geometries, including 2D-dots, no analytical expression is available. Putting aside the fact that such a function may not exist, in such cases, it has been proposed [28] that it can be approximated by the suppressed effective thermal conductivity of the gray model in the same geometry, namely  $S(\chi_i) = \kappa_g(\chi_i)/\kappa$ , where the subscript  $g$  denotes gray model and  $\kappa_g(\chi_i)$  denotes the effective thermal conductivity measured by fitting the relaxation profile to the heat conduction equation

solution in the said geometry. Provided with measurements of length scale dependent effective heat conductivities,  $\kappa_i$ ,  $F(\Lambda_\omega)$  can be obtained by solving the inverse problem in equation (3.15) using a convex optimization framework [13].

In order to compare with our results, we performed the above procedure for the Holland model of silicon with both the experimental and DMM transmissivity functions and noise-free synthetic temperature profiles. The suppression function used for the reconstruction along with its derivative based on the experimental transmissivity are plotted in figure 3-13a. The suppression function was calculated by fitting a polynomial to ten different values of  $\kappa_g(\chi_i)/\kappa$ , obtained from gray simulations with  $L = 100$  nm by varying the gray mean free path. The suppression function with DMM transmissivities is essentially the same. Figure 3-13b shows  $\kappa_{\text{eff}}(L)$  ( $\kappa_i$  in equation (3.15)) normalized by  $\kappa$ , as obtained by MC simulations of ten different domain length scales ( $L$ ) based on both experimental and DMM transmissivities. Finally, figure 3-13c plots the reconstructed free path distribution, obtained using the convex optimization problem formulated in [13] with the same values for the number of integration points and parameter  $\eta$  (see [13] for more details), for both interface models. Our results do not change significantly if we use more than ten data points.

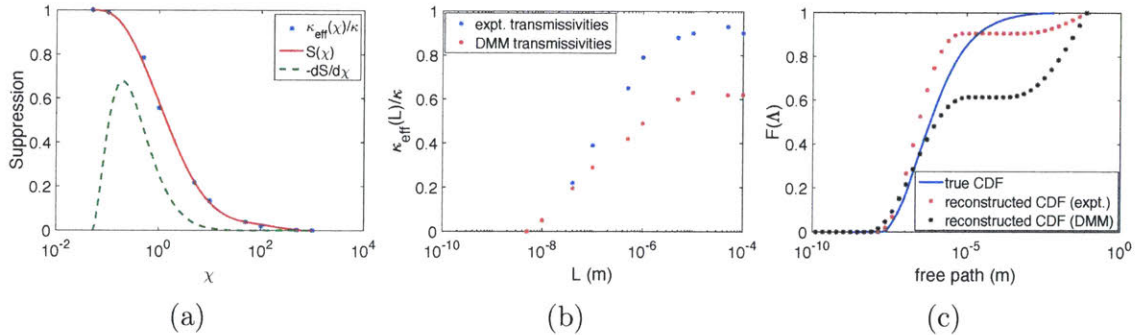


Figure 3-13: Reconstructed free path distribution based on effective thermal conductivity approach (c); “expt.” denotes the experimental interface model adapted from [67]. Length dependent cumulative effective heat conductivity (b). The suppression function based on experimental transmissivity interface model (a).

Three different types of discrepancies can be detected in figure 3-13c. The first discrepancy is the mismatch with the true CDF in the  $\Lambda \lesssim 5 \mu\text{m}$  region for both models which can be attributed to the gray approximation used for the calculation of

the suppression function; a similar trend has been observed previously in [28]. The second type of discrepancy is the mismatch with the true CDF, and in particular the plateau in  $F$ , in the range  $5 \mu\text{m} \lesssim \Lambda \lesssim 1 \text{ mm}$  in both models. Although constraining the CDF to reach 1 at large free paths (a property of the cumulative distribution function) has forced the CDF to eventually do so around  $\Lambda = 5 \text{ cm}$ , saturation of  $\kappa_{\text{eff}}(L)/\kappa$  for  $L \gtrsim 5 \mu\text{m}$  (see figure 3-13b) has caused significant discrepancy between the reconstructed and true free path distribution in the region  $5 \mu\text{m} \lesssim \Lambda \lesssim 1 \text{ mm}$ . The third discrepancy is the significantly different plateau value for  $F$  for the two different interface models, which can be directly traced to the significantly different values at which  $\kappa_{\text{eff}}/\kappa$  saturates for  $L \gtrsim 5 \mu\text{m}$  for the two models.

It is very important to note that the saturation of  $\kappa_{\text{eff}}(L)/\kappa$  for  $L \gtrsim 5 \mu\text{m}$  is a result of the transport regime in silicon never becoming fully diffusive, even at  $L = 1 \text{ mm}$ . Since the reconstruction critically depends on the value of the ratio  $\kappa_{\text{eff}}(L)/\kappa$ , the fact that this ratio fails to reach a well-established physical limit casts severe doubt on the reliability of the whole reconstruction process based on the effective thermal conductivity. The fact that the effective thermal conductivity approach relies on the assumption of diffusive transport, which, in term, implies late times, was discussed in detail in [8] in the context of the transient thermal grating experiment. Failure to allow for sufficient time for transport to transition to diffusive, will result in an unreliable measurement and a poor reconstruction.

To illustrate the above point further, we consider the special case of one-dimensional transport ( $L \rightarrow \infty$ ) and define a time- and mode-dependent Knudsen number  $\text{Kn}_\omega(t) = \Lambda_\omega/\mathcal{D}(t)$  that characterizes the transport regime inside the silicon. Here,  $\mathcal{D}(t)$  is the characteristic heat penetration depth. It is defined as the length inside silicon, measured from the Al-Si interface, where the deviational temperature reaches 1% of the initial deviational temperature, i.e.  $\Delta T(\mathcal{D}(t)) = 0.01 \text{ K}$ . Figure 3-14a shows the mode dependent Knudsen number defined in this way inside silicon. The simulation is based on MC simulations of BTE using Holland silicon properties, experimental transmissivities, and noise-free relaxation profiles for 5 ns (similar to pump-probe experiment) plotted for the duration  $35 \text{ ps} \leq t \leq 5 \text{ ns}$  (the 35 ps is chosen since this

is the time that the surface temperature of Al starts to decrease from the initial value of  $\Delta T(t = 0) = 1$  K, implying that this is the time that the transport regimes begin to be observed in our measurement). The 21 lines in the figure correspond to 20 selected modes of data (there is a total of 1399 modes in the Holland data) and their average, the latter defined as the sum of the weighted Knudsen numbers of different frequencies (weighted by the density of states). We can see in the figure that for a significant number of modes, even at the end of the observation window ( $\sim 5$  ns), the Knudsen number is significantly larger than one, implying that diffusive behavior has yet to set in.

In order to further verify that the saturation in  $\kappa_{\text{eff}}$  observed in figure 3-13b is caused by non-diffusive effects, we performed long-time simulations of the 1D problem described above. In these simulations  $\kappa_{\text{eff}}$  was extracted at progressively later times, but always within a sampling window of 5 ns duration ( $t_{\text{final}} - t_{\text{initial}} = 5$  ns). Figure 3-14b shows  $\kappa_{\text{eff}}(L = \infty)/\kappa$  versus the end of measurement period,  $t_{\text{final}}$ , for different measurement times for Holland silicon properties, both experimental and DMM transmissivities, and noise-free relaxation profiles. The leftmost points in the figure correspond to a time window of  $t_{\text{final}} = 5$  ns, which is the time window used for the reconstruction data of figure 3-13b; the consistency between these values and the saturated values in figure 3-13b suggests that our 1D problem is a good representation of the physics of the 2D problem for the larger values of  $L$ .

Figure 3-14b clearly shows that  $\kappa_{\text{eff}}(L = \infty)/\kappa \rightarrow 1$  as  $t_{\text{final}}$  increases, as expected, since transport inside the silicon becomes more diffusive. The figure also shows that the value of  $\kappa_{\text{eff}}(L = \infty)/\kappa = 0.92$  observed for the experimental transmissivities is fortuitously high for that particular observation window and returns to values that are consistent with the DMM model for other observation windows. Although this large discrepancy between the values of  $\kappa_{\text{eff}}(L \rightarrow \infty)/\kappa$  for the  $t_{\text{final}} = 5$  ns window is somewhat fortuitous, it still serves to highlight the sensitivity of the effective thermal conductivity approach on the observation window, which casts serious doubt on its reliability (measurement of a material property should be independent of the measurement window to be considered reliable).

In summary, lack of diffusive behavior in the 2D-dots setup, as seen in figure 3-14, causes failure of the effective thermal conductivity approach. In contrast, as shown in sections 3.3.2–3.3.4, the approach proposed here does not suffer from such limitations.

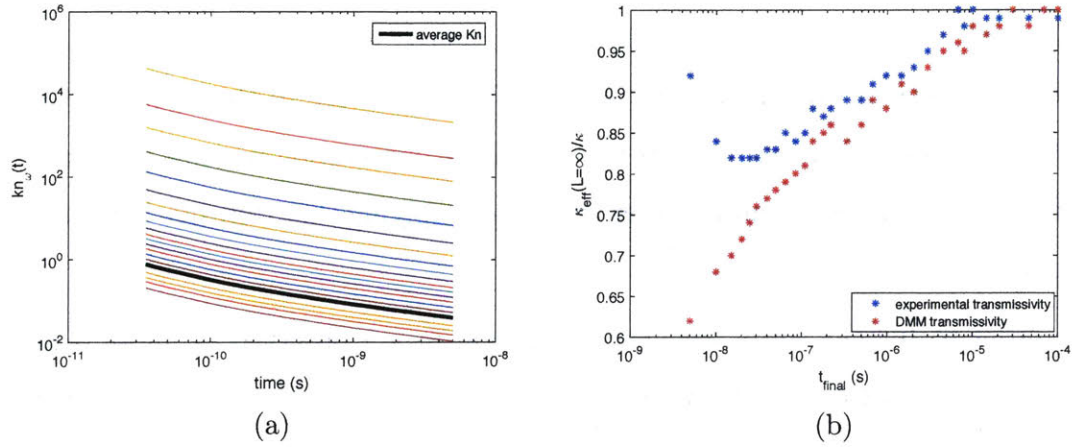


Figure 3-14: Non-diffusive behavior inside silicon. (a) Mode and time dependent Knudsen number inside silicon for pump-probe measurement time,  $0 < t < 5$  ns, based on BTE solution using Holland properties, experimental transmissivities, and noise-free relaxation profiles. (b) Effect of measurement time on transport regime inside silicon for both experimental and DMM transmissivities. The plot shows  $\kappa_{\text{eff}}(L = \infty)/\kappa$  for different measurement times. This quantity approaches 1 as the measurement window moves to later times.

# Chapter 4

## Validation on experimental data

In this chapter, we perform a direct comparison between DFT-derived phonon relaxation times and those reconstructed from experimentally measured temperature profiles in a two-dimensional transient thermal grating (2D-TTG) geometry [10]. The reconstruction is performed using the inverse problem framework proposed in Chapter 2. The Boltzmann transport equation (BTE) solutions are provided by the adjoint deviational Monte Carlo (MC) methodology [29–32]; in other words, as before, validity of Fourier’s law is never assumed. In addition to the above comparison, we evaluate the ability of the reconstruction methodology to perform on real experimental data and under conditions where measurements are available for only a portion of the length scales spanned by the material free paths; the latter is typically severely limiting for effective-thermal-conductivity-based methodologies [9]. Performing on real experimental data can be challenging due to the presence of noise but also other spurious signals (see figure 4-1b); in addition, it tests the hypothesis, implicit in this methodology, that the experimental setup can be adequately modeled using the BTE (subject to appropriate boundary conditions). The material used in the experiment and the reconstruction is silicon, with an *ab initio* [5] and a model based on the ShengBTE DFT package [69] being used for validation purposes (the material model).

This chapter is based on Ref. [11], where this material first appeared.

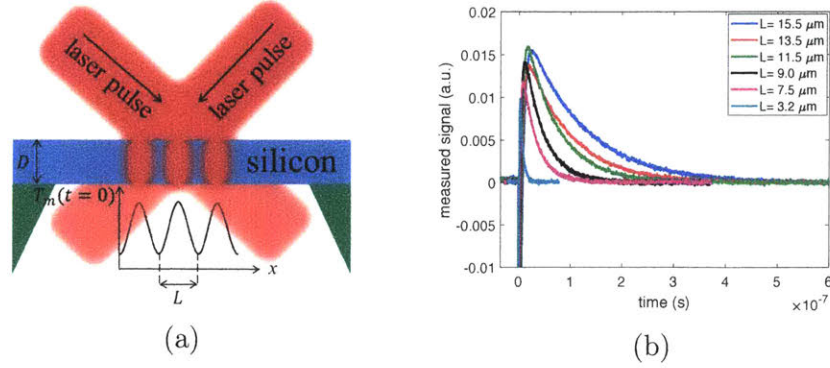


Figure 4-1: (a)- The 2D-TTG experiment; the Si film thickness is constant at  $D= 400$  nm. (b) A few examples of the measured signal for different length scales. Nineteen wavelengths in the range  $L = 1.6\text{--}21 \mu\text{m}$  were measured.

## 4.1 Formulation

The governing equations for phonon-mediated heat transport have been discussed previously in section 2.1.1. Here, we focus on the inverse problem formulation. Our goal, as before, is to obtain a reliable approximation to  $\tau_\omega$  by minimizing the discrepancy between the experimental temperature measurements and the BTE solutions. The objective function that needs to be minimized is

$$\min_{\mathbf{U}} \mathcal{L} = \min_{\mathbf{U}} \left[ \sum_{L, \mathbf{x}, t \geq t_0} w_L |c_L S_m(t, \mathbf{x}; L) - T_{\text{BTE}}(t, \mathbf{x}; L, \mathbf{U})| + \alpha \left| 1 - \frac{1}{3\kappa} \int_{\omega} C_\omega \tau_\omega(\mathbf{U}) v_\omega^2 d\omega \right| \right], \quad (4.1)$$

in which  $L$  denotes the grating period (problem characteristic length scale —see figure 4-1a),  $t_0 = t_0(L)$  is the first measurement time for each length scale used in the optimization (see section 4.2),  $S_m$  is the experimentally measured signals (see figure 4-1b)— different from  $T_m$  (see section 4.2), and  $w_L$  is a length scale dependent weight that ensures that all gratings contribute equally to the optimization; its value is given by  $w_L = 1/(nN_L)$ , where  $n$  is the number of different wavelengths for which data exist and  $N_L$  is the number of datapoints (in time) for each  $L^1$ . The parameter

<sup>1</sup>Note that  $w_L$  and  $N_L$  are introduced in this chapter since here the number of datapoints ( $N_L$ ) for each length scale due to limitation on the experimental setup is different. In Chapters 2 and 3,

$c_L$  that provides the optimal match between  $S_m$  and  $T_{\text{BTE}}$  can be calculated using a convex optimization formulation that has an analytical solution (see section 4.2).

## 4.2 Reconstruction

### 4.2.1 Optimization process

The optimization process in this section is similar to the one described in Chapter 2, however, here, we are assuming the existence of optical phonons as well as acoustic phonons, in particular, we are assuming  $M^{LA} = M^{TA_1} = M^{TA_2} = 3$  (a piecewise linear function with three segments, as before), while  $M^{LO} = M^{TO_1} = M^{TO_2} = 1$ . This choice of simpler model for optical phonons is due to their significantly smaller frequency range compared to acoustic phonons. Furthermore, we have assumed that the two transversal branches for both optical and acoustic phonons have the same relaxation time function. We have not observed any improvement in the reconstruction results using separate models for the transversal branches. This observation is due to the fact that the two transversal branches are very similar for silicon. We have also used “graduated optimization” as before, however, since here we are assuming  $\tau^{TA_1} = \tau^{TA_2}$  and  $\tau^{TO_1} = \tau^{TO_2}$ , we have only three stages instead of four.

In the first stage, we assume that all relaxation times (six branches) are described by one line (one branch with  $M^S = 1$ ), similar to the process described in Chapter 2, leading to two unknowns.

In the second stage, the three acoustic branches are still assumed to be the same but the intended number of segments is used, similarly, all optical branches are assumed to be the same with the intended number of segments. Thus, the number of unknowns in this stage is  $6 + 2 = 8$ .

The third stage is the final stage of the optimization, therefore, starting from the optimized values of stage two, it proceeds using the intended number of unknowns ( $6 \times 2 + 2 \times 2 = 16$  unknowns). The optimized values at this stage are the final values

---

since the temperatures were generated synthetically, we chose  $N_L = 100$  for all length scales  $L$ .

parameterizing the relaxation time function.

To reduce cost, similar to the optimization process described in Chapter 2, we have used variable number of particles in the MC simulations at different stages, in particular, during the first and second stages of the optimization process we used  $\mathcal{N}_{\text{BTE}} = 10^4$  particles for calculation of  $T_{\text{BTE}}$ , while during the third stage of the process, the number of particles was increased to  $\mathcal{N}_{\text{BTE}} = 10^5$ .

## 4.2.2 Optimization in the presence of experimental data

It has been shown in [10] that the measurements in 2D-TTG ( $S_m$ ) are proportional to the temperatures ( $T_m$ ); the proportionality coefficient, however, is not known in general. This coefficient can be determined by requiring the phononic part of the signal (that is, ignoring the electronic excitation part of the signal, the negative values in the signal at very early times in figure 4-1b) be accurately represented (in a least squares sense) by the solutions of the BTE for the temperature. In other words, we solve the following sub-problem

$$c_L = \arg \min_{c_L} \sum_{t>t_0, \mathbf{x}} (c_L S_m(t, \mathbf{x}; L) - T_{\text{BTE}}(t, \mathbf{x}; L, \mathbf{U}))^2, \quad (4.2)$$

for each length scale  $L$ , where  $c_L$  is the length scale dependent proportionality constant. Equation (4.2) is a convex problem that can be solved by differentiating the right hand side (RHS) with respect to  $c_L$ , which leads to the following solution

$$c_L = \frac{\sum_{t>t_0, \mathbf{x}} S_m(t, \mathbf{x}; L) T_{\text{BTE}}(t, \mathbf{x}; L, \mathbf{U})}{\sum_{t>t_0, \mathbf{x}} S_m(t, \mathbf{x}; L)^2} \quad (4.3)$$

Next, we determine the time  $t_0(L)$ , which appears in the objective function  $\mathcal{L}$ , and equations (4.2) and (4.3).  $t_0(L)$  represents the time, for each length scale  $L$ , for which electronic excitation effects are negligible. To determine  $t_0(L)$  we have fitted a bi-exponential profile to each signal and chose the point at which the fitted electronic excitation signal (the exponential component of the signal with smaller decay time) reaches a small fraction ( $\gamma$ ) of the phononic signal (the exponential component of

the signal with larger decay time). Note that this does not imply an exponential/bi-exponential response assumption in any part of the reconstruction process; this process has only been used to determine the time after which the electronic excitation effects are negligible. More specifically, for each wavelength, first we solve the following set of optimization problems

$$\min_{A, B, \tau_{\text{ph}}, \tau_{\text{e}}} \sum_{t=0}^{t^*} \left| A \exp\left(-\frac{t}{\tau_{\text{ph}}}\right) - B \exp\left(-\frac{t}{\tau_{\text{e}}}\right) - S_{\text{m}}(t, \mathbf{x}; L) \right|, \quad (4.4)$$

in which  $0 < t^* = t^*(L) < t_f$ , where  $t_f = t_f(L)$  is the final measurement time for that wavelength. This means that we fit a bi-exponential function and solve for the optimal set  $\{A, B, \tau_{\text{ph}}, \tau_{\text{e}}\}$  for all possible values of  $t^*$ . This approach is motivated by the realization that the relaxation behavior is not necessarily exponential for either of the phononic or electronic components; therefore, by taking the “worst case” solution for  $t^*$ , as explained below, we ensure that our estimate is as conservative as possible.

We have used the MATLAB `fminsearch` function to calculate the parameters  $A = A(L, t^*)$ ,  $B = B(L, t^*)$ ,  $\tau_{\text{ph}} = \tau_{\text{ph}}(L, t^*)$ , and  $\tau_{\text{e}} = \tau_{\text{e}}(L, t^*)$ , which converges very fast for such low-dimensional well-behaved objective functions. After the parameters  $A$ ,  $B$ ,  $\tau_{\text{ph}}$ , and  $\tau_{\text{e}}$  for different  $t^*$  for a given length scale are determined, we proceed to find the candidate starting times  $t'_0 = t'_0(L, t^*)$  via

$$\frac{B \exp\left(-\frac{t'_0}{\tau_{\text{e}}}\right)}{A \exp\left(-\frac{t'_0}{\tau_{\text{ph}}}\right)} = \gamma \quad (4.5)$$

which has the solution in the form of

$$t'_0 = \ln\left(\frac{\gamma A}{B}\right) \bigg/ \left(\frac{1}{\tau_{\text{ph}}} - \frac{1}{\tau_{\text{e}}}\right). \quad (4.6)$$

The actual  $t_0 = t_0(L)$  (to be used in the objective function  $\mathcal{L}$ ) is then determined as the largest value calculated from (4.6) among the set of all optimized  $A$ ,  $B$ ,  $\tau_{\text{ph}}$ , and  $\tau_{\text{e}}$ , that is  $t_0 = \max_{t^*} t'_0(L, t^*)$ . Here, we have used  $\gamma = 0.001$ . We have also verified that using  $\gamma = 0.01$  yields the same result.

### 4.3 Validation

The reconstruction method has been applied to the experimental measurements of a 2D-TTG geometry on silicon, obtained from [10]. A sketch of the 2D-TTG geometry and a few examples of measured relaxation signals can be found in figure 4-1. As it was stated previously, the negative values in the signal at very early times in the figure are associated with electronic excitations that are not modeled in this work; as a result, the corresponding data are not used in the optimization process. In other words, optimization is performed over data satisfying  $t > t_0(L)$  for each measurement wavelength.

The reconstructed results are compared to two sets of DFT data for silicon. The first is described in [5] and will be referred to as “model A”; the second model, which features no separation in branches, was obtained using the ShengBTE DFT package [69] and will be referred to as “model B”. There are  $2 \times 6 + 2 \times 2 = 16$  unknowns for “model A”. For “model B”, since there is only one function, we used only one piecewise linear function with three segments, leading to 6 unknowns. We did not see any improvement by increasing the number of segments to five.

A comparison between the DFT calculated properties and optimization results is provided in figure 4-2. Overall, the level of agreement between the DFT and corresponding reconstructed data is very good, both at the relaxation time level (figures 4-2a and 4-2b) and the free path CDF level (figures 4-2c). However, closer examination of figure 4-2 reveals some discrepancies between each reconstructed set of data and its corresponding DFT model which could be instructive to investigate. We have eliminated the possibility that these discrepancies arise from removing the early-time signal by changing the time window over which we assume the electronic excitation part vanishes (time  $t_0$ ) and observing no change in the reconstructed properties (see the discussion in section 4.2). This is expected since the electronic excitation part is a very small fraction of each signal (see figure 4-1b). Another possibility is imperfect reconstruction due to the lack of measurements at all relevant length scales (the length scales used in the experiments lie in the range  $1.6 \leq L \leq 21 \mu\text{m}$ , which

does not cover the sub-micron region (2 nm–1  $\mu$ m) of the free path range of silicon (2 nm–100  $\mu$ m)). On the other hand, as discussed in [9], the reconstruction methodology used here is quite robust to such scarcity of data. This is further investigated below. A final possibility is that the DFT data does not exactly capture the experimental material behavior most likely due to non-idealities associated with the experiment (e.g., experimental error, boundary conditions, material characterization and purity, etc.).

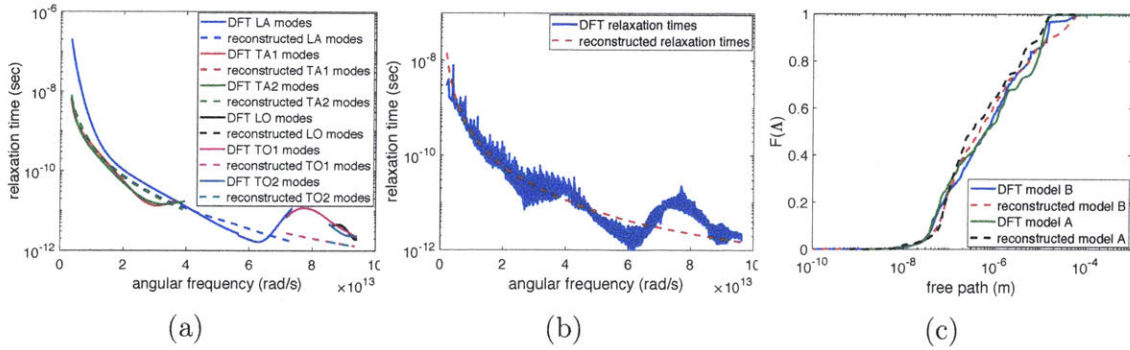


Figure 4-2: Comparison between reconstructed material properties and DFT calculations. (a) Reconstructed and “model A” DFT calculations of relaxation times. (b) Reconstructed and “model B” DFT calculations of relaxation times. (c) Reconstructed, “model A”, and “model B” DFT calculation of free path distribution.

In order to investigate the above further, and in the absence of a direct benchmark, we use the experimental data as a benchmark. In other words, we assess the accuracy of the reconstructed  $\tau_\omega$  by comparing the temperature relaxation profiles it predicts (obtained by solving the BTE using that data) to the experimental temperature profiles; we expect that the more accurate the reconstruction, the closer the temperature profiles predicted by it will be to the experimental traces. Figure 4-3a shows a comparison between the experimental traces and the DFT prediction for two wavelengths; figure 4-3b shows the corresponding comparison (for the same wavelengths as figure 4-3a) between the experimental traces and those predicted using the reconstructed  $\tau_\omega$ . The trends observed in figures 4-3a and 4-3b are representative of other wavelengths, not shown here in the interest of brevity. We first remark that the excellent match observed in figure 4-3b highlights the high accuracy of the reconstruction methodology used here, even in the presence of noise in both measurement and MC simulations,

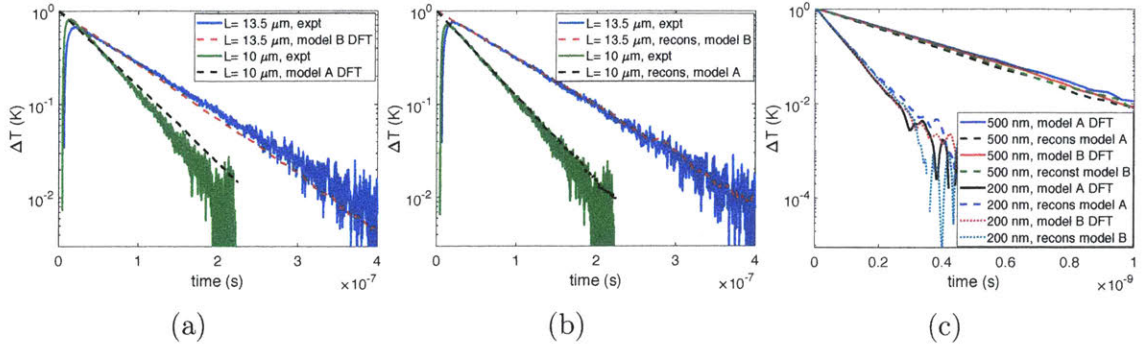


Figure 4-3: Comparison between experimentally measured (“expt”), reconstructed (“recons”), and DFT-based simulated temperature profiles. (a) DFT vs. experimental measurements. (b) Reconstructed vs. experimental measurements. (c) DFT vs. reconstructed for sub-micron regime. All “recons” results are based on the reconstructions of figure 4-2.

as well as the presence of other spurious signals (electronic excitation). Comparison between the two figures also reveals that the discrepancies are clearly smaller in the case of the reconstructed  $\tau_\omega$ ; this implies that most of the discrepancy between the reconstructed and DFT data is likely due to differences between the idealized (DFT) and real (experimental) material behavior.

As noted above, the reconstruction method used here is able to accurately reconstruct material properties even at length scales for which no experimental measurements exist (see section 4.4 for additional discussion). This is demonstrated in figure 4-3c, which compares the relaxation profile as predicted by the reconstructed and DFT data for  $L = 500 \text{ nm}$  and  $200 \text{ nm}$  (which is significantly smaller than the smallest length scale for which experimental data was available,  $L = 1.6 \mu\text{m}$ ). The overall agreement is very good; an analysis of the sensitivity of this reconstruction to each optimization parameter can be found in section 4.4. We do note, however, that in the “small- $L$ ” regime, transport becomes increasingly ballistic and thus less sensitive to relaxation times. We therefore performed a second numerical experiment to ensure that the above assertion is indeed true.

In this second experiment, we performed the reconstruction using a subset of the available experimental data ( $10 \mu\text{m} \leq L \leq 21 \mu\text{m}$ ) and used some of the remaining data ( $L = 1.8 \mu\text{m}$  and  $L = 2.4 \mu\text{m}$ ) for comparison with our predictions. The re-

sults are shown in figure 4-4 (for a sensitivity analysis, see section 4.4). The good agreement between measured and simulated temperatures (after  $t_0(1.8 \mu\text{m}) = 2.3 \text{ ns}$  and  $t_0(2.4 \mu\text{m}) = 2.8 \text{ ns}$ ) shows that the reconstruction method used here provides reliable predictions even for length scale regimes not represented in the experimental data. This is due to the fact that this method retains a spectral parametrization of phonon properties. This is in sharp contrast to effective-thermal-conductivity-based approaches which project the information in the experimental data onto a few-parameter model of the process (e.g. an exponential response with an effective thermal conductivity/diffusivity), thereby significantly reducing its information content, while introducing error (Fourier-like behavior is only valid for sufficiently large length scales and late times [8]). This reduction in information content aggravates the ill-posedness of the reconstruction, requiring intervention, such as imposition of smoothness requirements [13], to avoid unphysical solutions.

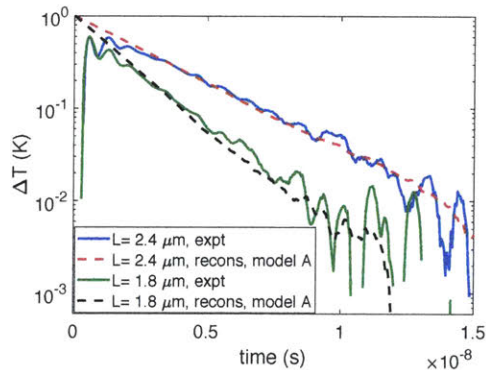


Figure 4-4: Comparison between experimentally measured (“expt”) temperature relaxation profiles and those predicted by reconstructed data (“recons”) using information of experiments in the range  $L = 10\text{--}21 \mu\text{m}$ .

## 4.4 Sensitivity analysis of the solution

In this section, we present results on the sensitivity of the objective function  $\mathcal{L}$  to the parameters of the relaxation time function,  $\tau_{\omega_j}^S$ , in the neighborhood of  $\hat{\mathbf{U}} =$

$\arg \min_{\mathbf{U}} \{\mathcal{L}\}$ , in which

$$\hat{\mathbf{U}} = (\hat{\tau}^{LA}, \hat{\tau}^{TA_1}, \hat{\tau}^{TA_2}, \hat{\omega}^{LA}, \hat{\omega}^{TA_1}, \hat{\omega}^{TA_2}, \hat{\tau}^{LO}, \hat{\tau}^{TO_1}, \hat{\tau}^{TO_2}, \hat{\omega}^{LO}, \hat{\omega}^{TO_1}, \hat{\omega}^{TO_2}) \quad (4.7)$$

is the solution that the optimization algorithm has converged to (see equation (2.8)). In particular, we perturb each  $\hat{\tau}_{\hat{\omega}_j}^S$  (here,  $S \in \{LA, TA_1, TA_2, LO, TO_1, TO_2\}$  and  $\hat{\omega}_j \in \{\hat{\omega}_0^S, \dots, \hat{\omega}_{MS}^S\}$ ) by generating samples from  $\tau_{\hat{\omega}_j}^S \in [0.1\hat{\tau}_{\hat{\omega}_j}^S, 10\hat{\tau}_{\hat{\omega}_j}^S]$  while keeping all other components of  $\mathbf{U}$  the same as the optimal solution and plot the resulting variation in  $\mathcal{L}$  as a function of the perturbation. To ensure that the noise in the optimization process is included, in our BTE solutions we use the same number of particles as in the final stage of the optimization, namely,  $\mathcal{N}_{\text{BTE}} = 10^5$ . The perturbed parameters are sampled using the uniform distribution

$$\log \tau_{\hat{\omega}_j}^S = 2R - 1 + \log \hat{\tau}_{\hat{\omega}_j}^S, \quad (4.8)$$

where  $R \sim U([0, 1])$  is generated from the standard uniform distribution.

Figure 4-5 shows the sensitivity of the objective function value for “model A” at the minimum point (figure 4-2a) for medium to long (figure 4-5a) and short (figure 4-5b) free paths. We observe that for the medium/long free paths (figure 4-5a) there is a strong sensitivity to the solution; furthermore, we observe that the results shown in figure 4-2 correspond to the minimum of all parameters. The plots in figure 4-5a correspond to parameters that influence  $\Lambda_\omega \gtrsim 10$  nm, which are  $\tau_{\omega_1}^{LA}$ ,  $\tau_{\omega_2}^{LA}$ ,  $\tau_{\omega_0}^{TA}$ ,  $\tau_{\omega_1}^{TA}$ ,  $\tau_{\omega_2}^{TA}$ , and  $\tau_{\omega_3}^{TA}$ . Note that the sensitivity of  $\tau_{\omega_0}^{LA}$  has not been provided in figure 4-5a since the density of states for *LA* modes for  $\omega < 8 \times 10^{12}$  rad/s is zero.

Figure 4-5b shows the sensitivity plots for short free path phonons, with region of influence  $\Lambda_\omega \lesssim 10$  nm, which are  $\tau_{\omega_3}^{LA}$ ,  $\tau_{\omega_0}^{TO}$ ,  $\tau_{\omega_1}^{TO}$ ,  $\tau_{\omega_0}^{LO}$ , and  $\tau_{\omega_1}^{LO}$ . We observe that although due to the stronger diffusive behavior the sensitivity to these parameters is less than medium/long free paths, the algorithm, despite the noise in the BTE solutions, has been able to converge to a solution close to the optimal point for  $\tau_{\omega_3}^{LA}$ ,  $\tau_{\omega_0}^{TO}$ , and  $\tau_{\omega_1}^{TO}$ , with any discrepancies being a result of noise (uncertainty in value of  $\mathcal{L}$ ). The sensitivity of the solution to optical phonons due to their small free

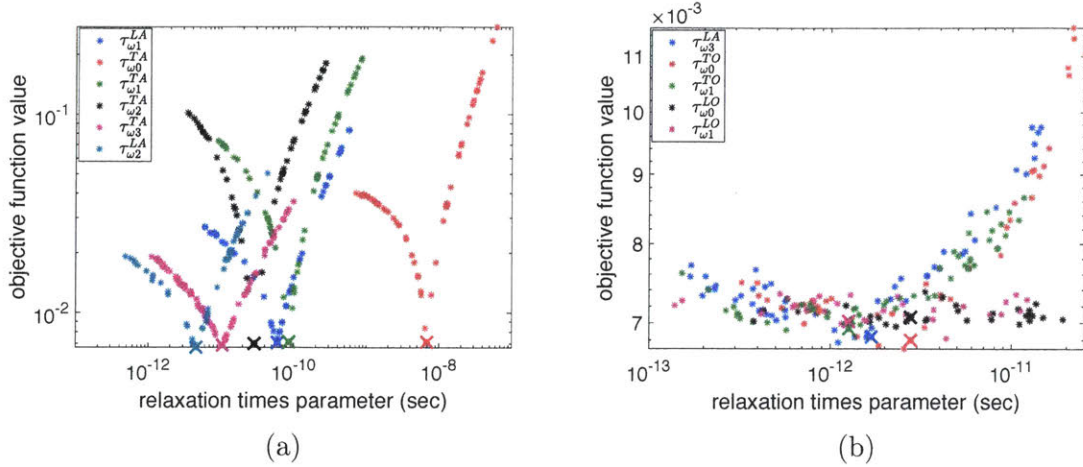


Figure 4-5: Sensitivity analysis of the solution of the optimization algorithm at the minimum point using “model A” (figure 4-2a) for (a)- long/medium and (b)- short free paths. The “x” signs show the minimum point (the solution from the optimization algorithm).

path and group velocity and their small range in frequency domain is expected to be significantly less than the acoustic phonons. This lack of sensitivity is stronger in longitudinal optical phonons due to their significantly smaller density of states compared to the transverse optical phonons. In fact, we have not observed any significant sensitivity to longitudinal optical phonon parameters. On the other hand, this lack of sensitivity is just a reflection of the small influence of the *LO* branch on the temperature profiles (see Chapter 3 and [9] for a more extensive discussion in the context of reconstructing interface properties). In other words, any uncertainty in determining  $\tau_{\omega_j}^{LO}$  will have a very small effect on the ability of the reconstructed relaxation times to describe the temperature relaxation profiles associated with the material.

In order to demonstrate the above assertion, we have generated temperature relaxation profiles using the parameters  $\tau_{\omega_0}^{LO}$  and  $\tau_{\omega_1}^{LO}$  that are perturbed from the optimization solution  $\hat{\tau}_{\omega_0}^{LO}$  and  $\hat{\tau}_{\omega_1}^{LO}$  by one order of magnitude in each direction (similar to range of perturbations in figure 4-5). Figure 4-6a shows a comparison between the temperature based on the optimal solution and the perturbed solution ( $0.1\hat{\tau}_{\omega_0}^{LO}$ ,  $10\hat{\tau}_{\omega_0}^{LO}$ ,  $0.1\hat{\tau}_{\omega_1}^{LO}$ , and  $10\hat{\tau}_{\omega_1}^{LO}$ ) for  $L = 200$  nm, which is an order of magnitude smaller than the smallest length scale available. This result verifies that the lack of sensitiv-

ity in the value of the objective function (in the inverse problem) reflects the weak dependence of the temperature profiles on the corresponding parameter (in the forward problem). In other words, even if measurements at a length scale one order of magnitude below the minimum experimentally available measurement were available, accurate reconstruction of the  $LO$  branch relaxation times would likely have been impossible. Figure 4-6b shows the same comparison for  $L = 20$  nm which is two orders of magnitude smaller than the smallest experimentally available measurement. Here, the effect of perturbation of  $LO$  parameters is observable but still insignificant.

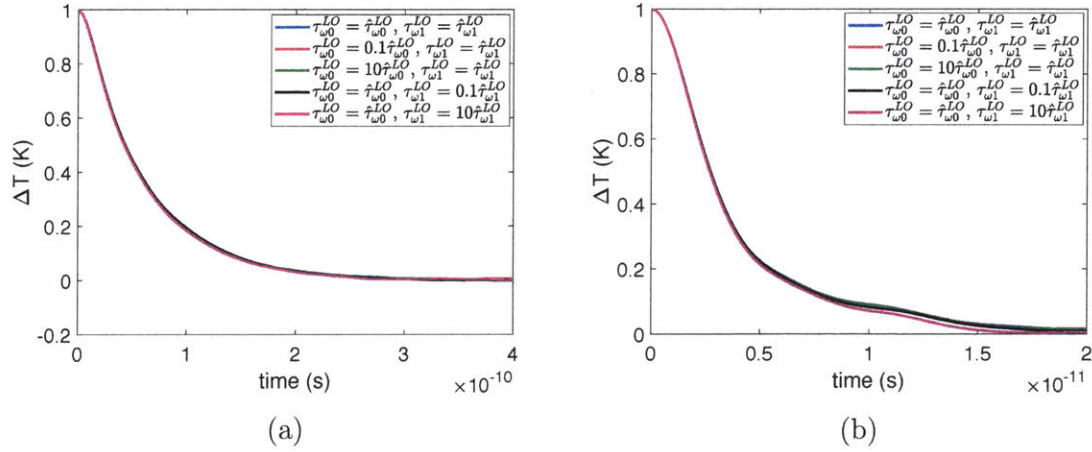


Figure 4-6: Comparison between temperature profiles based on optimal solutions and perturbed  $LO$  solutions at small length scales for (a)-  $L = 200$  nm and (b)-  $L = 20$  nm.

Figure 4-7 shows the sensitivity of the objective function value for “model B” at the minimum point (figure 4-2b) for medium to long (figure 4-7a) and short (figure 4-7b) free paths. The same conclusions as figure 4-5 are valid here as well. Figure 4-8 shows the sensitivity analysis for the results shown in figure 4-4 (“model A” with a subset of experimental data used as inputs to the optimization). We observe that, due to limited range of length scales in the experimental measurements, the overall sensitivities are smaller than those of figure 4-5. At the same time the conclusions drawn from figure 4-5 are still valid, namely, sufficient sensitivity exists to make reasonably accurate reconstructions that reproduce the experimental temperature relaxation profiles.

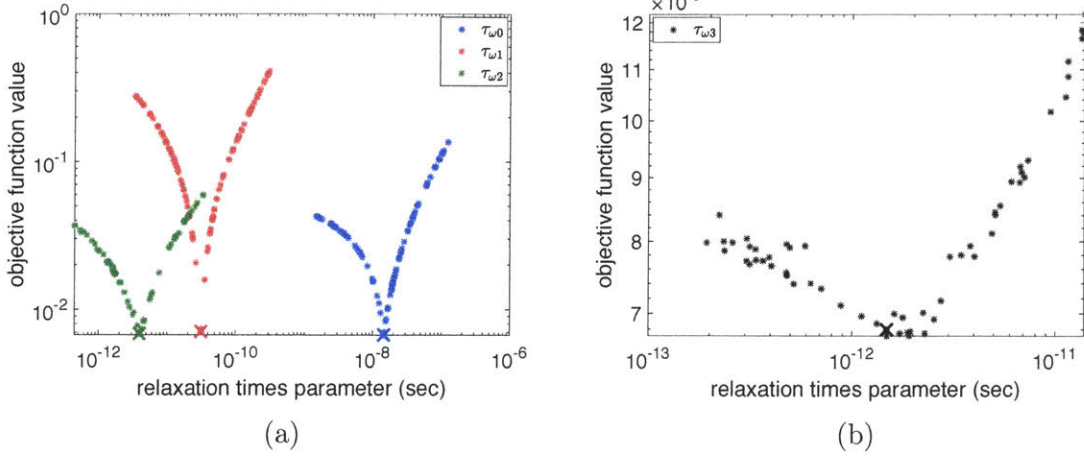


Figure 4-7: Sensitivity analysis of the solution of the optimization algorithm at the minimum point using “model B” (figure 4-2b) for (a)- long/medium and (b)- short free paths. The “x” signs show the minimum point (the solution from the optimization algorithm).

In summary, the results provided in figures 4-5–4-8 indicate that provided sufficient measurements exist for the spectral makeup of the material property of interest to be adequately sampled, the proposed method is expected to provide a reasonably accurate reconstruction of this material property even if measurements do not exist for all lengthscales. In other words, although the lack of measurement at small length

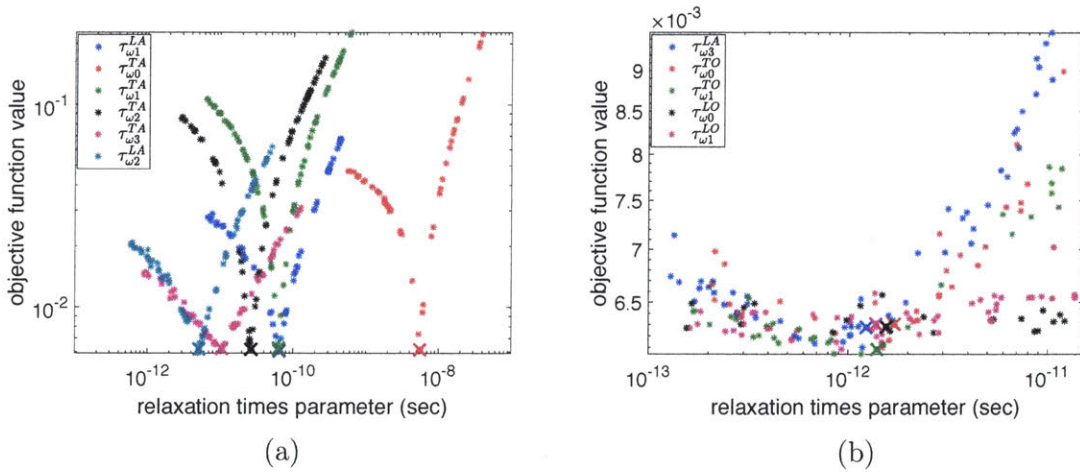


Figure 4-8: Sensitivity analysis of the solution of the optimization algorithm at the minimum point with length scales in the range  $L = 10\text{--}21 \mu\text{m}$  (figure 4-4) for (a)- long/medium and (b)- short free paths. The “x” signs show the minimum point (the solution from the optimization algorithm).

scales is expected to lead to degradation of the quality of the reconstructed properties (at a minimum because the amount of available information is smaller) this is not as detrimental as in effective-thermal-conductivity-type of approaches. The sensitivity analysis performed above can be useful in identifying parameters to which the objective function is relatively insensitive and which, as a result, may not be accurately determined. Finally, the noise magnitude observed in figures 4-5b, 4-7b and 4-8b implies that if more particles are used in the MC simulations (for obtaining the BTE solution), more accurate reconstruction of short free path/relaxation time phonons and possibly even for the  $LO$  branches, is possible.

# Chapter 5

## Reliability of the optimization process and results

In this chapter we study the reliability of the optimization process (objective function, multi-stage NM algorithm) discussed in the thesis. With the exception of the material in section 5.3, due to the non-convexity of the optimization problem, the results presented in this chapter are numerical, obtained in the context of a case study, namely the 1D-TTG experiment. In section 5.1 we address the uniqueness of the solution by studying the uniqueness of the minimum of the objective function (2.9) using a global optimization algorithm. Motivated by some of the numerical results obtained in section 5.1, in sections 5.2 and 5.3 we show that the thermal response (the solution of the forward problem) for a given phonon free path distribution is non-unique. In section 5.4 we quantify the statistical properties of the optimized solution given the uncertainty in the input fields (temperatures) from a Bayesian perspective. Finally, in section 5.5, we provide a probabilistic analysis of the optimization process and result, namely, a quantification of the stochastic nature of the optimization result due to the uncertainty in measurements (input temperature profiles), stochastic initial conditions, and the forward model (noisy forward MC simulations of the BTE).

## 5.1 Uniqueness of the optimization solution

The relaxation time reconstruction results that we have provided so far in this thesis show that the proposed optimization framework has been successful in converging to a solution that appears consistent with the input data  $T_m$ . However, due to the non-convexity of the objective function, the following question arises: how certain can we be that the optimized solution is the only solution that is capable of generating thermal responses that match the input temperature profiles? Unfortunately, due to the complexity of the BTE and the related inverse problems, we cannot provide a definite answer to this question that is applicable to any geometry; instead, here, we have focused on a specific problem, the 1D-TTG experiment, and attempted to study the uniqueness of the solution for this particular case using a global optimization algorithm.

Due to the success of the NM algorithm for our problem, here, we use a globalized version of NM algorithm, referred to as the “globalized bounded Nelder-Mead (GBNM)” [70], to study the uniqueness of the solution. The GBNM algorithm is very similar to the NM algorithm described before; however, instead of performing the optimization once, starting from one initial condition<sup>1</sup>, it repeats the whole optimization process many times, starting from different probabilistically correlated initial conditions. In particular, the distribution of initial conditions is chosen such that the probability of sampling from regions that contain either previous initial conditions or previous optimization solutions (equivalent to a single NM process) is lower. In this fashion, it is guaranteed, in a stochastic sense, that for a finite number of iterations, the whole domain of the parameter space is sampled more efficiently [70].

The initial conditions in GBNM are sampled from the distribution

$$\psi(\mathbf{U}) = \frac{\max_{\mathbf{U}' \in \Gamma} \tilde{p}(\mathbf{U}') - \tilde{p}(\mathbf{U})}{\int_{\Gamma} [\max_{\mathbf{U}' \in \Gamma} \tilde{p}(\mathbf{U}') - \tilde{p}(\mathbf{U})] d\mathbf{U}}, \quad (5.1)$$

---

<sup>1</sup>Or the most favorable of a number of uncorrelated randomly chosen initial conditions, such as in the process described in section 2.2.3.

where  $\Gamma$  is the domain of the parameter space  $\mathbf{U}$ , and  $\tilde{p}(\mathbf{U})$  is

$$\tilde{p}(\mathbf{U}) = \frac{p(\mathbf{U})}{\int_{\Gamma} p(\mathbf{U}) d\mathbf{U}}, \quad (5.2)$$

in which

$$p(\mathbf{U}) = \frac{1}{N_s} \sum_{i=1}^{N_s} \mathcal{N}(\mathbf{U}; \mathbf{U}_i, \Sigma), \quad (5.3)$$

where the sum is over the  $N_s$  initial conditions or converged solutions of the previous optimizations. For instance, at the  $k$ -th optimization process,  $N_s = 2(k - 1)$ , corresponding to  $k - 1$  previously sampled initial conditions and  $k - 1$  previously converged optimization solutions. Equation (5.3) creates a Gaussian mixture distribution with the means located at either the already sampled initial conditions or the converged solutions; equation (5.2) normalizes this distribution based on the domain of the parameter space to ensure it represents a probability distribution in that domain, and finally equation (5.1) calculates its complement, which is the distribution that the initial condition for the next NM optimization process is generated from.

Let  $\Sigma \in \mathbb{R}^{12 \times 12}$  be the covariance matrix of the Gaussian distribution (note that here  $\dim(\mathbf{U}) = 12$ ; see below), whose diagonal elements here are taken to be 1% of the size of the parameter space in each direction (as suggested in Ref. [70]) —see below. Furthermore, its off-diagonal elements are taken to be zero (assumption of uncorrelated  $\mathbf{U}$  components [70]). Therefore,

$$\begin{aligned} \Sigma_{i,i} &= 0.09, & i &\in \{1, \dots, 2M^S + 2\} \\ \Sigma_{i,i} &= 0.01(\omega_M - \omega_0), & i &\in \{2M^S + 3, \dots, 4M^S\} \\ \Sigma_{i,j} &= 0, & i &\in \{1, \dots, 4M^S\}, j \in \{1, \dots, 4M^S\}, i \neq j. \end{aligned} \quad (5.4)$$

Since one of the requirements in the GBNM algorithm is boundedness of the parameter space, here, we are assuming  $\log(\tau_{\omega_j}^S) \in [-13, -4]$ ; this is a conservative choice since it includes all relaxation time values bounded by 0.1 ps and 100  $\mu$ s, given that for Si the relaxation time values, considering all frequencies and branches, are between 1 ps and 100 ns. This choice of bounds leads to a variance of  $0.01(13 - 4) = 0.09$  (equa-

tion (5.4), first line). We are also assuming  $\omega_j^S \in [\omega_0, \omega_M]$ , where  $\omega_0$  is the smallest and  $\omega_M$  is the largest frequency considering all branches, hence, the variance of these parameters is  $0.01(\omega_M - \omega_0)$  (equation (5.4), second line). We have also assumed that the two  $TA$  branches are the same, leading to  $4M^S = 12$  total unknowns (as seen in equation (5.4) as well).

For this test, we have generated synthetic temperature profiles for material Si in the TTG geometry for  $10 \text{ nm} < L < 100 \text{ }\mu\text{m}$  by solving the BTE using IFFT, and used the generated data to perform the global optimization. More detail on the GBNM algorithm can be found in [70].

We have performed the global optimization algorithm for both the *ab initio* and the Holland models. The results are provided in figure 5-1. This figure shows the values of the objective function  $\mathcal{L}$  (equation (2.9)) versus the distance between the “true” solution and the vector  $\mathbf{U}$  corresponding to the objective function value. These values are the result of the natural path of the GBNM algorithm. In other words, we have recorded the points that the GBNM algorithm has explored throughout the global optimization process and plotted them in this figure, for both models. The measure labeled as “distance” is defined as

$$\text{distance} := \frac{\int_{\omega} \left| \log \left( \frac{\tau_{\omega}}{\tau_{\omega}^*} \right) \right| D_{\omega} d\omega}{\int_{\omega} D_{\omega} d\omega}, \quad (5.5)$$

where  $\tau_{\omega}^*$  represents the “true” solution. Therefore, “distance” is a measure of average difference between any frequency-dependent relaxation time function that we calculate through the GBNM process and the true relaxation time function, weighted by the density of states at each frequency. Here,  $\omega$ , as before, contains information of both different frequencies and branches.

The main observation from figure 5-1 is that the bottom left of the cluster of datapoints in both plots represents a monotonically increasing function, which means that the closer we are to the true solution, the smaller the value of the objective function becomes, and more importantly, this is a monotonic behavior as we approach the true solution. This implies that the solution is unique; non-uniqueness would

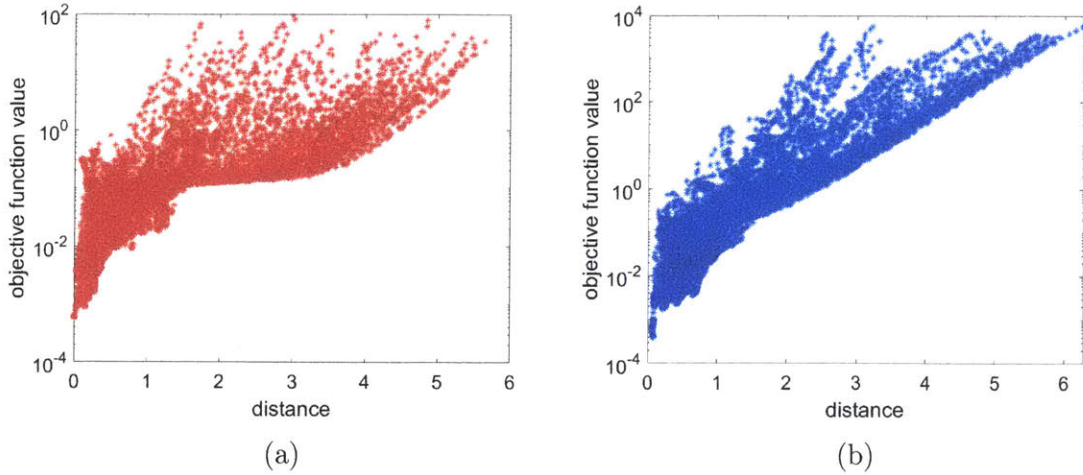


Figure 5-1: The value of the objective function versus the distance (see equation (5.5)) between the points sampled during GBNM and the true solution for (a)- Holland and (b)- *ab initio* model.

be implied by points in the lower right hand corner of the diagrams (low value of objective function, while the distance from the solution is large). Here we note that the number of datapoints in each plot in figure 5-1 is approximately 1 million. While exploring the whole parameter space with high resolution is not feasible due to the high dimension of the problem studied here ( $\dim(\mathbf{U}) = 12$ ), the general behavior of the objective function, such as the monotonicity described above (which itself implies

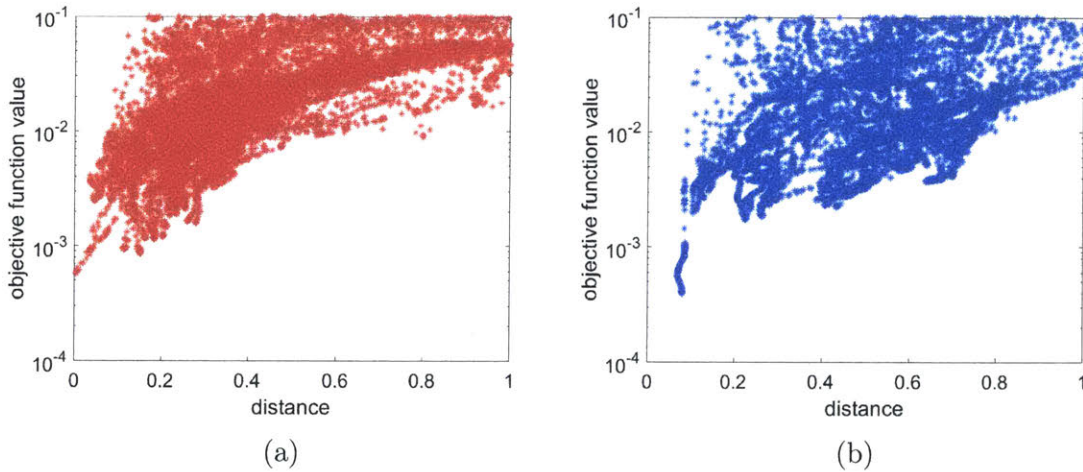


Figure 5-2: The value of the objective function versus the distance (see equation (5.5)) between the points sampled during GBNM and the true solution for (a)- Holland and (b)- *ab initio* model.

the uniqueness), will likely not change if more iterations are used (and consequently an even better exploration of the parameter space is performed). Figure 5-2 shows a magnified version of the plots provided in figure 5-1 near the correct solution.

## 5.2 Does the free path distribution define a unique relaxation time function?

The large number of datapoints presented in figure 5-1 provides us with valuable information about the behavior of the objective function. Below, we will be using this information to study the relation of the relaxation times function to the free path distribution, a common quantity of interest that many researchers treat as a material property for predicting the thermal response of materials at sub-micron regimes.

Figure 5-3 shows a plot similar to what has been presented in figure 5-1, this time for the free path distribution, for the *ab initio* model (using the same data generated based on the GBNM algorithm). The “relative distance” labeled in the figure is defined using the following relationship

$$\text{relative distance} := \int_{\Lambda} \left| 1 - \frac{f(\Lambda)}{f^*(\Lambda)} \right| d\Lambda, \quad (5.6)$$

where  $f^*$  represents the “true” free path distribution; the definition of free path distribution  $f$  can be found in section 3.3.2. The main observation from figure 5-3 is the existence of many points close to the true solution (the leftmost region in the figure) with very large values of the objective function, unlike the plots in figure 5-1. This implies that there are many points (representing different  $\mathbf{U}$  values or different relaxation time functions) that have a free path distribution that is almost the same as the true solution with significantly different thermal response (a large value of the objective function). This behavior seriously questions the wisdom at using the free path distribution as a material property; a quantity is considered a material property if it predicts a unique physical response if other variables (other material properties, geometry, etc) are not altered.

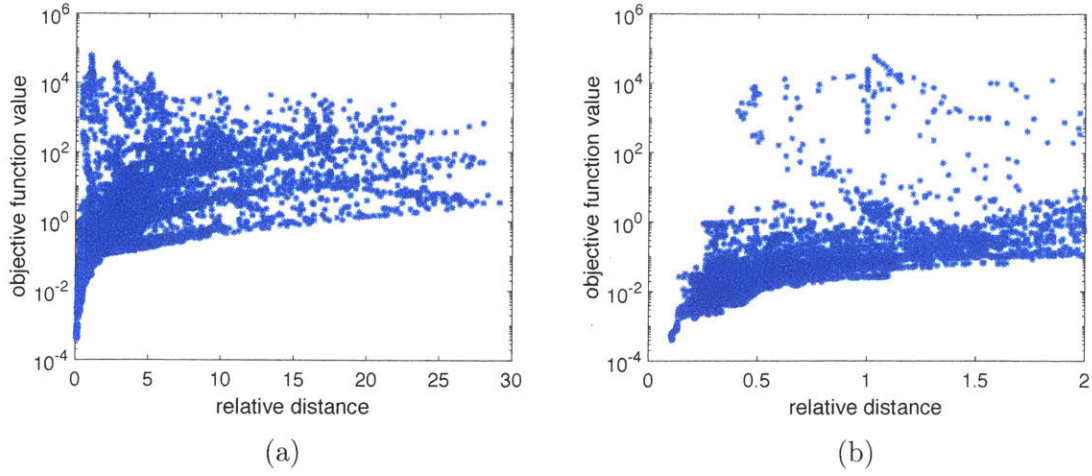


Figure 5-3: The value of the objective function versus the relative distance (see equation (5.6)) between the points sampled during GBNM and the true solution for *ab initio* model. (b) is the magnified version of (a) close to the correct solution.

In order to investigate the above, namely, the nonuniqueness of the thermal response for a given free path distribution, in more detail, we have performed an optimization that directly studies this hypothesis. We considered the objective function

$$\min_{\mathbf{U}} \int_{\Lambda} |\mathbf{f}^*(\Lambda) - \mathbf{f}(\Lambda)| d\Lambda, \quad (5.7)$$

which attempts to find free path distributions that match the true free path distribution by searching in the parameter space  $\mathbf{U}$ . Note that  $\mathbf{U}$  enters the objective function through the definition of the free path distribution  $\Lambda_{\omega} = v_{\omega} \tau_{\omega}(\mathbf{U})$ . We have used the NM algorithm to perform this optimization with IFFT as the forward simulation method and have used the 1D-TTG geometry as before with the Holland model for Si. We have repeated the optimization multiple times starting from different initial conditions for  $\mathbf{U}$  in order to also study the effect of different initial conditions on the optimization process. Figure 5-4 shows the relaxation times and the free path distribution obtained from one of these optimizations as well as the temperature profile predicted by the optimized  $\mathbf{U}$  versus the true profile at 100 nm length scale. As it is expected from equation (5.7), the reconstructed free path distribution matches the true free path distribution. At the same time, both the relaxation time function,

and more importantly, the thermal responses do not match, even though all other material properties, as well as the geometry are kept fixed. The mismatch in thermal responses also exists at other length scales.

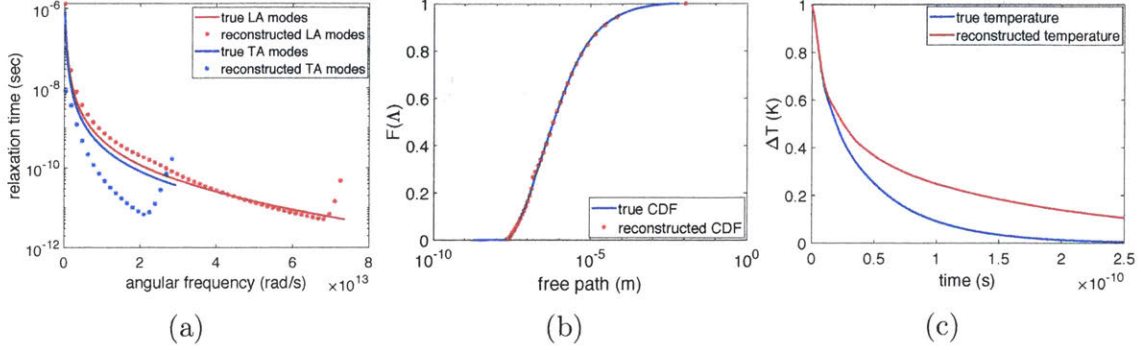


Figure 5-4: (a)- The reconstructed relaxation time function and (b)- free path distribution and (c)- temperature profile at 100 nm wavelength based on equation (5.7) objective function.

The results provided in figures 5-3 and 5-4 clearly show, from a numerical perspective, that the free path distribution cannot be used reliably as a material property. In the following subsection we show rigorously, that a given free path distribution, depending on its functional form, can correspond to many different relaxation time functions.

### 5.3 On the inability of the free path distribution to uniquely define the relaxation time function

In the previous section, we have observed through multiple numerical experiments that the free path distribution is unable to predict a unique thermal behavior. Here, we prove that this likely is an artifact of replacing relaxation times function with free path distribution, which fails to preserve all the information contained in the relaxation times function.

**Theorem:** For a given material, if there are two phonon frequencies,  $\omega_1$  and  $\omega_2$ , such that  $C_\omega(\omega_1)v_\omega(\omega_1) = C_\omega(\omega_2)v_\omega(\omega_2)$ , the relaxation time function is non-unique

for a given free path distribution.

*Proof:* We consider two different relaxation time functions,  $\tau_\omega$  and  $\tau'_\omega$ , with free path distributions  $f(\Lambda)$  and  $f'(\Lambda)$ , respectively;  $\tau_\omega$  and  $\tau'_\omega$  are identical ( $\tau_\omega = \tau'_\omega$ ) for all  $\omega \neq \omega_1, \omega_2$  and

$$\tau'_\omega(\omega_1) = \frac{\tau_\omega(\omega_2)v_\omega(\omega_2)}{v_\omega(\omega_1)}, \quad \tau'_\omega(\omega_2) = \frac{\tau_\omega(\omega_1)v_\omega(\omega_1)}{v_\omega(\omega_2)}, \quad (5.8)$$

where we assume  $v_\omega(\omega_2) \neq v_\omega(\omega_1)$ .

From the relaxation time function  $\tau_\omega$  one can derive the free path  $\Lambda_\omega$  and frequency-dependent heat conductivity  $\kappa_\omega$  ( $\kappa_\omega := C_\omega v_\omega^2 \tau_\omega / 3$ ), considered here as a pair  $(\Lambda_\omega, \kappa_\omega) = (v_\omega \tau_\omega, C_\omega v_\omega^2 \tau_\omega / 3)$ . Since the two relaxation time functions are identical at all  $\omega \neq \omega_1, \omega_2$ , their corresponding  $(\Lambda_\omega, \kappa_\omega)$  pairs are also identical at all  $\omega \neq \omega_1, \omega_2$ . To show that their pairs are identical for all frequencies, and thus *they have the same free path distribution*, we now show that

$$(\Lambda_\omega(\omega_1), \kappa_\omega(\omega_1)) = (\Lambda'_\omega(\omega_2), \kappa'_\omega(\omega_2)) \quad (5.9)$$

and

$$(\Lambda_\omega(\omega_2), \kappa_\omega(\omega_2)) = (\Lambda'_\omega(\omega_1), \kappa'_\omega(\omega_1)) \quad (5.10)$$

which imply that they are identical at all frequencies. Here, we have used the definition  $(\Lambda_\omega(\omega_i), \kappa_\omega(\omega_i)) := (v_\omega(\omega_i)\tau_\omega(\omega_i), C_\omega(\omega_i)v_\omega^2(\omega_i)\tau_\omega(\omega_i)/3)$ , for  $i = 1, 2$  (and similarly for the  $(\Lambda'_\omega(\omega_i), \kappa'_\omega(\omega_i))$  pair).

The above can be shown by writing

$$\tau'_\omega(\omega_1)v_\omega(\omega_1) = \left[ \frac{\tau_\omega(\omega_2)v_\omega(\omega_2)}{v_\omega(\omega_1)} \right] v_\omega(\omega_1) = \tau_\omega(\omega_2)v_\omega(\omega_2), \quad (5.11)$$

where we have used equation (5.8) to obtain the second relationship. The heat con-

ductivity value corresponding to this free path is

$$\begin{aligned}
\frac{1}{3}C_\omega(\omega_1)v_\omega^2(\omega_1)\tau'_\omega(\omega_1) &= \frac{1}{3}C_\omega(\omega_1)v_\omega(\omega_1)[v_\omega(\omega_1)\tau'_\omega(\omega_1)] \\
&= \frac{1}{3}C_\omega(\omega_2)v_\omega(\omega_2)[v_\omega(\omega_2)\tau_\omega(\omega_2)] \\
&= \frac{1}{3}C_\omega(\omega_2)v_\omega^2(\omega_2)\tau_\omega(\omega_2), \tag{5.12}
\end{aligned}$$

where we have used both the assumption  $v_\omega(\omega_2) \neq v_\omega(\omega_1)$  and equation (5.11) to obtain the second equality. Relations (5.11) and (5.12) are equivalent to relation (5.10).

Using the same process as (5.11) and (5.12) for  $\omega_2$  (replacing  $\omega_1$  by  $\omega_2$ ), we obtain relation (5.9).

These results (relations (5.9) and (5.10)) imply that  $f(\Lambda) = f'(\Lambda)$  for all free paths while there are frequencies for which  $\tau_\omega(\omega) \neq \tau'_\omega(\omega)$  ■.

Figure 5-5 shows the plot of  $C_\omega v_\omega$  for the Holland and the *ab initio* models. We observe that in both cases, there are many points with different frequencies, considering all branches, that have the same  $C_\omega v_\omega$  value. In particular, for the *ab initio* model, even considering one branch, there are many points on each curve that have the same  $C_\omega v_\omega$  value. The existence of many such points will aggravate the non-uniqueness of the relaxation time function for a given free path distribution, since we can pick many  $\omega_i$  and  $\omega_j$  pairs (either one of these pairs or multiple of them simultaneously) for which  $C_\omega(\omega_i)v_\omega(\omega_i) = C_\omega(\omega_j)v_\omega(\omega_j)$  and introduce a relaxation time function  $\tau'_\omega$ , following the recipe introduced in the theorem (in particular (5.8)) which is different from the true relaxation time function (the *ab initio* model,  $\tau_\omega$ ) but has the same free path distribution as the *ab initio* model. This also justifies the behavior observed in figure 5-4, that is, different relaxation time functions for the *ab initio* (as well as Holland) model exist that correspond to the same free path distribution. While this non-uniqueness of the relaxation time function for a given free path distribution may not be catastrophic on its own, the fact that these different functions predict different thermal behaviors, as we have seen in figure 5-4c, implies that a given free path distribution provides insufficient information for predicting the

thermal response. The results provided in this section prove that **the free path distribution is not a material property.**

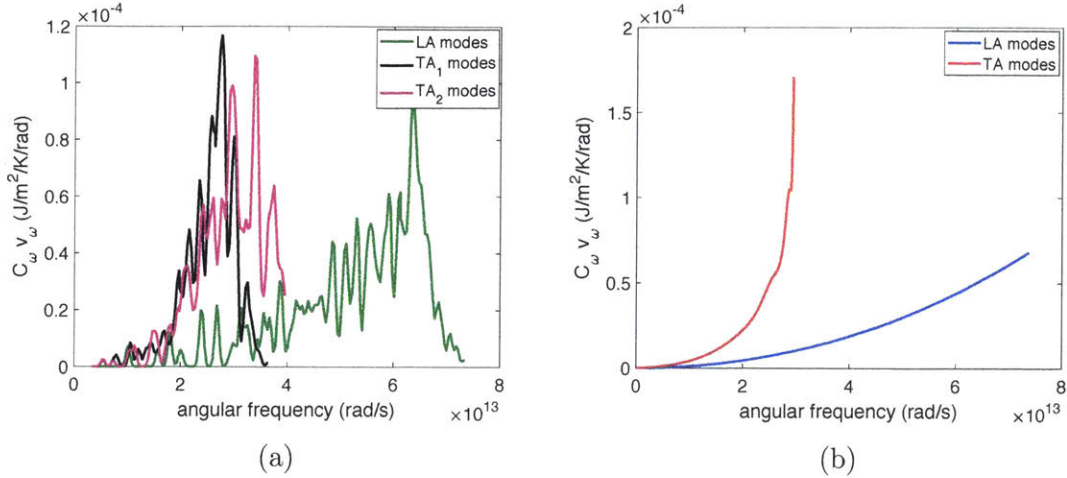


Figure 5-5: The plot of  $C_\omega v_\omega$  versus frequency for the (a)- *ab initio* and the (b)-Holland model..

## 5.4 Bayesian approach to relaxation time reconstruction

In this section we study the effect of noise in the temperature measurement on the reconstruction of the relaxation time function  $\tau_\omega^S$ , using a probabilistic approach that is based on Bayesian inference. This approach does not involve the objective function and the previously proposed multi-stage optimization process, therefore providing a different perspective. The results of this section also provide valuable information on the accuracy in the reconstruction of various parts of the spectrum of  $\tau_\omega$  due to noise in the measurements. A probabilistic approach that involves the objective function and the optimization process is left to section 5.5.

The Bayesian approach is based on inferring the distribution of the parameter under study (the frequency-dependent relaxation time function) by modifying its initial (prior) distribution based on observations (noisy temperature profiles). For this purpose, we have generated synthetic input temperature profiles for material Si using the *ab initio* material model (assuming the two *TA* branches to be the same)

in the TTG geometry for  $10 \text{ nm} < L < 100 \text{ } \mu\text{m}$  by solving the BTE using IFFT. To model the noise in the input temperature profiles we add noise to the (deterministic) BTE solutions ( $T_{\text{BTE}}$ ), namely,

$$T_{\text{m}} = T_{\text{BTE}}(t, \mathbf{x}; L, \mathbf{U}) + \epsilon, \quad (5.13)$$

where  $\epsilon \sim \mathcal{N}(0, \sigma_{\text{m}}^2)$ , with  $\sigma_{\text{m}} = 0.01 \text{ K}$ . This value of  $\sigma_{\text{m}}$  is chosen such that it is an upper bound to the noise observed in the experimental measurement. The noise in the experimental measurement was evaluated by comparing the experimental temperature profiles of Chapter 4 with noise-free BTE simulations. We are interested in inferring the posterior distribution, that is, the distribution of the parameter  $\mathbf{U}$ , when a set of thermal spectroscopy temperature measurements,  $T_{\text{m}}$ , are being observed

$$p(\mathbf{U} | \{T_{\text{m}}(t, \mathbf{x} = 0; L)\}_{t,L}) \propto p(\{T_{\text{m}}(t, \mathbf{x} = 0; L)\}_{t,L} | \mathbf{U}) \pi(\mathbf{U}), \quad (5.14)$$

where  $\pi(\mathbf{U})$  is the prior distribution of the parameter  $\mathbf{U}$  before the observations, and  $\{T_{\text{m}}(t, \mathbf{x} = 0; L)\}_{t,L}$  are the set of all temperature measurements (observation). The temperature in the 1D-TTG geometry is sinusoidal as function of the location,  $\mathbf{x}$ ; therefore, we only need (and measure) its amplitude, located at  $\mathbf{x} = 0$ . In other words, the “{ }” in (5.14) does not run through different  $\mathbf{x}$  values. Assuming that the noise in the measurements is generated from independent and identically distributed random variables, we can further simplify (5.14) by writing:

$$\begin{aligned} p(\mathbf{U} | \{T_{\text{m}}(t, \mathbf{x} = 0; L)\}_{t,L}) &\propto \prod_{t,L} p(T_{\text{m}}(t, \mathbf{x} = 0; L) | \mathbf{U}) \pi(\mathbf{U}) \\ &= \prod_{t,L} \mathcal{N}(T_{\text{m}}(t, \mathbf{x} = 0; L); T_{\text{BTE}}(t, \mathbf{x} = 0; L, \mathbf{U}), \sigma_{\text{m}}^2) \\ &\quad \times \mathcal{N}(\mathbf{U}; \mu, \Sigma), \end{aligned} \quad (5.15)$$

where  $\mu \in \mathbb{R}^{12}$  corresponds to the parameters at the true material relaxation time function  $\tau_{\omega}^S(\mathbf{U} = \mu)$  (or any other point in its vicinity) and  $\Sigma \in \mathbb{R}^{12 \times 12}$  is the

covariance matrix of the prior distribution, whose elements here are taken to be

$$\begin{aligned}
\Sigma_{i,i} &= 1, & i \in \{1, \dots, 2M^S + 2\} \\
\Sigma_{i,i} &= 10^{26}, & i \in \{2M^S + 3, \dots, 4M^S\} \\
\Sigma_{i,j} &= 0, & i \in \{1, \dots, 4M^S\}, j \in \{1, \dots, 4M^S\}, i \neq j.
\end{aligned} \tag{5.16}$$

Here, we have assumed that the prior follows a Gaussian distribution around the correct solution. This is due to the fact that here we are more interested in the sensitivity of the reconstructed property, the relaxation time function, to the noise in the temperature measurement. Therefore, instead of the least-informative uniform distribution, we are assuming a prior with higher probability around the correct solution. This is motivated by our observation in the previous optimizations, that is, the relaxation time function in all those cases has converged to a solution close to the correct function. In other words, the Bayesian analysis is a complement to the analyses of section 5.1, since while the results provided in section 5.1 shows that the objective function has a global minimum, here we study how sensitive the objective function is to the measurement noise in the vicinity of that global minimum.

The posterior distribution (5.15) is sampled using the Metropolis-Hastings (MH) algorithm. Here, we use a symmetric Gaussian distribution

$$q(\cdot|\cdot) \sim \mathcal{N}(\cdot; \cdot, \Sigma_q), \tag{5.17}$$

for the proposal distribution, where

$$\begin{aligned}
(\Sigma_q)_{i,i} &= 10^{-3}, & i \in \{1, \dots, 2M^S + 2\} \\
(\Sigma_q)_{i,i} &= 10^{23}, & i \in \{2M^S + 3, \dots, 4M^S\} \\
(\Sigma_q)_{i,j} &= 0, & i \in \{1, \dots, 4M^S\}, j \in \{1, \dots, 4M^S\}, i \neq j.
\end{aligned} \tag{5.18}$$

The values of  $(\Sigma_q)_{i,i}$  have been determined empirically. A large value of  $(\Sigma_q)_{i,i}$  will explore a larger region in the parameter space, but will take more sampling points

to fill the space (a lower resolution of the parameter space), while a smaller value leads to a more localized search (higher resolution of the parameter space), but may not explore the parameter space thoroughly (or require more iterations to do so). The acceptance rate for the chosen proposal distribution is 0.36 which is close to the optimal value of 0.23 for multi-dimensional variables [71]. We have also used  $N_{\text{MH}} = 10^6$  sample points in the MH algorithm where the first  $10^5$  samples were used as the burn-in samples. The MH algorithm is described in Algorithm 1, in which  $U([a, b])$  is a uniform random distribution in  $[a, b]$  interval.

---

**Algorithm 1** Metropolis-Hastings for  $p(\mathbf{U} | \{T_m(t, \mathbf{x} = 0; L)\}_{t,L})$

---

**Require:** measurements:  $\{T_m(t, \mathbf{x} = 0; L)\}_{t,L}$ ; BTE forward simulation algorithm:  $T_{\text{BTE}}$ ; number of sample points:  $N_{\text{MH}}$   
generate  $\mathbf{U}_0^{\text{MH}} \sim \mathcal{N}(\mu, \Sigma)$   
simulate  $\forall(t, L) : T_{\text{BTE}}(t, \mathbf{x} = 0; L, \mathbf{U}_0^{\text{MH}})$   
**for**  $k = 1$  to  $k = N_{\text{MH}}$  **do**  
    generate  $\mathbf{U}' \sim \mathcal{N}(\mathbf{U}_{k-1}^{\text{MH}}, \Sigma_q)$   
    simulate  $\forall(t, L) : T_{\text{BTE}}(t, \mathbf{x} = 0; L, \mathbf{U}')$   
    calculate  $\alpha \leftarrow \min \left\{ 1, \frac{\prod_{t,L} \mathcal{N}(T_m(t, \mathbf{x}=0; L); T_{\text{BTE}}(t, \mathbf{x}=0; L, \mathbf{U}'), \sigma_m^2) \mathcal{N}(\mathbf{U}'; \mu, \Sigma)}{\prod_{t,L} \mathcal{N}(T_m(t, \mathbf{x}=0; L); T_{\text{BTE}}(t, \mathbf{x}=0; L, \mathbf{U}_{k-1}^{\text{MH}}), \sigma_m^2) \mathcal{N}(\mathbf{U}_{k-1}^{\text{MH}}; \mu, \Sigma)} \right\}$   
    generate  $u \sim U([0, 1])$   
    **if**  $u < \alpha$  **then**  
         $\mathbf{U}_k^{\text{MH}} \leftarrow \mathbf{U}'$   
    **else**  
         $\mathbf{U}_k^{\text{MH}} \leftarrow \mathbf{U}_{k-1}$   
    **end if**  
**end for**  
**return**  $p(\mathbf{U} | \{T_m(t, \mathbf{x} = 0; L)\}_{t,L}) \leftarrow \frac{1}{N_{\text{MH}}} \sum_{k=1}^{N_{\text{MH}}} \mathbb{1}_{\mathbf{U}=\mathbf{U}_k^{\text{MH}}}$

---

The pairwise posterior marginals for different pairs of the components of the unknown ( $\mathbf{U}$ ) are plotted as scatter-plots in figures 5-6 (for  $LA$  modes) and 5-7 (for  $TA$  modes). These figures provide useful information regarding the sensitivity of different elements of  $\mathbf{U}$  to presence of the measurement noise compared to each other. For instance, in figure 5-6 we observe that  $\mathbf{U}_3$  can be reconstructed with more accuracy compared to other elements of  $\mathbf{U}$  (sharper distributions) —considering only the elements of  $\mathbf{U}$  corresponding to  $LA$  mode. In the same figure we also observe that there is a negative correlation (defined as  $\text{corr}(x, y) := \text{cov}(x, y) / (\sigma_x \sigma_y)$ , where  $\sigma_x^2$  and  $\sigma_y^2$

are the variances of random variables  $x$  and  $y$ , respectively) between  $\mathbf{U}_2$  and  $\mathbf{U}_9$ , as well as  $\mathbf{U}_3$  and  $\mathbf{U}_{10}$ ; this is expected since  $\mathbf{U}_2$  corresponds to the relaxation time value at  $\mathbf{U}_9$  (as the segmentation point between the first and second lines on the relaxation time function of the  $LA$  modes), and similarly,  $\mathbf{U}_3$  corresponds to the relaxation time value at  $\mathbf{U}_{10}$  (as the segmentation point between the second and third lines on the relaxation time function of the  $LA$  modes). A stronger version of this correlation can also be observed in figure 5-7 for  $TA$  modes, between  $\mathbf{U}_6$  and  $\mathbf{U}_{11}$  (as the segmentation point between the first and second lines on the relaxation time function of the  $TA$  modes), and similarly,  $\mathbf{U}_7$  and  $\mathbf{U}_{12}$  (as the segmentation point between the second and third lines on the relaxation time function of the  $TA$  modes). We also observe that, overall, the distributions in figure 5-7 are sharper than 5-6, implying a more accurate reconstruction of the parameters of the  $TA$  modes. This could be due to the assumption that the two  $TA$  branches have been approximated by the same function, which consequently led to their greater influence on the thermal behavior. Note that each branch has 6 unknowns, leading to  $\binom{6}{2} = 15$  pairs (number of plots) in each figure.

Once we infer the distribution of different components of  $\mathbf{U}$ , we can calculate the distribution of relaxation time function as a function of its frequency using equation (2.7). The results are provided in figure 5-8. We have also plotted the true relaxation time functions in this figure. We observe that for  $LA$  modes, at frequencies around  $\omega = 6 \times 10^{13}$  rad/s, the distribution is sharper than other frequencies, implying that a relatively more accurate reconstruction of the value of relaxation time at those frequencies is possible. On the other hand, the uncertainty at very large frequencies ( $\omega \gtrsim 6.5 \times 10^{13}$  rad/s) is more than the other ranges of the frequency. A similar trend can be observed for  $TA$  modes. Overall, by comparing the two plots in figure 5-8, we conclude that the reconstruction of  $TA$  branches is more accurate, as it was stated previously.

In order to obtain a better picture of the shape of the distributions at different frequencies, we have also plotted the distributions at a few specific frequencies (equivalent to cross-sections at different frequencies in figure 5-8). Figures 5-

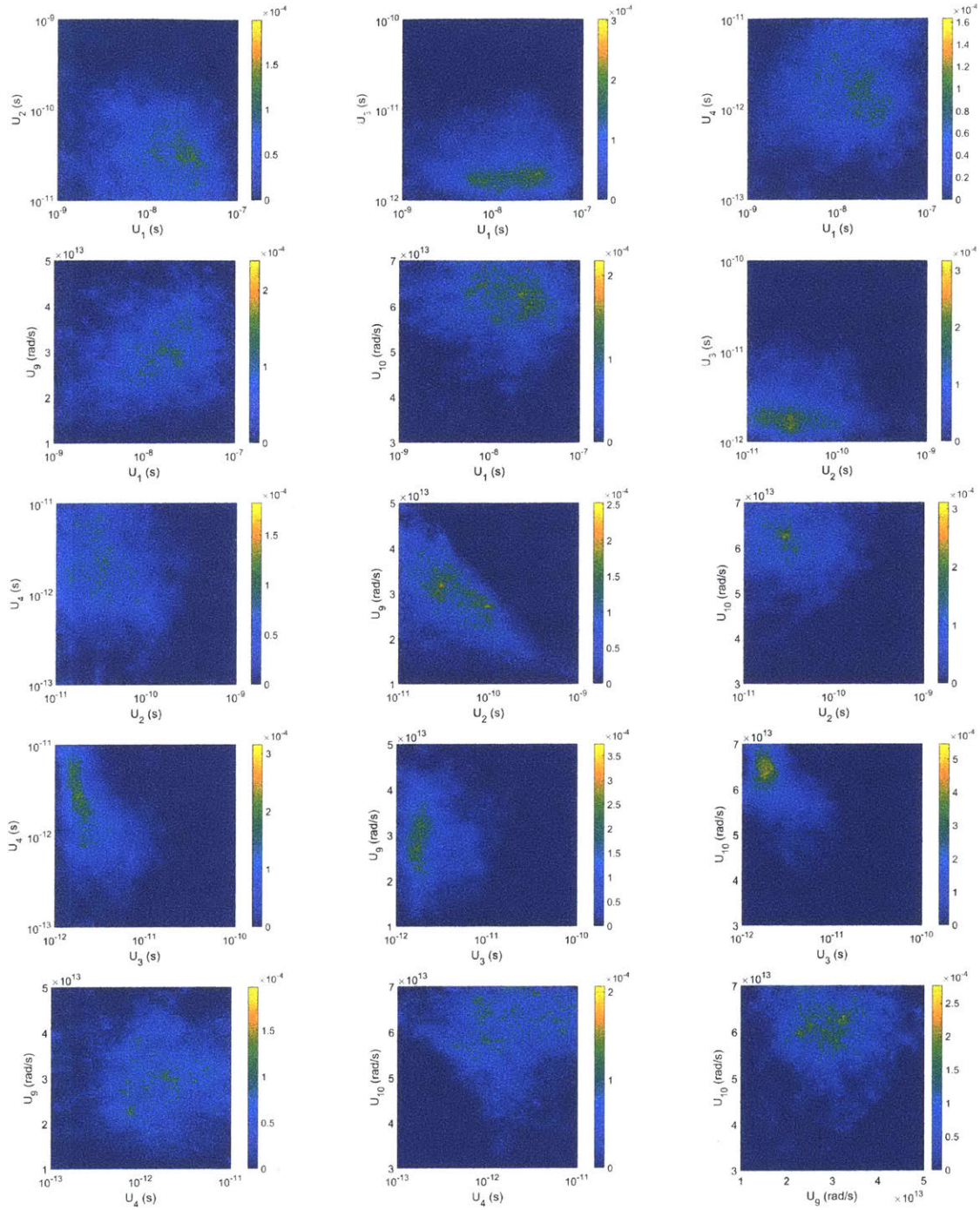


Figure 5-6: Pairwise posterior marginals of different pairs of the parameters of the *LA* mode.

9 and 5-10 show the prior distribution,  $\pi(\tau_\omega)$ , versus the posterior distribution,  $p(\tau_\omega | \{T_m(t, \mathbf{x} = 0; L)\}_{t,L})$ , for a few frequencies of *LA* and *TA* modes, respectively. We observe that in most cases, the posterior distribution has become significantly

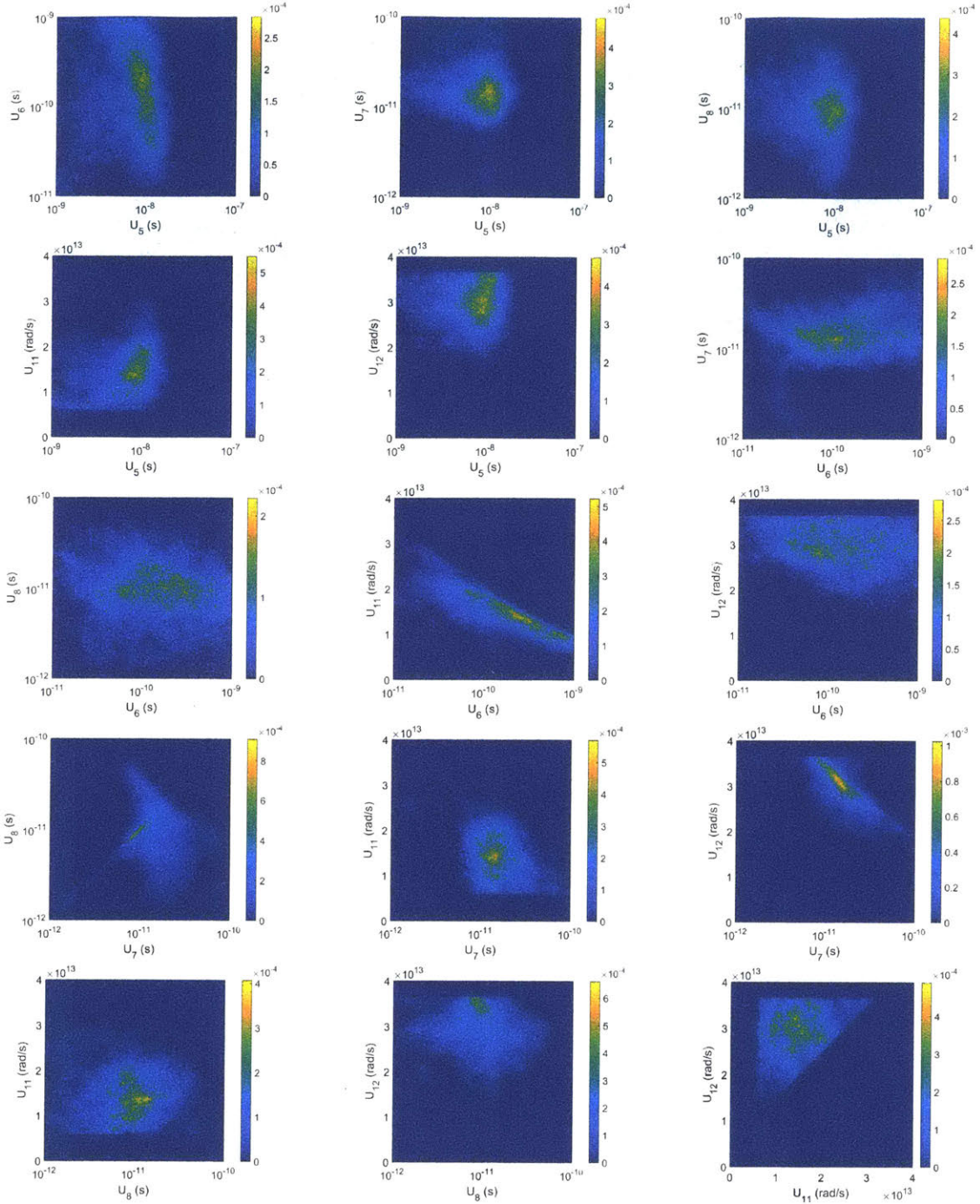


Figure 5-7: Pairwise posterior marginals of different pairs of the parameters of the *TA* mode.

narrower compared to the prior distribution, implying that the chosen prior distribution has been wide enough to avoid bias in inferring the posterior distribution. The distributions in *TA* case are sharper, as can also be seen in figure 5-8. The distribu-

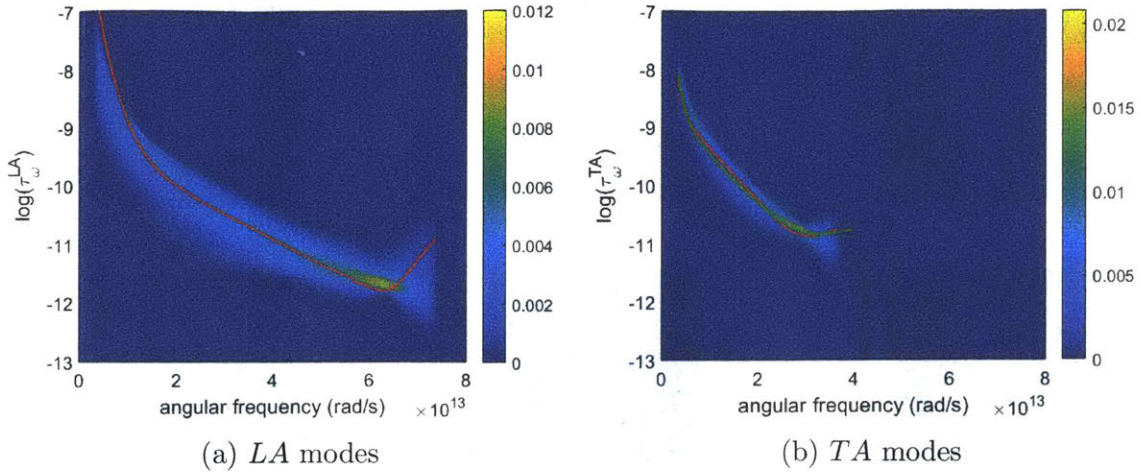


Figure 5-8: Contour plot of the probability density of the frequency-dependent relaxation times distribution of *LA* and *TA* modes. The red line in (a) denotes the true  $\tau_{\omega}^{LA}$ , while the red line in (b) denotes the true  $\tau_{\omega}^{TA_1}$  and the green line in (b) denotes the true  $\tau_{\omega}^{TA_2}$ .

tion at very high frequencies ( $\omega = 7$  rad/s in figure 5-9 and  $\omega = 3.5$  rad/s in figure 5-10) is wider than the other frequencies, consistent with our observation of figure 5-8.

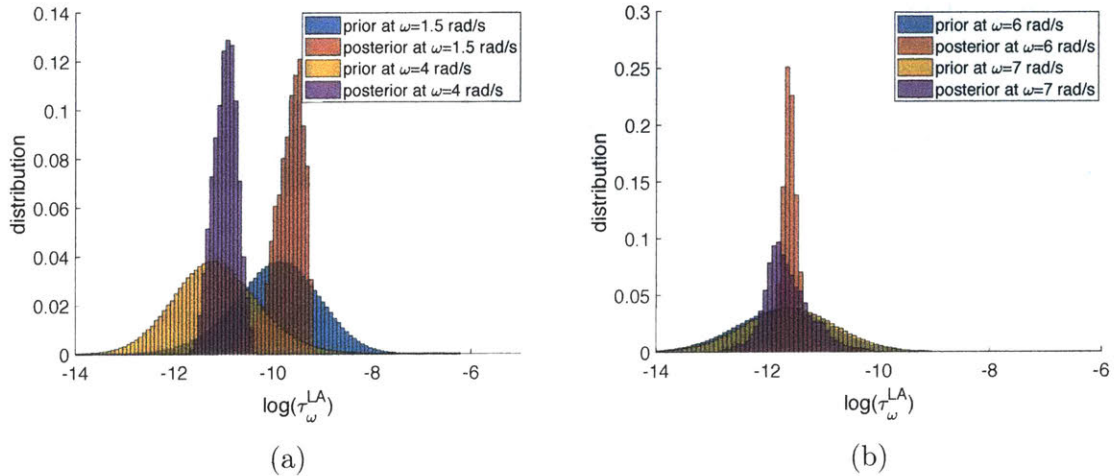


Figure 5-9: Distributions at a few low frequency (a) and high frequency (b) *LA* modes.

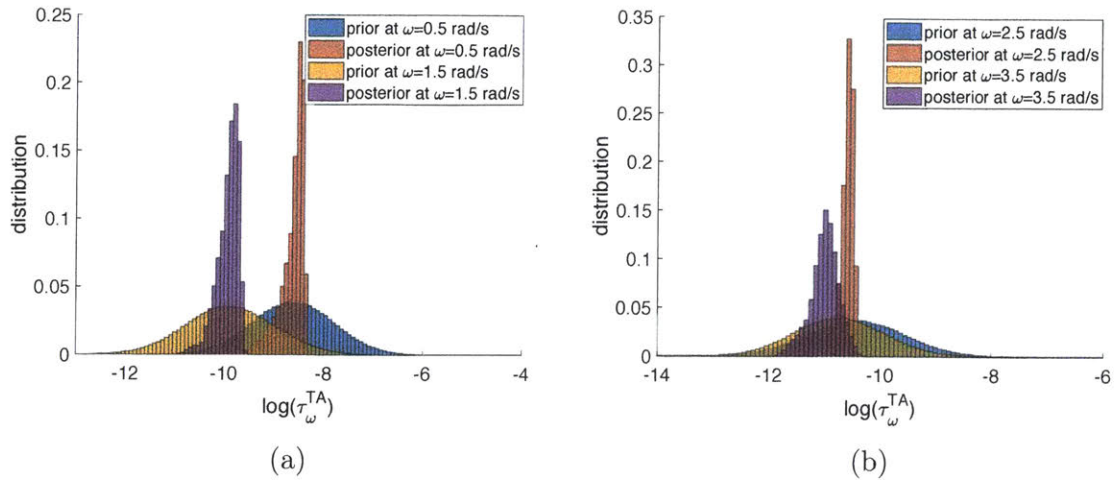


Figure 5-10: Distributions at a few low frequency (a) and high frequency (b)  $TA$  modes.

## 5.5 Probabilistic characterization of the optimization results

The optimization method proposed in this thesis operates in the presence of sources of randomness and uncertainty that can affect the final solution; the most important such sources are:

- repetition of the optimization process for multiple times using five different initial conditions in the first two stages of the graduated optimization process as well as (potentially) the choice of the segmentation point(s) of  $\tau_\omega^{TA}$  mode in the initial condition of the third stage
- noise in the temperature measurements,  $T_m$
- noise in the simulation of the forward problem

In this section, we study the effect of these sources of uncertainty on the optimization process for the same material properties (Si) and geometry (TTG) that we considered in section 5.4.

In this section we take a frequentist approach, that is, obtaining the distribution of the optimization output (relaxation time function) by observing its frequency (us-

ing many repetitions of the optimization process), whereas the analyses of section 5.4 have been focused on the reconstruction from a Bayesian perspective (updating a prior distribution based on the observations in order to obtain the posterior distribution). The analyses provided in sections 5.1 and 5.4 and their results complement the studies of the present section; if the particular functional form proposed in equation (2.7) would have resulted in a non-unique solution (contrary to the observation in section 5.1), regardless of the optimization algorithm that we use, there would not be any guarantee that the optimized solution is the correct solution (“true” solution); moreover, a wide posterior distribution of the relaxation times around the correct solution (contrary to the observation in section 5.4) would have implied low quality of the reconstruction (due to substantial sensitivity of relaxation times to measurement noise), regardless of the optimization algorithm.

Here, we assume that the measured temperatures,  $T_m$ , are generated from the actual (true) temperatures,  $T_t$ , plus a normally distributed noise, that is

$$T_m = T_t(t, \mathbf{x}; L) + \epsilon, \quad (5.19)$$

where  $\epsilon \sim \mathcal{N}(0, \sigma_m^2)$  and  $\sigma_m = 0.01$  K. Note that although the stochastic processes described in equations (5.13) and (5.19) are similar, the parameters/functions involved in the two equations are not the same. In other words, since in the Bayesian formulation we need to define the likelihood function ( $p(\{T_m(t, \mathbf{x} = 0; L)\}_{t,L} | \mathbf{U})$  term in equation (5.14)), we describe the measurement ( $T_m$ ) as a function of the unknown ( $\mathbf{U}$ ), as can be seen in equation (5.13), while when we perform direct sampling, such as the present section, we describe the measurement as a function of the actual (not directly observable) measurements ( $T_t$ ).

To simplify the representation of the probabilistic models used in this section, which are different for different stages of the optimization, we extend the notation for the unknown parameter  $\mathbf{U}$  introduced in Chapter 2 (equation (2.8)) to initial conditions at each stage. In particular, we denote the initial condition at stage  $i$  by

$\mathbf{Y}^i$ , namely,

$$\mathbf{Y}^1 = (\tau_{\omega_0}, \tau_{\omega_M}), \quad \mathbf{Y}^2 = (\boldsymbol{\tau}, \boldsymbol{\omega}), \quad \mathbf{Y}^3 = (\boldsymbol{\tau}^{LA}, \boldsymbol{\tau}^{TA}, \boldsymbol{\omega}^{LA}, \boldsymbol{\omega}^{TA}). \quad (5.20)$$

where, based on the framework discussed in Chapter 2 and [8],  $\mathbf{Y}^1 \in \mathbb{R}^2$ ,  $\mathbf{Y}^2 \in \mathbb{R}^6$ , and  $\mathbf{Y}^3 \in \mathbb{R}^{12}$ . Furthermore, we denote the optimization process by function  $\mathcal{F}$ , which maps the inputs to the solution,  $\mathbf{U} = \arg \min_{\mathbf{U}} \mathcal{L}$ , that is

$$\mathcal{F}(\mathbf{Y}_{1,2}^1, \mathbf{Y}_{5,6}^2, \mathbf{Y}_{11,12}^3, \{T_m(t, \mathbf{x} = 0; L)\}_{t,L}, \mathcal{N}_{\text{BTE}}^{1,2,3}) : \mathbb{R}^{N+6} \times \mathbb{N}^3 \rightarrow \mathbb{R}^{12} \quad (5.21)$$

in which  $\mathbf{Y}_j^i$  is the  $j$ -th component of the initial condition at stage  $i$ ,  $\{T_m(t, \mathbf{x} = 0; L)\}_{t,L}$ , as before, is the set of all temperature measurements, which has  $N$  elements ( $|\{T_m(t, \mathbf{x} = 0; L)\}_{t,L}| = N$ ), and  $\mathcal{N}_{\text{BTE}}^i \in \mathbb{N}$  is the number of particles used in the MC simulations of the BTE,  $T_{\text{BTE}}$ , at stage  $i$ . The function has  $N + 9$  inputs (the term  $\mathbb{R}^{N+6} \times \mathbb{N}^3$ ); in particular,  $\mathbb{R}^{N+6}$  corresponds to the  $N$  temperature measurements and the six initial conditions associated with the three stages of the optimization (as described below), while  $\mathbf{U} \in \mathbb{R}^{12}$  (the output) corresponds to the final solution of the optimization,  $\mathbf{U} = \arg \min_{\mathbf{U}} \mathcal{L}$ .

The reason for this specific choice of the independent variables in (5.21), as stated in the beginning of this section, is to study the effect of choice of initial conditions ( $\mathbf{Y}_{1,2}^1, \mathbf{Y}_{5,6}^2, \mathbf{Y}_{11,12}^3$ ), the noise in the measurements ( $\{T_m(t, \mathbf{x} = 0; L)\}_{t,L}$ ), and the noise in the simulation of the BTE ( $\mathcal{N}_{\text{BTE}}^{1,2,3}$ ). The input  $\mathbf{Y}_{1,2}^1$  in (5.21) represents the two initial relaxation time values,  $\tau_{\omega_0}$  and  $\tau_{\omega_M}$ , that parameterize the initial linear relaxation time function at the first stage;  $\mathbf{Y}_{5,6}^2$  represents the two frequencies (located on the line that the solution of the first stage has converged to) which correspond to the initial segmentation points for the three lines of the second stage; and  $\mathbf{Y}_{11,12}^3$  represents the two frequencies,  $\omega_1^{TA}$  and  $\omega_2^{TA}$ , which correspond to the initial segmentation points between the three lines of the third stage for  $TA$  modes. Note that the reason we do not have such inputs for the  $LA$  modes is that since  $\omega_0^{LA} = \omega_0$  and  $\omega_M^{LA} = \omega_M$  (the range of  $LA$  mode frequencies is the same as the

domain of all frequencies; see figure 5-8), we can initialize  $LA$  mode relaxation times at the third stage from the solution of the second stage; this is in contrast to the  $TA$  modes, for which  $\omega_{M^{TA}}^{TA} < \omega_M$ , and thus depending on the location of the segmentation points in the solution of the second stage, we may need to pick one or two new segmentation points in the range  $(\omega_0^{TA}, \omega_{M^{TA}}^{TA})$  to ensure the relaxation time function for  $TA$  modes has three lines, otherwise, two or four parameters in the relaxation time model of the  $TA$  modes will become redundant.

In analogy to definition (5.21), we denote the optimization algorithm in each stage  $i$  by function  $\mathcal{F}^i$ , where

$$\mathcal{F}^i(\mathbf{Y}^i, \{T_m(t, \mathbf{x} = 0; L)\}_{t,L}, \mathcal{N}_{\text{BTE}}^i) : \mathbb{R}^{N+r_i} \times \mathbb{N} \rightarrow \mathbb{R}^{r_i}, \quad i \in \{1, 2, 3\} \quad (5.22)$$

in which  $\mathbb{R}^N$  represents the  $N$  temperature measurements and based on the framework discussed in Chapter 2,  $r_1 = 2$ ,  $r_2 = 6$ , and  $r_3 = 12$  (the dimension of the unknown parameter at different stages).  $\mathcal{N}_{\text{BTE}}^i \in \mathbb{N}$ , as before, is the number of particles used in the MC simulations of the BTE at stage  $i$ .

Unlike the standard optimization process discussed in Chapter 2, where the output is a deterministic solution  $\mathbf{U}$ , here, we are interested in a probabilistic output where the uncertainty in both temperature measurements and stage-dependent initial conditions, in the presence and absence of noise in the BTE simulations, are considered. In particular, we perform three different studies of the distribution of  $\mathbf{U}$  (that is  $\mathbf{U} = \mathcal{F}(\mathbf{Y}_{1,2}^1, \mathbf{Y}_{5,6}^2, \mathbf{Y}_{11,12}^3, \{T_m(t, \mathbf{x} = 0; L)\}_{t,L}, \mathcal{N}_{\text{BTE}}^{1,2,3})$ ), which we will refer to as “case” —one, two, and three. First (case one), we only study the effect of choice of stage-dependent initial conditions,  $\mathbf{Y}_{1,2}^1$ ,  $\mathbf{Y}_{5,6}^2$ , and  $\mathbf{Y}_{11,12}^3$ . In this sampling process, it is assumed that  $T_m = T_t$  (noise-free measurements) and  $\mathcal{N}_{\text{BTE}} \rightarrow \infty$  (we use IFFT as discussed in section 5.4 to guarantee noise-free forward simulations). In the second case, we also incorporate the effect of noise in the temperature measurement, therefore,  $T_m = T_t + \epsilon$  (as described in equation (5.19)). Finally, case three includes the effect of noisy forward MC simulations as well in the optimization process, that is,  $\mathcal{N}_{\text{BTE}}$  is finite.

**Case one** In order to study the effect of choice of initial condition at the first stage, we sample the parameters of the initial condition from the following distribution

$$\mathbf{Y}_{1,2}^1 \sim U([-13, -4]^2) \quad (5.23)$$

where  $U([a, b]^n)$  represents generating  $n$  uniformly distributed random numbers in the range  $[a, b]$ . This choice of initial condition for the first stage leads to  $(\tau_{\omega_0}, \tau_{\omega_3}) \in [10^{-13}, 10^{-4}]^2$  which includes the set of all linear relaxation time functions that are bounded by 0.1 ps and 100  $\mu$ s, which is a conservative choice of the distribution of the initial condition.

The optimization result at the end of the first stage is in the form of a linear function, that is,  $\mathcal{F}^1 \in \mathbb{R}^2$ , while for the initial condition of the second stage we have  $\mathbf{Y}^2 \in \mathbb{R}^6$ , a piecewise linear function with three lines. Therefore, calculating  $\mathbf{Y}^2$  is equal to finding the two segmentation points that transform the line that the optimization at the first stage has converged to into the three lines that form the initial condition of stage two. There are different ways to chose the two initial segmentation points. Here, we generate two random numbers from two Gaussian distributions, one centered at the frequency  $\omega_0 + (\omega_M - \omega_0)/3$  and the other one at  $\omega_0 + 2(\omega_M - \omega_0)/3$ , where  $\omega_0$  and  $\omega_M$  are the smallest and largest frequencies considering all branches, respectively. Therefore,

$$\mathbf{Y}_5^2 \sim \mathcal{N}(\omega_0 + (\omega_M - \omega_0)/3, \sigma_\omega^2), \quad \mathbf{Y}_6^2 \sim \mathcal{N}(\omega_0 + 2(\omega_M - \omega_0)/3, \sigma_\omega^2). \quad (5.24)$$

Once  $\mathbf{Y}_{5,6}^2$  is sampled, we can determine other elements of  $\mathbf{Y}^2$  from

$$\begin{aligned} \mathbf{Y}_1^2 &= \mathcal{F}_1^1 \\ \mathbf{Y}_2^2 &= (\mathcal{F}_2^1 - \mathcal{F}_1^1) \log(\mathbf{Y}_5^2/\omega_0) / \log(\omega_M/\omega_0) + \mathcal{F}_1^1 \\ \mathbf{Y}_3^2 &= (\mathcal{F}_2^1 - \mathcal{F}_1^1) \log(\mathbf{Y}_6^2/\omega_0) / \log(\omega_M/\omega_0) + \mathcal{F}_1^1 \\ \mathbf{Y}_4^2 &= \mathcal{F}_2^1 \end{aligned} \quad (5.25)$$

where we used the notation  $\mathcal{F}^1 := \mathcal{F}^1(\mathbf{Y}^1, \{T_m(t, \mathbf{x} = 0; L)\}_{t,L}, \mathcal{N}_{\text{BTE}}^1)$  in RHS of (5.25) for compactness and  $\mathcal{F}_j^i$  is the  $j$ -th component of  $\mathcal{F}^i$ . Here we have used  $\sigma_\omega = 10^{13}$  rad/s.

The remaining initial condition in (5.21) is  $\mathbf{Y}_{11,12}^3$  which corresponds to generation of initial condition at the third stage from the optimization solution at the second stage. As explained previously, here we can initialize the  $LA$  mode relaxation times at the third stage from the solution of the second stage, while for the  $TA$  modes, since  $\omega_{M^{TA}}^{TA} < \omega_M$ , depending on the location of the segmentation points in the solution of the second stage, we may need to pick one or two new segmentation points in the range  $(\omega_0^{TA}, \omega_{M^{TA}}^{TA})$  to ensure the relaxation time function for  $TA$  modes is parameterized with three lines. Taking into account the location of the segmentation points at the end of the second stage, we have

$$\mathbf{Y}_{11}^3 \sim \begin{cases} \mathbf{1}_{\mathbf{Y}_{11}^3 = \mathcal{F}_5^2} & \mathcal{F}_6^2 < \omega_3^{TA} \text{ or } \{\mathcal{F}_5^2 < \frac{\omega_0 + \omega_3^{TA}}{2} \text{ and } \mathcal{F}_5^2 < \omega_3^{TA} < \mathcal{F}_6^2\} \\ \mathcal{N}(\omega_0 + \frac{\omega_3^{TA} - \omega_0}{3}, \sigma_\omega^2) & \omega_3^{TA} < \mathcal{F}_5^2 \text{ or } \{\frac{\omega_0 + \omega_3^{TA}}{2} < \mathcal{F}_5^2 \text{ and } \mathcal{F}_5^2 < \omega_3^{TA} < \mathcal{F}_6^2\} \end{cases} \quad (5.26)$$

and

$$\mathbf{Y}_{12}^3 \sim \begin{cases} \mathbf{1}_{\mathbf{Y}_{12}^3 = \mathcal{F}_6^2} & \mathcal{F}_6^2 < \omega_3^{TA} \\ \mathbf{1}_{\mathbf{Y}_{12}^3 = \mathcal{F}_5^2} & \frac{\omega_0 + \omega_3^{TA}}{2} < \mathcal{F}_5^2 \text{ and } \mathcal{F}_5^2 < \omega_3^{TA} < \mathcal{F}_6^2 \\ \mathcal{N}(\omega_0 + 2\frac{\omega_3^{TA} - \omega_0}{3}, \sigma_\omega^2) & \omega_3^{TA} < \mathcal{F}_5^2 \text{ or } \{\mathcal{F}_5^2 < \frac{\omega_0 + \omega_3^{TA}}{2} \text{ and } \mathcal{F}_5^2 < \omega_3^{TA} < \mathcal{F}_6^2\} \end{cases} \quad (5.27)$$

where we used the notation  $\mathcal{F}^2 := \mathcal{F}^2(\mathbf{Y}^2, \{T_m(t, \mathbf{x} = 0; L)\}_{t,L}, \mathcal{N}_{\text{BTE}}^2)$  in RHS of (5.26) and (5.27) for compactness. The distributions used in (5.26) and (5.27) are similar to the distribution that were proposed in (5.24), except, one, here the domain of the two segmentation points is  $[\omega_0, \omega_3^{TA}]$  instead of  $[\omega_0, \omega_3]$ , and two, depending on the solution of the optimization at the end of the second stage, we might need to only sample one or zero segmentation points at the initialization of stage three, with other point(s) being determined from the solution of the second stage without any new sampling process. In cases we only need to sample one new segmentation point, we generate that point from a Gaussian distribution either centered at  $\omega_0 + (\omega_3^{TA} - \omega_0)/3$

or  $\omega_0 + 2(\omega_3^{TA} - \omega_0)/3$ , whichever is farthest from the location of the other segmentation point (the one that is in the  $[\omega_0, \omega_3^{TA}]$  range from the solution of the second stage).

Once  $\mathbf{Y}_{11,12}^3$  is sampled, we can determine other elements of  $\mathbf{Y}^3$  from

$$\mathbf{Y}_i^3 = \mathcal{F}_i^2, \quad i \in \{1, 2, 3, 4\}$$

$$\mathbf{Y}_i^3 = \mathcal{F}_{i-4}^2, \quad i \in \{5, 9, 10\}$$

$$\mathbf{Y}_6^3 = \begin{cases} \mathcal{F}_2^2 & \mathcal{F}_6^2 < \omega_3^{TA} \text{ or } \{\mathcal{F}_5^2 < \frac{\omega_0 + \omega_3^{TA}}{2} \text{ and } \mathcal{F}_5^2 < \omega_3^{TA} < \mathcal{F}_6^2\} \\ (\mathcal{F}_2^2 - \mathcal{F}_1^2) \frac{\log\left(\frac{\mathbf{Y}_{11}^3}{\omega_0}\right)}{\log\left(\frac{\mathcal{F}_2^2}{\omega_0}\right)} + \mathcal{F}_1^2 & \omega_3^{TA} < \mathcal{F}_5^2 \text{ or } \{\frac{\omega_0 + \omega_3^{TA}}{2} < \mathcal{F}_5^2 \text{ and } \mathcal{F}_5^2 < \omega_3^{TA} < \mathcal{F}_6^2\} \end{cases}$$

$$\mathbf{Y}_7^3 = \begin{cases} \mathcal{F}_3^2 & \mathcal{F}_6^2 < \omega_3^{TA} \\ \mathcal{F}_2^2 & \frac{\omega_0 + \omega_3^{TA}}{2} < \mathcal{F}_5^2 \text{ and } \mathcal{F}_5^2 < \omega_3^{TA} < \mathcal{F}_6^2 \\ (\mathcal{F}_3^2 - \mathcal{F}_2^2) \frac{\log(\mathbf{Y}_{12}^3/\mathcal{F}_5^2)}{\log(\mathcal{F}_6^2/\mathcal{F}_5^2)} + \mathcal{F}_2^2 & \mathcal{F}_5^2 < \frac{\omega_0 + \omega_3^{TA}}{2} \text{ and } \mathcal{F}_5^2 < \omega_3^{TA} < \mathcal{F}_6^2 \\ (\mathcal{F}_2^2 - \mathcal{F}_1^2) \frac{\log(\mathbf{Y}_{12}^3/\omega_0)}{\log(\mathcal{F}_5^2/\omega_0)} + \mathcal{F}_1^2 & \omega_3^{TA} < \mathcal{F}_5^2 \end{cases}$$

$$\mathbf{Y}_8^3 = \begin{cases} \mathcal{F}_4^2 & \mathcal{F}_6^2 < \omega_3^{TA} \\ (\mathcal{F}_3^2 - \mathcal{F}_2^2) \frac{\log(\omega_3^{TA}/\mathcal{F}_2^2)}{\log(\mathcal{F}_6^2/\mathcal{F}_5^2)} + \mathcal{F}_2^2 & \mathcal{F}_5^2 < \omega_3^{TA} < \mathcal{F}_6^2 \\ (\mathcal{F}_2^2 - \mathcal{F}_1^2) \frac{\log(\omega_3^{TA}/\omega_0)}{\log(\mathcal{F}_5^2/\omega_0)} + \mathcal{F}_1^2 & \omega_3^{TA} < \mathcal{F}_5^2 \end{cases} \quad (5.28)$$

Based on the process described in (5.23)–(5.28), we can use Algorithm 2 to sample the distribution of  $\mathcal{F}$  in the absence of the measurement noise and the noise of the forward simulation. The distribution of the relaxation time function at the end of the sampling process,  $p(\mathbf{U})$ , is plotted in figure 5-11. We observe that, in general, the solutions are distributed around the exact (input) function with a small variance, implying that the solution of the multi-stage optimization process is quite robust to the choice of the initial conditions at different stages of the optimization. The uncertainty in the *LA* modes at high frequencies is more significant than other frequencies, in agreement with our observations in the Bayesian approach. However, one difference between the distribution in those frequencies ( $\omega \gtrsim 6.5 \times 10^{13}$  rad/s) in figure 5-11 compared to figure 5-8 is that, while the distribution in both figures in that frequency range is the widest, the distribution in figure 5-11 is more biased toward relaxation times that are smaller than the true relaxation times. This is likely due to the fact that in the

---

**Algorithm 2** Sampling  $p(\mathbf{U})$ ; noise-free measurements and forward simulations

---

**Require:** measurements:  $\{T_m(t, \mathbf{x} = 0; L)\}_{t,L}$ ; the three-stage optimization algorithm:  $\mathcal{F}^{1,2,3}$  functions; number of sample points:  $N_{\text{NM}}$

**for**  $k = 1$  to  $k = N_{\text{NM}}$  **do**

    generate  $\mathbf{Y}^1 \sim U([-13, -4]^2)$

    run first-stage optimization algorithm  $\mathcal{F}^1(\mathbf{Y}^1, \{T_m(t, \mathbf{x} = 0; L)\}_{t,L}, \infty)$

    generate  $\mathbf{Y}_{5,6}^2$  from equation (5.24)

    calculate  $\mathbf{Y}_{1,\dots,4}^2$  from equation (5.25)

    run second-stage optimization algorithm  $\mathcal{F}^2(\mathbf{Y}^2, \{T_m(t, \mathbf{x} = 0; L)\}_{t,L}, \infty)$

    generate  $\mathbf{Y}_{11,12}^3$  from equations (5.26)–(5.27)

    calculate  $\mathbf{Y}_{1,\dots,10}^3$  from equation (5.28)

    run third-stage optimization algorithm  $\mathcal{F}^3(\mathbf{Y}^3, \{T_m(t, \mathbf{x} = 0; L)\}_{t,L}, \infty)$

    set  $\mathbf{U}_k^{\text{NM}} \leftarrow \mathcal{F}^3(\mathbf{Y}^3, \{T_m(t, \mathbf{x} = 0; L)\}_{t,L}, \infty)$

**end for**

**return**  $p(\mathbf{U}) \leftarrow \frac{1}{N_{\text{NM}}} \sum_{k=1}^{N_{\text{NM}}} \mathbb{1}_{\mathbf{U}=\mathbf{U}_k^{\text{NM}}}$

---

multi-stage optimization process (which figure 5-11 is generated from), the first stage starts with a linear model of the relaxation times function and consequently, for the frequency ranges whose relaxation times have less influence on the thermal behavior, the algorithm may be biased toward the linear function that the optimization at the first stage has converged to (due to dependence of the initial condition at the second and third stages to the solution at the first and second stages, respectively). Another difference between the two figures is the better prediction of relaxation times at small frequencies in figure 5-11. This is likely a consequence of incorporating the value of heat conductivity into the multi-stage optimization process (the second term in (2.9)), since the free path at those frequencies is larger than other frequencies — note that the free path values directly influence the value of the heat conductivity.

**Case two** In this case we add the uncertainty in the temperature profile measurements. In other words, the only difference compared to case one is that the input temperatures are sampled based on (5.19), assuming  $\sigma_m = 0.01$  K. Algorithm 3 describes this sampling process.

The distribution of the relaxation time function at the end of the sampling,  $p(\mathbf{U})$ , for case two is plotted in figure 5-12. The behavior is similar to that of figure 5-11 with a slightly larger variance (due to noise in the measurement). The same conclusions

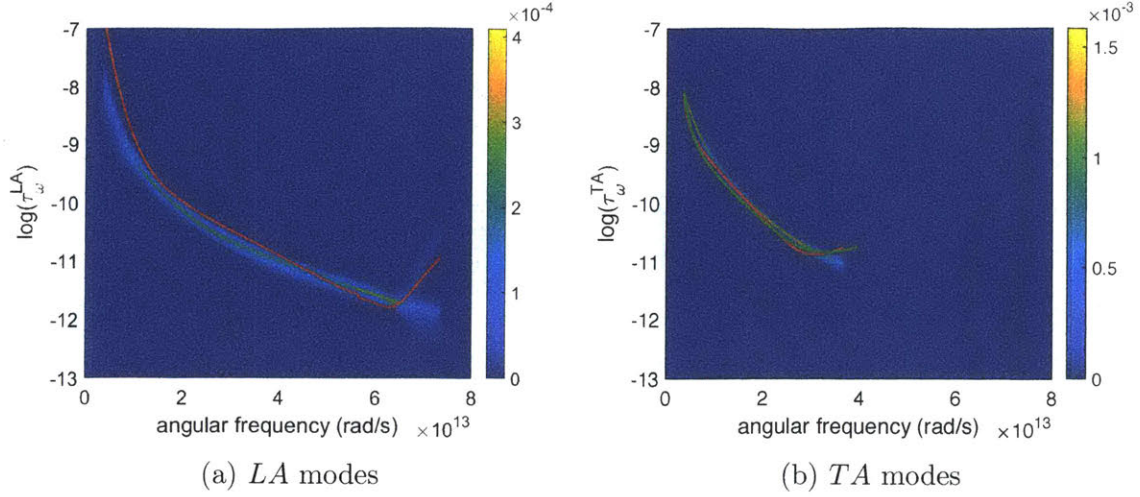


Figure 5-11: Frequency-dependent relaxation time distribution of *LA* and *TA* modes for the noise-free measurements and forward simulations. The red line in (a) denotes the true  $\tau_\omega^{LA}$  while the red line in (b) denotes the true  $\tau_\omega^{TA1}$  and the green line in (b) denotes the true  $\tau_\omega^{TA2}$ .

---

**Algorithm 3** Sampling  $p(\mathbf{U})$ ; noisy measurements and noise-free forward simulations

---

**Require:** measurements:  $\{T_m(t, \mathbf{x} = 0; L)\}_{t,L}$ ; the three-stage optimization algorithm:  $\mathcal{F}^{1,2,3}$  functions; number of sample points:  $N_{\text{NM}}$

**for**  $k = 1$  to  $k = N_{\text{NM}}$  **do**  
  generate  $\forall(t, L) : T_t(t, \mathbf{x} = 0; L) \sim \mathcal{N}(T_m(t, \mathbf{x} = 0; L), \sigma_m^2)$   
  generate  $\mathbf{Y}^1 \sim U([-13, -4]^2)$   
  run first-stage optimization algorithm  $\mathcal{F}^1(\mathbf{Y}^1, \{T_t(t, \mathbf{x} = 0; L)\}_{t,L}, \infty)$   
  generate  $\mathbf{Y}_{5,6}^2$  from equation (5.24)  
  calculate  $\mathbf{Y}_{1,\dots,4}^2$  from equation (5.25)  
  run second-stage optimization algorithm  $\mathcal{F}^2(\mathbf{Y}^2, \{T_t(t, \mathbf{x} = 0; L)\}_{t,L}, \infty)$   
  generate  $\mathbf{Y}_{11,12}^3$  from equations (5.26)–(5.27)  
  calculate  $\mathbf{Y}_{1,\dots,10}^3$  from equation (5.28)  
  run third-stage optimization algorithm  $\mathcal{F}^3(\mathbf{Y}^3, \{T_t(t, \mathbf{x} = 0; L)\}_{t,L}, \infty)$   
  set  $\mathbf{U}_k^{\text{NM}} \leftarrow \mathcal{F}^3(\mathbf{Y}^3, \{T_t(t, \mathbf{x} = 0; L)\}_{t,L}, \infty)$   
**end for**  
**return**  $p(\mathbf{U}) \leftarrow \frac{1}{N_{\text{NM}}} \sum_{k=1}^{N_{\text{NM}}} \mathbb{1}_{\mathbf{U}=\mathbf{U}_k^{\text{NM}}}$

---

about the distribution at different frequencies are also valid here.

**Case three** The sampling in this case is similar to case two, except that MC simulation is being used for forward BTE solutions, and, as a consequence,  $\mathcal{N}_{\text{BTE}}^i$  is finite. In particular,  $\mathcal{N}_{\text{BTE}}^1 = \mathcal{N}_{\text{BTE}}^2 = 10^4$  while  $\mathcal{N}_{\text{BTE}}^3 = 10^5$ . Note that due to the high computational cost of the sampling in this case, we have used a smaller number of

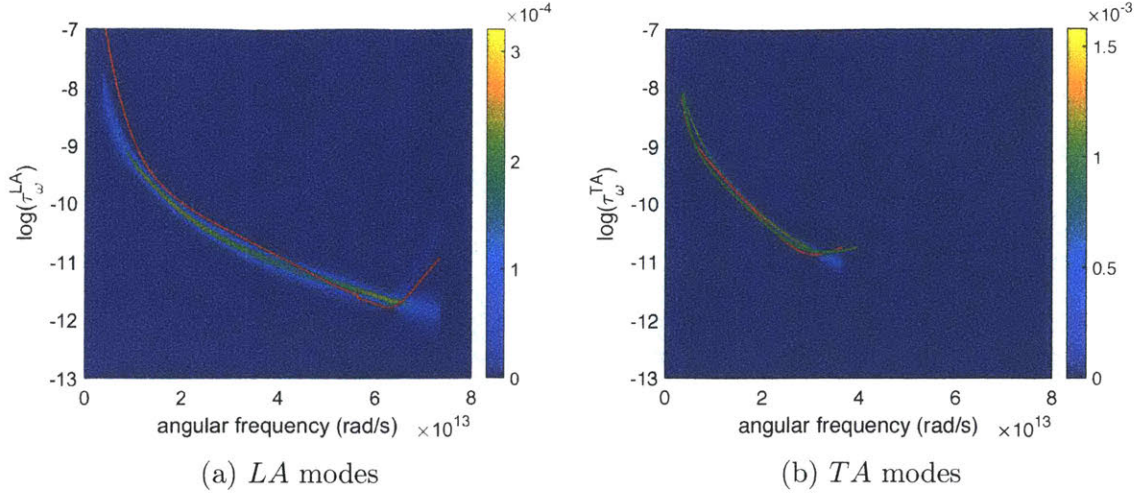


Figure 5-12: Frequency-dependent relaxation time distribution of  $LA$  and  $TA$  modes for the noisy measurements and noise-free forward simulations. The red line in (a) denotes the true  $\tau_{\omega}^{LA}$  while the red line in (b) denotes the true  $\tau_{\omega}^{TA1}$  and the green line in (b) denotes the true  $\tau_{\omega}^{TA2}$ .

particles in the third stage compared to Chapters 2 and 3, where we have used  $10^6$ . Therefore, the reconstruction of the relaxation times in the presence of noisy forward simulation, as studied in Chapter 2, is expected to be slightly more accurate than the result presented here. Algorithm 4 is used to sample the distribution of  $\mathbf{U}$  in this case.

---

**Algorithm 4** Sampling  $p(\mathbf{U})$ ; noisy measurements and noisy forward simulations

---

**Require:** measurements:  $\{T_m(t, \mathbf{x} = 0; L)\}_{t,L}$ ; the three-stage optimization algorithm:  $\mathcal{F}^{1,2,3}$  functions; number of sample points:  $N_{\text{NM}}$ ; number of stage-dependent MC simulations particles:  $\mathcal{N}_{\text{BTE}}^i$

**for**  $k = 1$  to  $k = N_{\text{NM}}$  **do**

generate  $\forall(t, L) : T_t(t, \mathbf{x} = 0; L) \sim \mathcal{N}(T_m(t, \mathbf{x} = 0; L), \sigma_m^2)$

generate  $\mathbf{Y}^1 \sim U([-13, -4]^2)$

run first-stage optimization algorithm  $\mathcal{F}^1(\mathbf{Y}^1, \{T_t(t, \mathbf{x} = 0; L)\}_{t,L}, 10^4)$

generate  $\mathbf{Y}_{5,6}^2$  from equation (5.24)

calculate  $\mathbf{Y}_{1,\dots,4}^2$  from equation (5.25)

run second-stage optimization algorithm  $\mathcal{F}^2(\mathbf{Y}^2, \{T_t(t, \mathbf{x} = 0; L)\}_{t,L}, 10^4)$

generate  $\mathbf{Y}_{11,12}^3$  from equations (5.26)–(5.27)

calculate  $\mathbf{Y}_{1,\dots,10}^3$  from equation (5.28)

run third-stage optimization algorithm  $\mathcal{F}^3(\mathbf{Y}^3, \{T_t(t, \mathbf{x} = 0; L)\}_{t,L}, 10^5)$

set  $\mathbf{U}_k^{\text{NM}} \leftarrow \mathcal{F}^3(\mathbf{Y}^3, \{T_t(t, \mathbf{x} = 0; L)\}_{t,L}, 10^5)$

**end for**

**return**  $p(\mathbf{U}) \leftarrow \frac{1}{N_{\text{NM}}} \sum_{k=1}^{N_{\text{NM}}} \mathbf{1}_{\mathbf{U}=\mathbf{U}_k^{\text{NM}}}$

---

Figure 5-13 shows  $p(\mathbf{U})$  for case three. The distributions are similar to those of case two, implying that using MC simulations for forward simulations did not degrade the quality of the reconstruction.

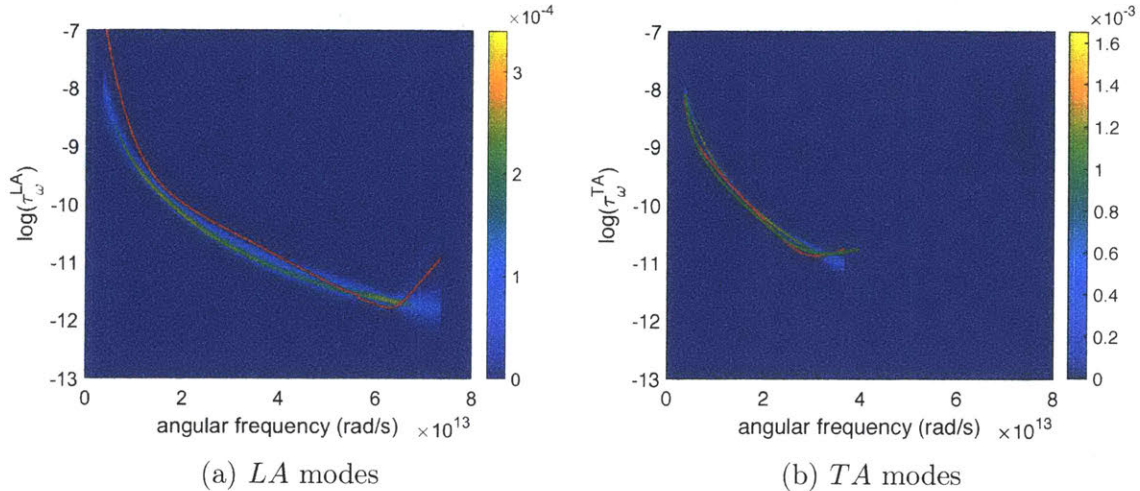


Figure 5-13: Frequency-dependent relaxation time distribution of  $LA$  and  $TA$  modes for the noisy measurements and forward simulations. The red line in (a) denotes the true  $\tau_{\omega}^{LA}$  while the red line in (b) denotes the true  $\tau_{\omega}^{TA1}$  and the green line in (b) denotes the true  $\tau_{\omega}^{TA2}$ .

The initial distribution,  $\mathbf{Y}^1$ , and the distribution at the end of the first stage in case three,  $\mathcal{F}^1$ , are plotted in figure 5-14. The components of  $\mathbf{Y}^1$  are both uniformly distributed between  $-13$  and  $-4$ , as expected from Algorithm 4. However, an important observation in figure 5-14 is that almost all  $\mathcal{F}^1$  samples are located at a point close to  $(-8, -12)$  (the point in the middle of the red circle). This is an important result since it implies that the behavior of the objective function at the first stage, even in the presence of noise in the temperature measurements and the forward simulations, resembles that of a convex function, which is one of the goals in the graduated optimization process (ensuring that the behavior at initial stages is close to a convex optimization) [59]. Furthermore, this shows that the specific choice of the five initial conditions proposed at the beginning of the first stage is not expected to have a significant effect on what its solution converges to.

We have plotted the distribution at the end of the first stage,  $\mathcal{F}^1$ , for all three cases, in figure 5-15. Figure 5-15a corresponds to case one, 5-15b corresponds to

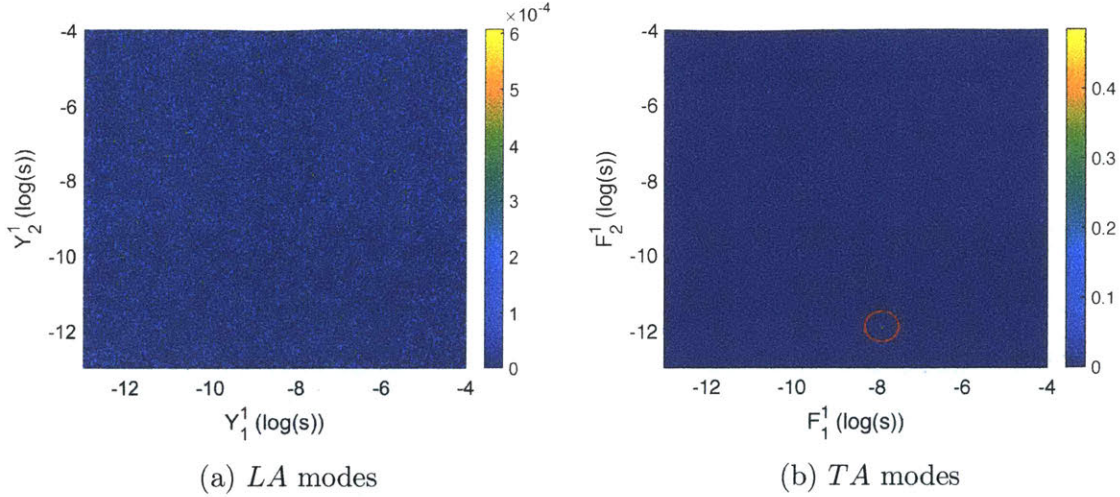


Figure 5-14: Distributions of  $\mathbf{Y}^1$  and  $\mathcal{F}^1$  for the noisy measurements and noisy forward simulations. The point in the middle of the red circle shows where the result has converged to.

case two, and 5-15c corresponds to case three (a magnified version of 5-14b) — note the small range of values over which the distribution is plotted. The conclusion for case one and two are similar to that of case three, as explained previously, that is, the objective function at the first stage is essentially a convex function. Due to small number of unknowns ( $\dim(\mathcal{F}^1) = 2$ ) figure 5-15 provides a simple and useful visualization of the effect of noise in the measurement and forward simulations on the uncertainty in reconstructing the unknown parameters<sup>2</sup>. In particular, these figures provide an “estimation” of the sensitivity of the relaxation time at small frequencies (since  $\mathcal{F}_1^1 = \tau_{\omega_0}$ ) and large frequencies (since  $\mathcal{F}_2^1 = \tau_{\omega_M}$ ) on the noise in the measurement and forward simulations, and, as expected, the uncertainty in case three is more than case two and in case two is more than case one. The small variance observed (in figure 5-15c) — note the small range of values over which the distribution is plotted — from the correct solution (the point in figure 5-15a), implies that the noise in the measurement and forward simulations does not have a significant impact on the quality of the reconstruction. This also justifies the similarities between the

<sup>2</sup>This is in comparison to, for instance, the results provided in figures 5-6 and 5-7, which due to large number of unknowns ( $\dim(\mathbf{U}) = 12$ ) plotting a simple pairwise joint distribution such as in figure 5-15, which relates different sources of noise to the reconstruction of the unknown, is not possible.

distributions observed in figures 5-11–5-13, despite the existence of multiple sources of uncertainties. Note also that the result in figure 5-15c corresponds to stage one of the optimization which uses  $10^4$  particles in the MC simulation; the simulations in the third stage of the optimization, presented in Chapters 2 and 3, are expected to have a significantly smaller variance due to larger number of computational particles in the MC simulations.

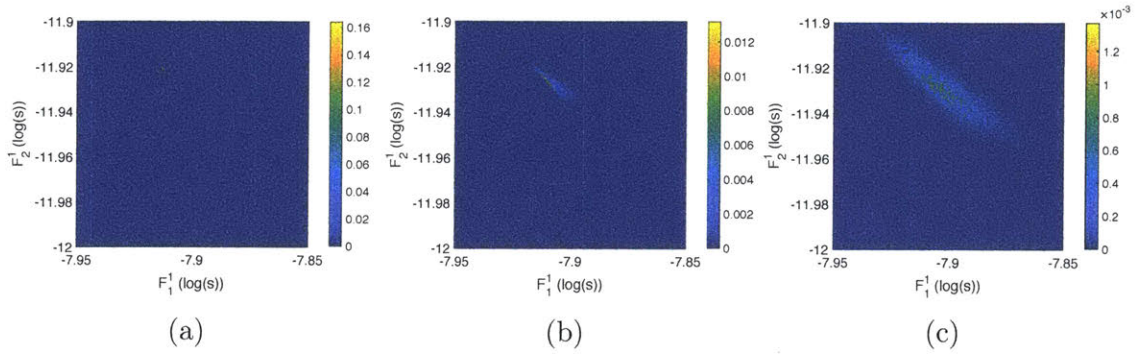


Figure 5-15: Distribution of  $\mathcal{F}^1$  for all three cases.



# Chapter 6

## Summary and outlook

In this thesis, we have proposed an alternative approach to phonon relaxation time and free path reconstruction that avoids the limitations associated with the effective thermal conductivity approach. The proposed method assumes knowledge of the phonon group velocities and poses the reconstruction as an optimization problem seeking the function  $\tau_\omega$  that minimizes the discrepancy between the observed experimental data and the solution of the BTE as applied to the experimental process. Although much research and improvements remain to be made, one of the main contributions of the present work is to show that reconstruction based on a more rigorous foundation (which does not make use of the assumption of Fourier behavior) is possible. Furthermore, the proposed formulation is sufficiently general to accept solutions of the BTE obtained by any means.

The optimization process is achieved by the Nelder-Mead algorithm that does not require gradient calculation and is thus robust to noise. Our results verify that reconstruction is robust both in the presence of noise in the input (experimental) data and the BTE solutions when the latter are obtained by MC simulation. Although MC simulations are considerably more expensive, they are, in fact, the more relevant to applications of practical interest (e.g., 2D-TTG [10] or 2D-dots [19]) which are in general high-dimensional and not expected to lend themselves to analytical solutions. The cost of MC simulations is partially mitigated by their excellent parallel efficiency. Moreover, in cases where the experimental measurement is limited to one

(or a few) discrete spatial locations, the MC simulation cost can be made independent of dimensionality using techniques such as adjoint formulations.

By using randomly chosen starting points, our validation tests subjected the optimization process to a worst-case scenario, since in most cases *a priori* information on the nature of the solution is expected to exist. In the present case, the lack of prior information was overcome by starting the optimization process, as a first stage, from a sweep of different initial conditions and choosing the result with the lowest objective function value as the initial condition for a second optimization stage. In the case of MC simulations, this approach was possible due to the robustness of the NM algorithm to noise, which enabled us to perform the first two stages of calculations using very cheap (noisy) simulations. In general, *a priori* information could be very useful in ensuring convergence to the correct solution, which due to the non-convex nature of the minimization problem is expected to be very challenging. Encouragingly, we were able to show (see Chapter 5) that despite its non-convex nature, the minimization problem is quite “well behaved”: for example, in addition to having a solution that appears to possess a global minimum, the value of the objective function as a function of its argument ( $\mathbf{U}$ ) can be reliably used as a measure of the distance between that input and the solution—a small value of the objective function implies being in the vicinity of the correct solution. Future research will focus on formulations which exploit *a priori* information on the nature of the solution, such as generalizing the uniqueness properties studied in Chapter 5 for the TTG, to general geometrical setups, as well as alternative optimization algorithms to improve convergence rates and accuracy, such as use of machine learning algorithms or MCMC (Markov chain Monte Carlo) with local approximations [72].

Our results also show that the reconstruction process is very robust with respect to the time window over which the material response is observed, in contrast to Fourier-based approaches which assume a late-time response. More specifically, by matching the material response to BTE solutions, the reconstruction is successful with response data limited to very early times (e.g. on the order of 5 nanoseconds) that are typical in pump-probe experiments [19] but do not satisfy assumptions required for diffusive

behavior to set in.

Utilizing an analytical solution of the BTE for the TTG response, we have shown in Chapter 2 that, as expected, reconstruction using the effective thermal conductivity concept is limited to late times (compared to the mean free time) and large lengthscales (compared to the mean free path) ( $\text{Kn}^2 \ll 1$  for the TTG in particular). Using input data that does not satisfy these requirements will lead to reconstruction error; on the other hand, using data in a limited range of characteristic lengthscales also leads to reconstruction error [13]. Furthermore, the analyses of sections 5.2 and 5.3 show that even if these requirements are met (late time and large free path), the free path cannot be used to predict a system’s thermal response, or in other words, **the free path distribution is not a material property**, because a given free path distribution does not uniquely define the relaxation time function of the system.

In Chapter 3, we have extended our optimization formulation to the reconstruction of the relaxation times and free paths from thermal spectroscopy data in the presence of a solid-solid interface. The reconstruction is achieved by comparing the experimental output with simulations of the BTE, thus avoiding the use of a Fourier assumption or related approximations. Our results show that, perhaps surprisingly, the relaxation times can be fully resolved, even if the interface transmissivities are not. This observation is particularly significant for applications where reconstruction of relaxation times is the primary objective, because it implies that various reconstructions previously thought intractable are, in fact, feasible. Although our work has focused on a particular experimental setup (2D-dots), we believe that our conclusions are valid for other experiments in similar transport regimes.

We also note that although for all successful reconstructions shown in Chapter 3, the interface conductance ( $G$ ) was reproduced to a good approximation level, this does not imply that an approximately correct value of  $G$  is a sufficient condition for correct reconstruction of relaxation times. In fact, numerical experiments show that simple frequency-independent parametrizations of transmissivities that capture the correct value of  $G$  (approximately) but do not reconstruct the relaxation times or predict the thermal behavior correctly are possible. In other words, the “aggregate effect” of

the interface that needs to be captured extends beyond its (continuum) conductance value. As always, the ultimate gauge of the success (reliability) of the reconstruction is its ability to reproduce the experimental (input) temperature relaxation profiles, measured either via a comparison such as that of figure 3-10, or via the final value of the objective function.

Complete reconstructions such as the one shown in figure 3-2 take  $O(50)$  hours on a very modest quad core workstation (8 threads on an Intel i7-2600 @ 3.4GHz). In other words, although not cheap, they are certainly feasible, even without powerful computational resources. Owing to the perfect parallel scaling of the kinetic-type MC method [30] used here, wall time can be reduced significantly if multi-CPU parallel computing is utilized. Moreover, the above cost can be significantly reduced by exploiting the robustness of the NM method to noisy inputs, for example, by reducing the number of particles used for the Boltzmann solutions. Although normally the convergence rate of MC simulations is viewed as a poor feature of the method, in this case it can be turned into an advantage by noticing that a reduction of  $\mathcal{N}_{\text{BTE}}$  by an order of magnitude, resulting in proportionally the same reduction in cost, will only lead to an increase in stochastic error of only  $O(3)$  and thus will have only a small effect on the final result accuracy (see figure 2-3). Such, as well as other approaches for reducing the cost of reconstruction will be fully explored in the near future.

The approach proposed in Chapter 3 has a number of advantages compared to the effective thermal conductivity (or effective thermal diffusivity) approach. While effective thermal conductivity techniques require the value of the interface thermal conductance as an input to the Fourier heat equation, our algorithm does not make any assumption on that. This not only requires less knowledge of the problem under consideration, it also makes the reconstruction process less susceptible to error. We also recall that, as shown in Chapter 2 and [8], for an accurate reconstruction of the full spectrum of free paths (and relaxation times) the method proposed here does not require the availability of measurements in all transport regimes, while this is a requirement in the effective-heat-conductivity-based approaches. This requirement is particularly problematic in the 2D-dots experiment where regardless of the value of

the chosen length scale  $L$ , the regime is never diffusive, as discussed in section 3.3.5.

We have validated our reconstruction in the presence of an interface using numerical experiments based on the 2D-dots geometry [19] due to its relevance to the current state of the art. In concert with the experimental process, the metal dot height has been assumed constant (100 nm) [35]. However, as discussed in section 3.3.4, our results suggest that the fixed dot height limits the amount of information that can be extracted for the purpose of reconstructing the interface properties. The results presented in figure 3-12 indicate that more accurate characterization of interface transmissivities is possible if information from (numerical) experiments with variable dot heights is used. In the future, we plan to study the role that different metal film heights and geometrical setups play in the reconstruction of interface properties, as well as more generally search for approaches which amplify the sensitivity of reconstruction process to transmissivities, leading to more accurate prediction of the latter.

In Chapter 4, we have shown that the framework proposed in Chapter 2 and [8] can be reliably used to reconstruct from experimental data, where non-idealities (e.g. noise or other spurious signals), as well as modeling discrepancies (e.g. boundary effects) make reconstruction challenging. In the case of silicon studied here, the reconstructed results were found to be in good overall agreement with DFT results. Small discrepancies were shown to be primarily due to the inability of DFT to precisely capture the experimental material behavior, most likely due to effects present in the experiment not captured by the idealized material studied within the DFT model. The sensitivity analysis detailed in this chapter provides a tool for *a posteriori* identification of elements of  $\mathbf{U}$  to which the objective function is relatively insensitive and which, as a result, may not be accurately determined. These considerations make reconstruction methodologies uniquely positioned as a reliable complement to DFT calculations.

Our results in Chapter 5 show that the proposed algorithm can be reliably used for future reconstruction purposes on real experimental data which may include noise in their measurements, with no concerns about the nonuniqueness of the solution or

low sensitivity of the relaxation time function to the measured thermal responses, specifically in the absence of solid-solid interfaces (the case considered in that chapter). Finally, the probabilistic approaches presented in sections 5.4 and 5.5, although computationally more expensive than the multi-stage optimization used in Chapters 2–4, can be used to study the sensitivity of relaxation time at different frequencies to the optimization parameters, as well as noise in both the input data and the forward (MC) simulations.

# Appendix A

## Parameters of piece-wise linear model for relaxation time

Relationship (2.7) is constructed such that the intersections of the piecewise linear segments at  $\omega_j^S$ ,  $j = 1, \dots, M^S - 1$ , are smoothed by third-order polynomial functions. Each smoothing polynomial extends over a frequency range of  $2\Delta$ , centered on  $\omega_j^S$  and denoted by  $(X_{2j-1}^S, X_{2j}^S)$ , where

$$\begin{aligned} X_0^S &= \omega_0^S \\ X_{2j}^S &= \omega_j^S + \Delta, \quad X_{2j-1}^S = \omega_j^S - \Delta, \quad j \in \{1, \dots, M^S - 1\} \\ X_{2M^S-1}^S &= \omega_{M^S}^S \end{aligned} \tag{A.1}$$

In this work, we have used  $\Delta = 5 \times 10^{12}$  rad/s.

The coefficients  $a_j^S$ ,  $b_j^S$ ,  $c_j^S$ , and  $d_j^S$  are calculated from the following equations

$$\begin{aligned}
a_j^S &= -\frac{\log\left(1 - \left(\frac{\Delta}{\omega_j^S}\right)^2\right)}{\left[\log\left(\frac{\omega_j^S + \Delta}{\omega_j^S - \Delta}\right)\right]^3} \left[ \frac{\log\left(\frac{\tau_{\omega_{j+1}}^S}{\tau_{\omega_j}^S}\right)}{\log\left(\frac{\omega_{j+1}^S}{\omega_j^S}\right)} - \frac{\log\left(\frac{\tau_{\omega_j}^S}{\tau_{\omega_{j-1}}^S}\right)}{\log\left(\frac{\omega_j^S}{\omega_{j-1}^S}\right)} \right], \\
b_j^S &= 0.5 \left\{ \frac{1}{\log\left(\frac{\omega_j^S + \Delta}{\omega_j^S - \Delta}\right)} \left[ \frac{\log\left(\frac{\tau_{\omega_{j+1}}^S}{\tau_{\omega_j}^S}\right)}{\log\left(\frac{\omega_{j+1}^S}{\omega_j^S}\right)} - \frac{\log\left(\frac{\tau_{\omega_j}^S}{\tau_{\omega_{j-1}}^S}\right)}{\log\left(\frac{\omega_j^S}{\omega_{j-1}^S}\right)} \right] - 3a_j^S \log\left((\omega_j^S)^2 - \Delta^2\right) \right\}, \\
c_j^S &= \frac{\log\left(\frac{\tau_{\omega_j}^S}{\tau_{\omega_{j-1}}^S}\right)}{\log\left(\frac{\omega_j^S}{\omega_{j-1}^S}\right)} - 3a_j^S [\log(\omega_j^S - \Delta)]^2 - 2b_j^S \log(\omega_j^S - \Delta), \\
d_j^S &= \log(\tau_{\omega_{j-1}}^S) - \log(\omega_{j-1}^S) \frac{\log\left(\frac{\tau_{\omega_j}^S}{\tau_{\omega_{j-1}}^S}\right)}{\log\left(\frac{\omega_j^S}{\omega_{j-1}^S}\right)} + \\
&\quad 0.5 \frac{[\log(\omega_j^S - \Delta)]^2}{\log\left(\frac{\omega_j^S + \Delta}{\omega_j^S - \Delta}\right)} \left[ \frac{\log\left(\frac{\tau_{\omega_{j+1}}^S}{\tau_{\omega_j}^S}\right)}{\log\left(\frac{\omega_{j+1}^S}{\omega_j^S}\right)} - \frac{\log\left(\frac{\tau_{\omega_j}^S}{\tau_{\omega_{j-1}}^S}\right)}{\log\left(\frac{\omega_j^S}{\omega_{j-1}^S}\right)} \right] - \\
&\quad 0.5a_j^S [\log(\omega_j^S - \Delta)]^2 [3\log(\omega_j^S + \Delta) - \log(\omega_j^S - \Delta)], \tag{A.2}
\end{aligned}$$

where  $j \in \{1, \dots, M^S - 1\}$  and  $S \in \{LA, TA_1, TA_2\}$ .

# Appendix B

## Semi-analytical solution for the transient thermal grating

Here, we derive the semi-analytical frequency-domain solution (2.11) used in section 2.2.1 using Fourier transform in the frequency domain (with respect to the time variable) and wavenumber domain (with respect to the space variable). We will use the subscript  $\zeta$  to denote the former and the subscript  $\eta$  to denote the latter. By applying a Fourier transform to (2.10) in both variables we obtain

$$i\zeta e_{\zeta\eta}^d + i\eta v_\omega \cos(\theta) e_{\zeta\eta}^d = -\frac{1}{\tau_\omega} e_{\zeta\eta}^d + \frac{1}{\tau_\omega} (de^{\text{eq}}/dT)_{T_{\text{eq}}} \Delta \tilde{T}_{\zeta\eta} + 2\pi (de^{\text{eq}}/dT)_{T_{\text{eq}}} \delta(\eta - 2\pi L^{-1}), \quad (\text{B.1})$$

which provides the following relationship for  $e_{\zeta\eta}^d$

$$e_{\zeta\eta}^d = \frac{(de^{\text{eq}}/dT)_{T_{\text{eq}}} [\tau_\omega^{-1} \Delta \tilde{T}_{\zeta\eta} + 2\pi \delta(\eta - 2\pi L^{-1})]}{i\zeta + i\eta v_\omega \cos(\theta) + \tau_\omega^{-1}}. \quad (\text{B.2})$$

Applying Fourier transform in both variables to equation (2.3) and replacing  $e_{\zeta\eta}^d$  with the above result, we obtain the following expression for  $\Delta \tilde{T}_{\zeta\eta}$

$$\int_{\Omega} \int_{\omega} \left[ \frac{C_\omega}{\tau_\omega} \Delta \tilde{T}_{\zeta\eta} - \frac{(de^{\text{eq}}/dT)_{T_{\text{eq}}} [\tau_\omega^{-1} \Delta \tilde{T}_{\zeta\eta} + 2\pi \delta(\eta - 2\pi L^{-1})]}{i\tau_\omega \zeta + i\eta v_\omega \tau_\omega \cos(\theta) + 1} D_\omega \right] d\omega d\Omega = 0, \quad (\text{B.3})$$

which after integrating over  $\theta \in (0, \pi)$  and  $\phi \in (0, 2\pi)$  and algebraic simplification leads to the following relationship

$$\Delta\tilde{T}_{\zeta\eta} = \frac{\frac{\pi\delta(\eta-2\pi L^{-1})}{\eta} \int_{\omega} \frac{iC_{\omega}}{v_{\omega}\tau_{\omega}} \ln\left(\frac{\tau_{\omega}\zeta - v_{\omega}\tau_{\omega}\eta - i}{\tau_{\omega}\zeta + v_{\omega}\tau_{\omega}\eta - i}\right) d\omega}{\int_{\omega} \frac{C_{\omega}}{\tau_{\omega}} d\omega - \frac{1}{2\eta} \int_{\omega} \frac{iC_{\omega}}{v_{\omega}\tau_{\omega}^2} \ln\left(\frac{\tau_{\omega}\zeta - v_{\omega}\tau_{\omega}\eta - i}{\tau_{\omega}\zeta + v_{\omega}\tau_{\omega}\eta - i}\right) d\omega}. \quad (\text{B.4})$$

Equation (B.4) can be further simplified by applying the inverse Fourier transform in wavenumber domain  $\eta$ . Noting that equation (B.4) is in the form of  $\Delta\tilde{T}_{\zeta\eta} = \delta(\eta - 2\pi L^{-1})G(\eta, \zeta)$ , we use the identity

$$\frac{1}{2\pi} \int_{-\infty}^{\infty} \delta(\eta - 2\pi L^{-1}) G(\eta, \zeta) e^{i\eta x} d\eta = \frac{1}{2\pi} G(2\pi L^{-1}, \zeta) e^{2\pi i x/L}, \quad (\text{B.5})$$

to obtain

$$\Delta\tilde{T}_{\zeta} = \frac{e^{2\pi i x/L} \int_{\omega} S_{\omega} \tau_{\omega} d\omega}{\int_{\omega} [C_{\omega} \tau_{\omega}^{-1} - S_{\omega}] d\omega}, \quad (\text{B.6})$$

where  $S_{\omega}$  is given in (2.12). Equation (B.6) is similar to the result obtained in [37].

To obtain an expression for the temperature, we insert (B.4) into (B.2) and apply the inverse Fourier transform in wavenumber domain using the identity (B.5) to obtain

$$e_{\zeta}^d = \frac{e^{2\pi i x/L} (de^{\text{eq}}/dT)_{T_{\text{eq}}}}{i\tau_{\omega}\zeta + iv_{\omega}\tau_{\omega} \cos(\theta)2\pi L^{-1} + 1} \left[ \frac{\int_{\omega} S_{\omega} \tau_{\omega} d\omega}{\int_{\omega} C_{\omega} \tau_{\omega}^{-1} d\omega - \int_{\omega} S_{\omega} d\omega} + 1 \right]. \quad (\text{B.7})$$

This relation is then substituted in

$$\int_{\Omega} \int_{\omega} [C_{\omega} \Delta T_{\zeta} - e_{\zeta}^d D_{\omega}] d\omega d\Omega = 0, \quad (\text{B.8})$$

obtained by applying Fourier transform in the frequency domain to (2.4). Solving the resulting equation for  $\Delta T_{\zeta}$  leads to the expression provided in (2.11).

# Appendix C

## Solution of the transient thermal grating for late times

Introducing the definition  $\text{Kn}_\omega = v_\omega \tau_\omega 2\pi L^{-1}$  in equation (2.12), provides the following relationship for  $S_\omega$

$$S_\omega = \frac{iC_\omega}{2\text{Kn}_\omega \tau_\omega} \ln \left( \frac{\tau_\omega \zeta - \text{Kn}_\omega - i}{\tau_\omega \zeta + \text{Kn}_\omega - i} \right). \quad (\text{C.1})$$

Using a Taylor expansion for  $\tau_\omega \zeta \ll 1$  of the logarithmic term in (C.1) we obtain

$$S_\omega = \frac{iC_\omega}{2\text{Kn}_\omega \tau_\omega} \left[ -2i \tan^{-1}(\text{Kn}_\omega) - \frac{2\text{Kn}_\omega \tau_\omega}{\text{Kn}_\omega^2 + 1} \zeta + O(\tau_\omega^2 \zeta^2) \right], \quad (\text{C.2})$$

which is the same expression provided in equation (2.13). If we substitute  $S_\omega$  in (2.11) with (C.2) and neglect terms of  $O(\tau_\omega^2 \zeta^2)$  we obtain

$$\Delta T_\zeta = \frac{e^{2\pi i x/L}}{C} \left\{ \int_\omega C_\omega \tau_\omega \left[ \frac{\tan^{-1}(\text{Kn}_\omega)}{\text{Kn}_\omega} - \frac{\tau_\omega i \zeta}{\text{Kn}_\omega^2 + 1} \right] d\omega + \frac{\left[ \int_\omega C_\omega \left( \frac{\tan^{-1}(\text{Kn}_\omega)}{\text{Kn}_\omega} - \frac{\tau_\omega i \zeta}{\text{Kn}_\omega^2 + 1} \right) d\omega \right]^2}{\int_\omega \frac{C_\omega}{\tau_\omega} \left[ 1 - \frac{\tan^{-1}(\text{Kn}_\omega)}{\text{Kn}_\omega} + \frac{\tau_\omega i \zeta}{\text{Kn}_\omega^2 + 1} \right] d\omega} \right\}. \quad (\text{C.3})$$

Equation (C.3) is in the general form of

$$\Delta T_\zeta = k_1 - k_2 i \zeta + \frac{(k_3 - k_4 i \zeta)^2}{k_5 + k_6 i \zeta}, \quad (\text{C.4})$$

where  $k_1, k_2, \dots, k_6$  are independent of Fourier transform variable  $\zeta$  and depend only on the geometry and the material properties. Equation (C.4) can be further simplified in the following form

$$\Delta T_\zeta = k_1 - \frac{k_4^2 k_5}{k_6^2} - \frac{2k_3 k_4}{k_6} + \left( \frac{k_4^2}{k_6} - k_2 \right) i\zeta + \frac{(k_4 k_5 + k_3 k_6)^2}{k_6^2 (k_5 + k_6 i\zeta)}. \quad (\text{C.5})$$

Applying inverse Fourier transform to (C.5) leads to the following result

$$\Delta T = \left( k_1 - \frac{k_4^2 k_5}{k_6^2} - \frac{2k_3 k_4}{k_6} \right) \delta(t) + \left( \frac{k_4^2}{k_6} - k_2 \right) \delta'(t) + \frac{(k_4 k_5 + k_3 k_6)^2}{k_6^3} u(t) e^{-\frac{k_5}{k_6} t}, \quad (\text{C.6})$$

where  $\delta(t)$  and  $\delta'(t)$  are the delta Dirac function and its first derivative, respectively, and  $u(t)$  is the Heaviside function. At late times (more precisely,  $t > 0$ ), only the last term of (C.6) is nonzero. Substituting constants  $k_1$  through  $k_6$  in (C.6) with their equivalents from equation (C.3) leads to the result provided in (2.14).

# Appendix D

## Analytical solution for transient thermal grating in ballistic limit

The temperature relaxation profile in the ballistic limit can be obtained by setting  $\tau_\omega \rightarrow \infty$  in equation (2.11) and (2.12). Using this substitution, for  $S_\omega$  we have

$$S_\omega = \frac{iC_\omega L}{4\pi v_\omega \tau_\omega^2} \ln \left( \frac{\zeta - v_\omega 2\pi L^{-1}}{\zeta + v_\omega 2\pi L^{-1}} \right). \quad (\text{D.1})$$

Substituting this expression in (2.11), we observe that the second term of (2.11) vanishes in this limit (the numerator is  $O(\tau_\omega^{-2})$ , while the denominator is  $O(\tau_\omega^{-1})$ ). Therefore, we have

$$\Delta T_\zeta = \frac{iLe^{2\pi ix/L}}{4\pi C} \int_\omega \frac{C_\omega}{v_\omega} \ln \left( \frac{\zeta - v_\omega 2\pi L^{-1}}{\zeta + v_\omega 2\pi L^{-1}} \right) d\omega. \quad (\text{D.2})$$

The inverse Fourier transform of (D.2) can be calculated analytically [73] and gives

$$\Delta T = \frac{Le^{2\pi ix/L}}{2\pi Ct} \int_\omega \frac{C_\omega}{v_\omega} \sin(v_\omega 2\pi L^{-1}t) d\omega. \quad (\text{D.3})$$



# Appendix E

## Parameters of piece-wise linear model for transmissivity

The role of  $\bar{X}_j^S$  is similar to  $X_j^S$  in equation (A.1), therefore,

$$\begin{aligned}\bar{X}_0^S &= \bar{\omega}_0^S, \\ \bar{X}_{2j}^S &= \bar{\omega}_j^S + \Delta, \quad \bar{X}_{2j-1}^S = \bar{\omega}_j^S - \Delta, \quad j \in \{1, \dots, \bar{M}^S - 1\}, \\ \bar{X}_{2\bar{M}^S-1}^S &= \bar{\omega}_{\bar{M}^S}^S.\end{aligned}\tag{E.1}$$

The coefficients  $\bar{a}_j^S$ ,  $\bar{b}_j^S$ ,  $\bar{c}_j^S$ , and  $\bar{d}_j^S$  are calculated from the following equations

$$\begin{aligned}\bar{a}_j^S &= 0, \\ \bar{b}_j^S &= \frac{T_{12, \bar{\omega}_{j+1}}^S - T_{12, \bar{\omega}_j}^S}{\bar{\omega}_{j+1} - \bar{\omega}_j} - \frac{T_{12, \bar{\omega}_j}^S - T_{12, \bar{\omega}_{j-1}}^S}{\bar{\omega}_j - \bar{\omega}_{j-1}} - 3\bar{a}_j^S \bar{\omega}_j, \\ \bar{c}_j^S &= \frac{T_{12, \bar{\omega}_j}^S - T_{12, \bar{\omega}_{j-1}}^S}{\bar{\omega}_j - \bar{\omega}_{j-1}} - 3\bar{a}_j^S (\bar{\omega}_j - \Delta)^2 - 2\bar{b}_j^S (\bar{\omega}_j - \Delta), \\ \bar{d}_j^S &= \frac{T_{12, \bar{\omega}_{j+1}}^S - T_{12, \bar{\omega}_j}^S}{\bar{\omega}_{j+1} - \bar{\omega}_j} \Delta + T_{12, \bar{\omega}_j}^S - \bar{a}_j^S (\bar{\omega}_j + \Delta)^3 - \bar{b}_j^S (\bar{\omega}_j + \Delta)^2 - \bar{c}_j^S (\bar{\omega}_j + \Delta),\end{aligned}\tag{E.2}$$

where  $j \in \{1, \dots, \bar{M}^S - 1\}$  and  $S \in \{LA, TA_1, TA_2\}$ . Note that although the matching conditions between the line segments require a third order polynomial, here, due to the symmetrical choice of  $\Delta$ , the order of polynomial has reduced to two,  $\bar{a}_j^S = 0$ .



# Bibliography

- [1] E. POP, S. SINHA, AND K. E. GOODSON, *Heat generation and transport in nanometer-scale transistors*, proceedings of the IEEE 94, 1587-1601 (2006).
- [2] D. G. CAHILL, K. GOODSON, AND A. MAJUMDAR, *Thermometry and thermal transport in micro/nanoscale solid-state devices and structures*, Journal of Heat Transfer 124, 223-241 (2001).
- [3] Z. TIAN, S. LEE, G. CHEN, *Heat transfer in thermoelectric materials and devices*, Journal of Heat Transfer 135, 061605 (2013).
- [4] D. G. CAHILL, P. V. BRAUN, G. CHEN, D. R. CLARKE, S. FAN, K. E. GOODSON, P. KEBLINSKI, W. P. KING, G. D. MAHAN, A. MAJUMDAR, H. J. MARIS, S. R. PHILLPOT, E. POP, AND L. SHI, *Nanoscale thermal transport. II. 2003-2012*, Applied Physics Reviews 1, 011305 (2014).
- [5] K. ESFARJANI, G. CHEN, AND H. T. STOKES, *Heat transport in silicon from first-principles calculations*, Physical Review B 84, 085204 (2011).
- [6] A. WARD AND D. A. BROIDO, *Intrinsic phonon relaxation times from first-principles studies of the thermal conductivities of Si and Ge*, Physical Review B 81, 085205 (2010).
- [7] M. ZEBARJADI, K. ESFARJANI, M. S. DRESSELHAUS, Z. F. REN, AND G. CHEN, *Perspectives on thermoelectrics: from fundamentals to device applications*, Energy and Environmental Science 5, 5147-5162 (2012).
- [8] M. FORGHANI, N. G. HADJICONSTANTINOY, AND J.-P. M. PÉRAUD, *Reconstruction of the phonon relaxation times using solutions of the Boltzmann transport equation*, Physical Review B 94, 155439 (2016).
- [9] M. FORGHANI AND N. G. HADJICONSTANTINOY, *Reconstruction of phonon relaxation times from systems featuring interfaces with unknown properties*, Physical Review B 97, 195440 (2018).
- [10] J. A. JOHNSON, A. A. MAZNEV, J. CUFFE, J. K. ELIASON, A. J. MINNICH, T. KEHOE, C. M. SOTOMAYOR TORRES, G. CHEN, AND K. A. NELSON, *Direct measurement of room-temperature nondiffusive thermal transport over micron distances in a silicon membrane*, Physical Review Letters 110, 025901 (2013).

- [11] M. FORGHANI AND N. G. HADJICONSTANTINO, *Phonon relaxation time reconstruction from transient thermal grating experiments and comparison with density functional theory predictions*, Applied Physics Letters 114, 026103 (2019).
- [12] A. J. MINNICH, J. A. JOHNSON, A. J. SCHMIDT, K. ESFARJANI, M. S. DRESSELHAUS, K. A. NELSON, AND G. CHEN, *Thermal conductivity spectroscopy technique to measure phonon mean free paths*, Physical Review Letters 107, 095901 (2011).
- [13] A. J. MINNICH, *Determining phonon mean free paths from observations of quasiballistic thermal transport*, Physical Review Letters 109, 205901 (2012).
- [14] E. POP, *Energy dissipation and transport in nanoscale devices*, Nano Research 3, 147-169 (2010).
- [15] D. P. SELLAN, J. E. TURNEY, A. J. H. MCGAUGHEY, AND C. H. AMON, *Cross-plane phonon transport in thin films*, Journal of Applied Physics 108, 113524 (2010).
- [16] F. YANG AND C. DAMES, *Heating-frequency-dependent thermal conductivity: An analytical solution from diffusive to ballistic regime and its relevance to phonon scattering measurements*, Physical Review B 91, 165311 (2015).
- [17] K. T. REGNER, A. J. H. MCGAUGHEY, AND J. A. MALEN, *Analytical interpretation of nondiffusive phonon transport in thermoreflectance thermal conductivity measurements*, Physical Review B 90, 064302 (2014).
- [18] A. A. MAZNEV, J. A. JOHNSON, AND K. A. NELSON, *Onset of nondiffusive phonon transport in transient thermal grating decay*, Physical Review B 84, 195206 (2011).
- [19] Y. HU, L. ZENG, A. J. MINNICH, M. S. DRESSELHAUS, AND G. CHEN, *Spectral mapping of thermal conductivity through nanoscale ballistic transport*, Nature Nanotechnology 10, 701-706 (2015).
- [20] J.-K. YU, S. MITROVIC, D. THAM, J. VARGHESE, AND J. R. HEATH, *Reduction of thermal conductivity in phononic nanomesh structures*, Nature Nanotechnology 5, 718-721 (2010).
- [21] M. C. WINGERT, Z. C. Y. CHEN, E. DECHAUMPHAI, J. MOON, J.-H. KIM, J. XIANG, AND R. CHEN, *Thermal conductivity of Ge and GeSi coreshell nanowires in the phonon confinement regime*, Nano Letters 11, 5507-5513 (2011).
- [22] S.-M. LEE AND D. G. CAHILL, *Heat transport in thin dielectric films*, Journal of Applied Physics 81, 2590 (1997).
- [23] K. BISWAS, J. HE, I. D. BLUM, C.-I WU, T. P. HOGAN, D. N. SEIDMAN, V. P. DRAVID, AND M. G. KANATZIDIS, *High-performance bulk thermoelectrics with all-scale hierarchical architectures*, Nature 489, 414-418 (2012).

- [24] A. I. HOCHBAUM, R. CHEN, R. D. DELGADO, W. LIANG, E. C. GARNETT, M. NAJARIAN, A. MAJUMDAR, AND P. YANG, *Enhanced thermoelectric performance of rough silicon nanowires*, Nature 451, 163-167 (2008).
- [25] A. I. BOUKAI, Y. BUNIMOVICH, J. TAHIR-KHELI, J.-K. YU, W. A. GODDARD III, AND J. R. HEATH, *Silicon nanowires as efficient thermoelectric materials*, Nature 451, 168-171 (2008).
- [26] D. KRAEMER, B. POUDEL, H.-P. FENG, J. C. CAYLOR, B. YU, X. YAN, Y. MA, X. WANG, D. WANG, A. MUTO, K. MCENANEY, M. CHIESA, Z. REN, AND G. CHEN, *High-performance flat-panel solar thermoelectric generators with high thermal concentration*, Nature Materials 10, 532-538 (2011).
- [27] J. A. ROGERS, Y. YANG, AND K. A. NELSON, *Elastic modulus and in-plane thermal diffusivity measurements in thin polyimide films using symmetry-selective real-time impulsive stimulated thermal scattering*, Applied Physics A 58, 523-534 (1994).
- [28] K. C. COLLINS, A. A. MAZNEV, Z. TIAN, K. ESFARJANI, K. A. NELSON, AND G. CHEN, *Non-diffusive relaxation of a transient thermal grating analyzed with the Boltzmann transport equation*, Journal of Applied Physics 114, 104302 (2013).
- [29] J.-P. M. PÉRAUD AND N. G. HADJICONSTANTINO, *Efficient simulation of multidimensional phonon transport using energy-based variance-reduced Monte Carlo formulations*, Physical Review B 84, 205331 (2011).
- [30] J.-P. M. PÉRAUD AND N. G. HADJICONSTANTINO, *An alternative approach to efficient simulation of micro/nanoscale phonon transport*, Applied Physics Letters 101, 153114 (2012).
- [31] J.-P. M. PÉRAUD, C. D. LANDON, AND N. G. HADJICONSTANTINO, *Monte Carlo methods for solving the Boltzmann transport equation*, Annual Review of Heat Transfer 17, 205-265 (2014).
- [32] J.-P. M. PÉRAUD AND N. G. HADJICONSTANTINO, *Adjoint-based deviational Monte Carlo methods for phonon transport calculations*, Physical Review B 91, 235321 (2015).
- [33] D. G. CAHILL, W. K. FORD, K. E. GOODSON, G. D. MAHAN, A. MAJUMDAR, H. J. MARIS, R. MERLIN, AND S. R. PHILLPOT, *Nanoscale thermal transport*, Journal of Applied Physics 93, 793 (2003).
- [34] M. E. SIEMENS, Q. LI, R. YANG, K. A. NELSON, E. H. ANDERSON, M. M. MURNANE, AND H. C. KAPTEYN, *Quasi-ballistic thermal transport from nanoscale interfaces observed using ultrafast coherent soft X-ray beams*, Nature Materials 9, 26-30 (2010).

- [35] K. M. HOOGEBOOM-POT, J. N. HERNANDEZ-CHARPAK, X. GU, T. D. FRAZER, E. H. ANDERSON, W. CHAO, R. W. FALCONE, R. YANG, M. M. MURNANE, H. C. KAPTEYN, AND D. NARDI, *A new regime of nanoscale thermal transport: Collective diffusion increases dissipation efficiency*, Proceedings of the National Academy of Sciences USA 112, 4846-4851 (2015).
- [36] E. T. SWARTZ AND R. O. POHL, *Thermal boundary resistance*, Reviews of Modern Physics 61, 605 (1989).
- [37] C. HUA AND A. J. MINNICH, *Transport regimes in quasiballistic heat conduction*, Physical Review B 89, 094302 (2014).
- [38] A. J. MINNICH, *Multidimensional quasiballistic thermal transport in transient grating spectroscopy*, Physical Review B 92, 085203 (2015).
- [39] A. J. MINNICH, *Exploring electron and phonon transport at the nanoscale for thermoelectric energy conversion*, PhD thesis, Massachusetts Institute of Technology, Cambridge, MA (2011).
- [40] S. BERNARD, E. WHITEWAY, V. YU, D. G. AUSTING, AND M. HILKE, *Probing the experimental phonon dispersion of graphene using  $^{12}\text{C}$  and  $^{13}\text{C}$  isotopes*, Physical Review B 86, 085409 (2012).
- [41] F. WIDULLE, T. RUF, O. BURESCH, A. DEBERNARDI, AND M. CARDONA, *Raman study of isotope effects and phonon eigenvectors in SiC*, Physical Review Letters 82, 3089 (1999).
- [42] J. SERRANO, J. STREMPFER, M. CARDONA, M. SCHWOERER-BÖHNING, H. REQUARDT, M. LORENZEN, B. STOJETZ, P. PAVONE, AND W. J. CHOYKE, *Determination of the phonon dispersion of zinc blende (3C) silicon carbide by inelastic x-ray scattering*, Applied Physics Letters 80, 4360 (2002).
- [43] J. MAULTZSCH, S. REICH, C. THOMSEN, E. DOBARDŽIĆ, I. MILOŠEVIĆ, AND M. DAMNJANOVIĆ, *Phonon dispersion of carbon nanotubes*, Solid State Communications 121, 471-474 (2002).
- [44] A. EICHLER, K.-P. BOHNEN, W. REICHARDT, AND J. HAFNER, *Phonon dispersion relation in rhodium: Ab initio calculations and neutron-scattering investigations*, Physical Review B 57, 324 (1998).
- [45] T. LUO, J. GARG, J. SHIOMI, K. ESFARJANI, AND G. CHEN, *Gallium arsenide thermal conductivity and optical phonon relaxation times from first-principles calculations*, Europhysics Letters 101, 16001 (2013).
- [46] L. WIRTZ AND A. RUBIO, *The phonon dispersion of graphite revisited*, Solid State Communications 131, 3, 141-152 (2004).

- [47] P. SCHAROCH, K. PARLIŃSKI, AND A. KIEJNA, *Ab initio calculations of phonon dispersion relations in aluminum*, Acta Physica Polonica A 97, 2, 349-354 (2000).
- [48] A. ALENITSYN, *On smoothing of non-smooth functions*, Math Track 2, 17-21 (2006).
- [49] M. G. HOLLAND, *Analysis of Lattice Thermal Conductivity*, Physical Review 132, 6, 2461 (1963).
- [50] A. S. HENRY AND G. CHEN, *Spectral phonon transport properties of silicon based on molecular dynamics simulations and lattice dynamics*, Journal of Computational and Theoretical Nanoscience 5, 141-152 (2008).
- [51] J. A. NELDER AND R. MEAD, *A simplex method for function minimization*, The Computer Journal 7, 308-313, (1965).
- [52] K. KLEIN AND J. NEIRA, *Nelder-Mead simplex optimization routine for large-scale problems: A distributed memory implementation*, Computational Economics 43, 4, 447-461 (2014).
- [53] M. MITCHELL, *An introduction to genetic algorithms*, MIT press (1998).
- [54] S. KIRKPATRICK, C. D. GELATT, AND M. P. VECCHI, *Optimization by simulated annealing*, Science 220, 4598, 671-680 (1983).
- [55] J. C. LAGARIAS, J. A. REEDS, M. H. WRIGHT, AND P. E. WRIGHT, *Convergence properties of the Nelder-Mead simplex method in low dimensions*, SIAM Journal on Optimization 9, 1, 112-147 (1998).
- [56] W. H. PRESS, S. A. TEUKOLSKY, W. T. VETTERLING, AND B. P. FLANNERY, *Numerical recipes in C: The art of scientific computing*, Cambridge University Press, Cambridge (1992).
- [57] R. R. BARTON AND J. S. IVEY JR., *Modifications of Nelder-Mead simplex method for stochastic simulation response optimization*, Proceedings of the Winter Simulation Conference, 945-953 (1991).
- [58] E. O. BRIGHAM, *The fast Fourier transform*, Prentice-Hall, New Jersey (1988).
- [59] E. HAZAN, K. Y. LEVY, AND S. SHALEV-SHWARTZ, *On Graduated Optimization for Stochastic Non-Convex Problems*, Proceedings of the 33rd International Conference on Machine Learning 48, 1833-1841 (2016).
- [60] N. G. HADJICONSTANTINOY, *Hybrid atomistic-continuum formulations and the moving contact-line problem*, Journal of Computational Physics 154, 245-265 (1999).

- [61] Due to a small discrepancy between the true data of [13] and the present work (likely related to discretization), the “Reconstructed CDF,  $\kappa_{eff}$ ” data was slightly scaled; at the same time, care was taken to ensure that the discrepancy with the present work true data shown in the figure is the same or smaller than that shown in figure 2 of [13].
- [62] J.-P. M. PÉRAUD, *Efficient multiscale methods for micro/nanoscale solid state heat transfer*, PhD thesis, Massachusetts Institute of Technology, Cambridge, MA (2015).
- [63] J.-P. M. PÉRAUD AND N. G. HADJICONSTANTINOY, *Extending the range of validity of Fourier’s law into the kinetic transport regime via asymptotic solution of the phonon Boltzmann transport equation*, Physical Review B 93, 045424 (2016).
- [64] R. STEDMAN AND G. NILSSON, *Dispersion relations for phonons in aluminum at 80 and 300 K*, Physical Review 145, 492 (1966).
- [65] A. J. MINNICH, G. CHEN, S. MANSOOR, AND B. S. YILBAS, *Quasiballistic heat transfer studied using the frequency-dependent Boltzmann transport equation*, Physical Review B 84, 235207 (2011).
- [66] W. A. LITTLE, *The transport of heat between dissimilar solids at low temperatures*, Canadian Journal of Physics 37, 334-349 (1959).
- [67] C. HUA, X. CHEN, N. K. RAVICHANDRAN, AND A. J. MINNICH, *Experimental metrology to obtain thermal phonon transmission coefficients at solid interfaces*, Physical Review B 95, 205423 (2017).
- [68] D. LI AND A. J. H. MCGAUGHEY, *Phonon dynamics at surfaces and interfaces and its implications in energy transport in nanostructured materials - An opinion paper.*, Nanoscale and Microscale Thermophysical Engineering 19, 166-182 (2015).
- [69] W. LI, J. CARRETE, N. A. KATCHO, AND N. MINGO, *ShengBTE: A solver of the Boltzmann transport equation for phonons*, Computer Physics Communications 185, 1747-1758 (2014).
- [70] M. A. LUERSEN AND R. L. RICHE, *Globalized Nelder-Mead method for engineering optimization*, Computers and Structures 82, 2251-2260 (2004).
- [71] G. O. ROBERTS, A. GELMAN, AND W. R. GILKS, *Weak convergence and optimal scaling of random walk Metropolis algorithms*, The Annals of Applied Probability 7, 110-120 (1997).
- [72] P. R. CONRAD, A. D. DAVIS, Y. M. MARZOUK, N. S. PILLAI, AND A. SMITH, *Parallel local approximation MCMC for expensive models*, SIAM/ASA Journal on Uncertainty Quantification 6, 339-373 (2018).
- [73] I. S. GRADSHTEYN AND I. M. RYZHIK, *Table of integrals, series, and products*, 7th edition, Academic press, Burlington, MA, (2007).